Cavitation in gas-saturated liquids

Citation for published version (APA):
Rooze, J. (2012). *Cavitation in gas-saturated liquids*. [Phd Thesis 1 (Research TU/e / Graduation TU/e), Chemical Engineering and Chemistry]. Technische Universiteit Eindhoven. https://doi.org/10.6100/IR732583

DOI:
10.6100/IR732583

Document status and date:
Published: 01/01/2012

Document Version:
Publisher's PDF, also known as Version of Record (includes final page, issue and volume numbers)

Please check the document version of this publication:

• A submitted manuscript is the version of the article upon submission and before peer-review. There can be important differences between the submitted version and the official published version of record. People interested in the research are advised to contact the author for the final version of the publication, or visit the DOI to the publisher's website.
• The final author version and the galley proof are versions of the publication after peer review.
• The final published version features the final layout of the paper including the volume, issue and page numbers.

Link to publication

General rights
Copyright and moral rights for the publications made accessible in the public portal are retained by the authors and/or other copyright owners and it is a condition of accessing publications that users recognise and abide by the legal requirements associated with these rights.

- Users may download and print one copy of any publication from the public portal for the purpose of private study or research.
- You may not further distribute the material or use it for any profit-making activity or commercial gain
- You may freely distribute the URL identifying the publication in the public portal.

If the publication is distributed under the terms of Article 25fa of the Dutch Copyright Act, indicated by the "Taverne" license above, please follow below link for the End User Agreement:

www.tue.nl/taverne

Take down policy
If you believe that this document breaches copyright please contact us at:

openaccess@tue.nl

providing details and we will investigate your claim.

Download date: 04. Oct. 2023

Cavitation in gas-saturated liquids

Joost Rooze

A catalogue record is available from the Eindhoven University of Technology Library
ISBN: 978-90-386-3151-6

Printed by Ipskamp Drukkers, Enschede
Cover design inspired by “Incredible visual illusions” (**2004**) Arcturus Publishing Limited

Cavitation in gas-saturated liquids

PROEFSCHRIFT

ter verkrijging van de graad van doctor aan de
Technische Universiteit Eindhoven, op gezag van de
rector magnificus, prof.dr.ir. C.J. van Duijn, voor een
commissie aangewezen door het College voor
Promoties in het openbaar te verdedigen
op maandag 11 juni 2012 om 16.00

door

Joost Rooze

geboren te Eindhoven

Dit proefschrift is goedgekeurd door de promotoren:

prof.dr.ir. J.T.F. Keurentjes
en
prof.dr.ir. J.C. Schouten

Copromotor:
prof.dr. E.V. Rebrov

Summary

Cavitation in gas-saturated liquids

Oscillating gas bubbles can be created in a liquid by exposing it to ultrasound. These gas bubbles can implode if the sound pressure is high enough. This process is called cavitation. Interesting phenomena take place during the collapse. The gas and vapour inside the bubble are compressed and reach temperatures of several thousand Kelvin and pressures of several hundred bars, a dense plasma is formed inside the bubble, light is emitted, reactive radical molecules are formed, and there is a liquid flow around the bubble which can be utilised for mixing or even scission of polymers by strain rates. A jet is formed if the bubble collapses near a wall. The pressure and temperature are at ambient conditions in the liquid during this process. There is a plethora of applications which can be operated or intensified by cavitation, *e.g.* micro mixing, catalyst surface renewal and material synthesis, treatment of kidney stones, waste water treatment and other radical-induced chemistry such as polymerisation, and polymer weight distribution control.

In this thesis, several forms of cavitation have been investigated. Special attention is paid to the influence of gas and vapour content in the cavitation bubble. The gas and vapour content of the bubble play a crucial role in the extent of the effects of cavitation. First and foremost the thermal properties adiabatic index and heat conductivity determine the maximum temperature during the collapse. Gases with a high adiabatic index, such as noble gases, and liquids with a low vapour pressure and a high adiabatic index, such as water or sulfuric acid, yield the highest hot spot temperatures and therefore the most intense effects. Some gases such as oxygen also participate in chemical reactions. Another difference between cavitation effects of several gases may be caused by changing gas solubility in the liquid. This changes the concentration gradient around the bubble, and the mass transport to and from the bubble.

The effects of the gas on the cavitation process depend on the ultrasound frequency. At frequencies above 20 kHz air has a higher efficiency of radical formation than argon as a sat-

uration gas. This has been measured by following the oxidation of potassium iodide to iodine spectroscopically. The carbon dioxide in the air contributes to this increase at low ultrasound input power. This is surprising since carbon dioxide addition in the cavitation bubble gas phase likely suppresses the hot spot temperature. The enhancement of radical production by carbon dioxide only occurs when it is present in low quantities (< 1.5 vol%). A combination of the saturation gases argon (79 vol%), oxygen (20 vol%), and carbon dioxide (1 vol%) gives the highest radical production. Argon has a low heat capacity which results in high hot spot temperatures. Oxygen participates in new chemical reactions, which gives a higher probability of conversion of initial radicals towards the end product. The mechanism through which carbon dioxide enhances the radical production is speculative. It may be possible that the shape of the cavitation bubbles and micro bubble ejection is altered by enhanced mass transport of carbon dioxide into the bubble. Also the chemical pathways are changed.

Sometimes a high reactivity by radicals is undesired in an ultrasound process. An example of such a process is the study of scission of polymer-metal complexes by strain induced by a collapsing bubble. By mechanical scission of the complex the metal inside it becomes exposed and becomes available for catalytic reactions. This opens up interesting applications such as self-regenerating materials or materials that change colour when they are exposed to strain. Thermal activation and activation by radicals must be low compared to mechanical scission to be able to study the mechanical activation precisely. This has been done by changing the saturation gas from argon to methane or nitrogen. The radical production is 2 times higher under argon than under a nitrogen atmosphere, and 20 times higher under argon than under a methane atmosphere. The hot spot temperature correlates with the radical production. The scission percentages are roughly the same under these gases, indicating that mechanical scission is the most important mechanism of complex breakage. This is supported by model calculations of a collapsing bubble in a liquid saturated with these gases.

An alternative method to create cavitation and its effects is by creating a flow through a constriction. The pressure inside the constriction drops to values sufficient to induce bubble growth, and subsequently the bubble collapses. Miniaturisation of this process is desired because it allows easy study in precisely manufactured geometries, and because the apparent frequency of the process increases. Experimental observations have been compared to computational fluid dynamics modeling results, which show that it is important that the constriction exits in an unconfined area. An extended low pressure region can occur that induces excessive bubble growth and a non-violent implosion of the bubbles if the constriction exit is confined. Values of about 160 kHz in 0.75 mm capillaries are reached in 0.2 mm constrictions operated with a flow of 90 mL min^{-1}, which equals a liquid velocity in the constriction of 59 m s^{-1}. A radical production in the same range as those reported in previous work on hydrodynamic cavitation is measured with these settings. Chlorohydrocarbons have been added to the liquid to increase radical production. Simulations of the temperature of a collapsing bubble show a qualitative correlation with the radical production.

A physical representation of the propagation of sound waves in a liquid-gas slug flow has been developed to gain understanding of pressure pulse propagation in two-phase systems and to be able to safely operate a gas-liquid micro separator. An undesired pressure increase by *e.g.* temporary blocking of an upstream microchannel can result in leaking of the liquid to the gas side. A safety pressure release valve and a safety capillary are incorporated into the process. The safety valve releases any undesired over pressure to the atmosphere. The safety capillary and the pressure pulse propagation speed are needed to be able to have enough time to open the valve. A second advantage of the developed equation is that, together with an equation for pressure drop, the gas bubble length and gas fraction inside the capillary can be calculated. This offers opportunities for online characterisation of slug flow in micro reactors.

Table of contents

Introduction

1

1.1 The oscillating bubble

Gas bubbles in liquids can be made to expand and contract. An easy method to do this is to make a droplet of water fall inside a vessel of water. An air pocket is formed which contracts, acting as a resonator[1] and emitting a sound wave. This is the familiar dripping sound of water. Bubbles can be made to contract in other circumstances as well, for example with the oscillating pressure of a sound wave, or even a shock wave. This sound wave consists of rarefaction and compression cycles. These cycles create a force on the bubble wall, and the bubble grows or shrinks. The bubble can grow from a nucleus of several hundred nanometers to a size of several hundred micrometers, a length scale visible to the eye, if the amplitude of the sound wave is sufficient.

The bubble diameter has a sinusoidal variation when a gentle oscillation is applied, and a non-sinusoidal curve at higher oscillation amplitudes (see Fig. 1.1). The bubble violently collapses after it has grown to an instable size during the sound rarefaction wave. The formation and collapse of these bubbles is called cavitation. The bubble wall can reach the speed of sound during the collapse, and thus a shock wave inside the bubble is formed. Methods to create cavitation are by applying ultrasound to a liquid, by flowing a liquid with initial gas pockets through a constriction, so-called hydrodynamic cavitation, by impact of a droplet with a solid surface, or by local boiling of the liquid by using a focussed laser burst.

1.2 Secondary effects of cavitation

Besides bubble oscillations a number of interesting secondary phenomena take place during or around the bubble collapse. The bubble is compressed during the collapse, and this gives

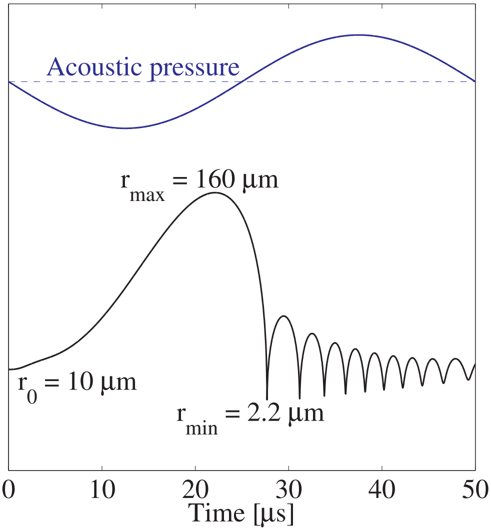

Figure 1.1: Mathematical description of a collapsing gas bubble with an initial radius r_0 of 10 µm under influence of a sinusoidal acoustic pressure field. The bubble reaches its maximum radius after a growth phase during the rarefaction wave. The collapse takes place in a relatively short time span and compresses the bubble to its minimum size. The pressure is very high in the bubble at this point, and the bubble rebounces to a larger size. New collapses take place after the rebounce, but these are less violent than the first collapse.

pressures of several hundred bars, and temperatures of several thousands degrees Kelvin. Molecular bonds can be dissociated, creating two reactive radical atoms or molecules. Atoms and molecules are split up in ions and electrons inside the bubble under these extreme conditions, and the interactions between these charged particles can create a flash of light[2]. The quick collapse and recovery makes the heating and cooling rates of the bubble very high[3].

The liquid around the bubble is also subject to forces during the oscillation of the bubble. An oscillating bubble acts as a liquid pump near a wall[4], displacing the fluid in circulations. The flow near the wall creates shear forces. These shear forces are strong enough to remove particles adhered to a surface[5]. The liquid also follows the gas bubble collapse and is sucked in during the compression stage. This creates high strain rates in the fluid, which are strong enough to pull macromolecules apart[6].

Cavitation has been applied in nature by the snapping shrimp. This creature has a large claw that creates a jet of water when the claw is closed swiftly. The impact of the jet and the formed collapsing cavitation bubbles stuns prey[7]. Cavitation can be used in chemical engineering to mix liquids by the streaming effects, to start chemical reactions with radical molecules[8], in breakdown of waste molecules which are hard to remove by conventional methods[9,10], to clean surfaces from contaminations, or to renew surfaces[3]. The large num-

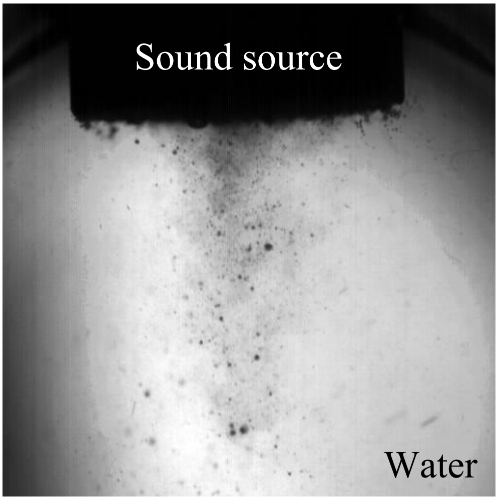

Figure 1.2: Cavitation field in argon saturated water with a 20 kHz sound source in the top of the image. A conical, oscillating bubble field forms under the sound source. The sound source is 1.27 cm in diameter and is backlighted with a Dedocool CoolT3 250 W lamp. The image is taken with a Redlake X4 high speed camera, equipped with a Nikon AF micro Nikkor 60 mm lens.

ber of possible applications have made the study of cavitation popular in recent decades.

1.3 Scientific challenges

There are several fundamental issues in cavitation research which call for further study, even though several decades of research has yielded many interesting results. This is probably because direct measurements of a cavitation bubble contents are impossible for several if not most of the interesting physical parameters. The bubble radius over time and the bubble field can be probed optically, as well as the luminescence of sonoluminescence. The chemical and mechanical effects of cavitation are also probed, although these effects usually result from a sequence of steps in the cavitation process. The hot spot temperature and pressure, and the distribution of molecules inside the cavitation bubble can only be estimated theoretically[11] or indirectly[12,13].

The formation of a field of bubbles is another active research field. Several structures are observed in multi bubble cavitation experiments. A conical structure is formed under a 20 kHz ultrasound horn (see Figure 1.2). Long filaments consisting of many bubbles that survive for many cycles are seen at higher frequencies[14]. There exists an optimum ultrasound frequency of about 300 kHz for radical production[15]. There are more collapses per second at this frequency, but they are believed to be less violent. The gas bubbles in a high frequency ultrasound field survive many collapses giving rise to secondary effects such as rectified diffusion. The interplay between these uncertain parameters makes the study of the effect of ultrasound frequency on the cavitation process complex, and interesting for further study.

Cavitation is also induced by creating a flow through a constriction. A low pressure region is formed in and after the constriction. Nuclei present in the liquid grow and subsequently collapse in a similar fashion as bubbles in an ultrasound field. It is slightly surprising that there is debate in the scientific literature over which method creates the most radicals per energy input although the governing physics are very similar.

This thesis focuses on several of the unresolved aspects of cavitation. The influence of the gas on both mechanical and chemical cavitation processes has been studied. The energy efficiency is taken into account when studying chemical processes. Hydrodynamic cavitation has been studied on several length scales ranging from tens to hundreds of micrometers.

1.4 Outline of this thesis

The gas contents of the cavitation bubble have a large effect on the overall process efficacy in any cavitation process. A review of the published work concerning the bubble gas content in cavitation research is presented in **Chapter 2**. The observations that have been made and have been described in literature are presented first. A detailed discussion of all the possible mechanisms for the observed effects that gas participates in is shown afterwards.

Gas, frequency, and power effects are discussed in **Chapter 3**. Experiments have been performed using simple materials such as a commercial ultrasound device, a home built amplifier, and aqueous solutions potassium iodide salt. Radical formation is more efficient at higher power than at lower power in the power range measured. The ultrasound frequency of 62 kHz gives a standing wave as opposed to the two lower frequencies measured (20 and 41 kHz), and the standing waves result in more efficient radical formation. Using air as a saturation gas gives a higher oxidation yield at 62 kHz than when using argon, even though argon has a higher adiabatic index and from a thermal point of view higher hot spot temperatures are expected when using argon as a saturation gas.

Further investigation of the phenomena encountered in a 62 kHz field is presented in **Chapter 4**. Solutions saturated with gas mixtures of argon and oxygen yield a higher oxidation yield when exposed to ultrasound. The oxygen inside the bubble can alter the oxidation yield by participating in chemical reactions. Acidification of the liquid by carbon dioxide addition (< 1.5 vol% in argon) or citric acid addition further enhances the radical production rate.

The relation between saturation gas and the mechanical effects is investigated in **Chapter 5**, where a novel catalyst is activated by the strain rates created by collapsing bubbles. The catalyst is a complex of a metal ion and two polymer tails, and can be broken into two pieces. The solubility of the gas alters the gas mass transport into the bubble during bubble growth and collapse. The thermal properties during collapse, and therefore also the hot spot temperature and radical production also change with saturation gas. The most likely mechanism of catalyst complex scission takes place due to mechanical forces. Experimental results on catalyst scission and radical production are compared to modelling of a collapsing bubble.

Hydrodynamic cavitation on several length scales is shown in **Chapter 6**. Theoretical considerations suggest that smaller length scales give a higher radical production per unit of energy. Radical production has been measured in a micro channel with a constriction with a typical diameter of 60 µm, and in a view cell with a constriction of 0.2 mm using potassium iodide oxidation as a demonstration reaction. The results have been compared to Computational Fluid Dynamics (CFD) modeling, which included a cavitation model. The pressure profiles obtained by the CFD analysis were used to calculate the collapse characteristics of a bubble travelling in the channel. Experimental validation of a chemical reaction has only been obtained in the 0.2 mm constriction at higher flow rates. This qualitatively agrees with the obtained CFD results.

The propagation of pressure waves in air-water slug flow in micro fluidic capillaries is discussed in **Chapter 7**. The propagation and reflection of waves in bubbly and slug flow are of interest when studying cavitation phenomena, especially if miniaturisation is desired, as described in Chapter 6, but then in case of acoustic phenomena. A model from literature, derived to describe pressure propagation in large scale slug flow, also describes micro fluidic flow. The capillary elasticity and the pressure drop over the capillary are taken into account. The model is used to calculate the length of safety capillaries that are used to protect downstream equipment from pressure surges, and it can be used to calculate gas bubble length and void fraction in a slug flow when pressure drop and the propagation speed are known. No fitting parameters are needed in this calculation.

Chapter 8 contains a discussion on the use of cavitation as a tool to improve chemical and physical processes in the future.

Bibliography

[1] M. Minnaert, On musical air-bubbles and the sounds of running water, Philosophical Magazine Series 7 16(104) (**1933**) 235–248. `doi:10.1080/14786443309462277`.

[2] D. J. Flannigan, K. S. Suslick, Plasma formation and temperature measurement during single-bubble cavitation, Nature 434(7029) (**2005**) 52–55. `doi:10.1038/nature03361`.

[3] K. S. Suslick, G. J. Price, Applications of ultrasound to materials chemistry, Annual Review of Materials Science 29(1) (**1999**) 295–326. `doi:10.1146/annurev.matsci.29.1.295`.

[4] P. Marmottant, M. Versluis, N. de Jong, S. Hilgenfeldt, D. Lohse, High-speed imaging of an

ultrasound-driven bubble in contact with a wall: “Narcissus” effect and resolved acoustic streaming, Experiments in Fluids 41 (**2006**) 147–153. `doi:10.1007/s00348-005-0080-y`.

[5] M. Hauptmann, S. Brems, E. Camerotto, A. Zijlstra, G. Doumen, T. Bearda, P. Mertens, W. Lauriks, Influence of gasification on the performance of a 1 MHz nozzle system in megasonic cleaning, Microelectronic Engineering 87(5-8) (**2010**) 1512–1515. `doi:10.1016/j.mee.2009.11.061`.

[6] A. M. Basedow, K. H. Ebert, Ultrasonic Degradation of Polymers in Solution, Springer-Verlag, Berlin, 1977.

[7] M. Versluis, B. Schmitz, A. von der Heydt, D. Lohse, How snapping shrimp snap: through cavitating bubbles, Science 289(5487) (**2000**) 2114–2117. `doi:10.1126/science.289.5487.2114`.

[8] M. M. van Iersel, M. A. van Schilt, N. E. Benes, J. T. F. Keurentjes, Controlled methyl chloride synthesis at mild conditions using ultrasound irradiation, Ultrasonics Sonochemistry 17(2) (**2010**) 315–317. `doi:10.1016/j.ultsonch.2009.08.002`.

[9] J. Lifka, B. Ondruschka, J. Hofmann, The use of ultrasound for the degradation of pollutants in water: Aquasonolysis - a review, Engineering in Life Sciences 3(6) (**2003**) 253–262. `doi:10.1002/elsc.200390040`.

[10] J. González-García, V. Sáez, I. Tudela, M. I. Díez-Garcia, M. Deseada Esclapez, O. Louisnard, Sonochemical treatment of water polluted by chlorinated organocompounds. A review, Water 2(1) (**2010**) 28–74. `doi:10.3390/w2010028`.

[11] M. P. Brenner, S. Hilgenfeldt, D. Lohse, Single-bubble sonoluminescence, Reviews of Modern Physics 74(2) (**2002**) 425–484. `doi:10.1103/RevModPhys.74.425`.

[12] K. S. Suslick, D. A. Hammerton, R. E. Cline, Sonochemical hot spot, Journal of the American Chemical Society 108(18) (**1986**) 5641–5642. `doi:10.1021/ja00278a055`.

[13] K. Okitsu, T. Suzuki, N. Takenaka, H. Bandow, R. Nishimura, Y. Maeda, Acoustic multibubble cavitation in water: A new aspect of the effect of a rare gas atmosphere on bubble temperature and its relevance to sonochemistry, Journal of Physical Chemistry B 110(41) (**2006**) 20081–20084. `doi:10.1021/jp064598u`.

[14] J. Appel, P. Koch, R. Mettin, D. Krefting, W. Lauterborn, Stereoscopic high-speed recording of bubble filaments, Ultrasonics Sonochemistry 11(1) (**2004**) 39–42. `doi:10.1016/S1350-4177(03)00111-1`.

[15] D. G. Wayment, D. J. Casadonte Jr., Design and calibration of a single-transducer variable-frequency sonication system, Ultrasonics Sonochemistry 9(4) (**2002**) 189–195. `doi:10.1016/S1350-4177(01)00127-4`.

2

Gas type and ultrasonic cavitation – a review

The physics and chemistry of non-linearly oscillating acoustic cavitation bubbles are strongly influenced by the dissolved gas in the surrounding liquid. Changing the gas alters among others the luminescence spectrum, and the radical production of the collapsing bubbles. An overview of experiments with various gas types and concentration described in literature is given and is compared to mechanisms that lead to the observed changes in luminescence spectra and radical production. The dissolved gas type changes the bubble adiabatic ratio, thermal conductivity, and the liquid surface tension, and consequently the hot spot temperature. The gas can also participate in chemical reactions, which can enhance radical production or luminescence of a cavitation bubble. With this knowledge, the gas content in cavitation can be tailored to obtain the desired output.

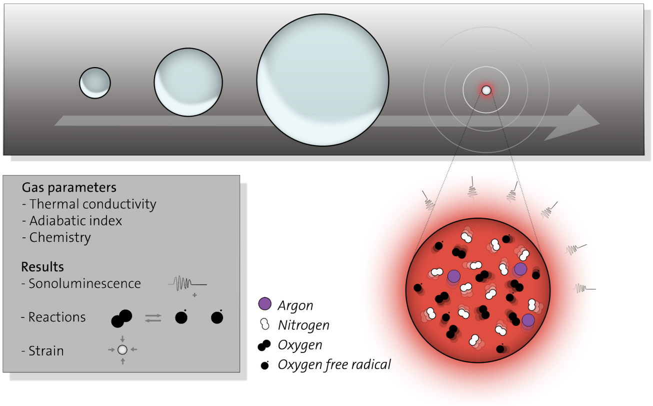

This Chapter is to be published as: J. Rooze, E. V. Rebrov, J. C. Schouten, and J. T. F. Keurentjes, Cavitation and gas type: a review. *Ultrasonics Sonochemistry*, Accepted

2.1 Introduction

Acoustic cavitation is the growth of a nucleus in a liquid, and subsequent collapse of the formed gas bubble[1,2]. The collapse takes place in microseconds and can be considered as adiabatic. High temperatures and pressures are reached inside the bubble due to gas compression. A large energy concentration is achieved during the collapse, resulting in a local temperature of several thousands of Kelvin[3,4]. This energy is dispersed to the surroundings during the collapse and after-bounces so that the gas temperature in the hot spot quickly returns to the ambient value. Typical phenomena that may be observed during cavitation are luminescence of the bubbles[5–8], high heating and cooling rates[9], radical production[10–12], high strain rates near the bubble wall[13], streaming of the liquid around the bubble[14], and liquid jet formation[15,16]. Dissolved gas is present as nuclei in the liquid. The nuclei are stabilised by dust particles, solid parts of the system, or by amphiphilic molecules or other contaminations[17].

The influence of dissolved gas type and concentration on ultrasonic cavitation processes is reviewed in this work. Previous reviews have focussed on sonoluminescence[5–8] or sonochemistry[11,12,18]. Both processes are put into further perspective within the framework of the influence of the dissolved gas. The combination of gas and vapour defines the thermal properties of the bubble during collapse, and dissolved gas can alter the radial dynamics of the collapse by mass transport to and from the bubble, and also by damping of the oscillation due to inhomogeneities in the pressure field[19]. The gas contents of the liquid and gas bubbles can be used to control acoustic cavitation by maximising or minimising luminescence, radical production, or other effects. This is of interest to scientists aiming for increased control over the cavitation process. The experiments reported in literature that show the effects of gas content in the liquid and cavitation bubble are described in Section 2.2. Single-bubble and multi-bubble sonoluminescence are discussed first, after which the literature experiments on the influence of gas content on the chemical reactions in and around the bubble are presented. The physical mechanisms that account for the observations described, bubble heat capacity, thermal conductivity, and chemical changes of the bubble contents are discussed in Section 2.3. A summary and a brief outlook are given in Section 2.4.

2.2 Dissolved gas in cavitation

2.2.1 Sonoluminescence

Sonoluminescence (SL) is the light emission that occurs during the collapse of a gas bubble that is non-linearly oscillating due to ultrasound[5,7,8]. Such a cavitation cycle is shown schematically in Fig. 2.1. The bubble grows to a maximum size during the period of rarefaction, and subsequently collapses. After-bounces occur after the first, most violent collapse. The bubble collapse creates a hot spot with temperatures of up to tens of thousands of Kelvin[4]), during which an opaque plasma consisting of ions and electrons with a high density of ≈ 1000 kg m^{-3} is formed[3,20,21]. Radiation is emitted from this plasma. Sources of this radiation are emissions by Bremsstrahlung and incandescent black body radiation[20,22], as well as ion recombination radiation[23,24], and spectral emissions from electronic transitions[3,21]. Multi-bubble sonoluminescence (MBSL) and single-bubble sonoluminescence (SBSL) (see Fig. 2.2 for examples) are generally treated separately as different manifestations of sonoluminescence.

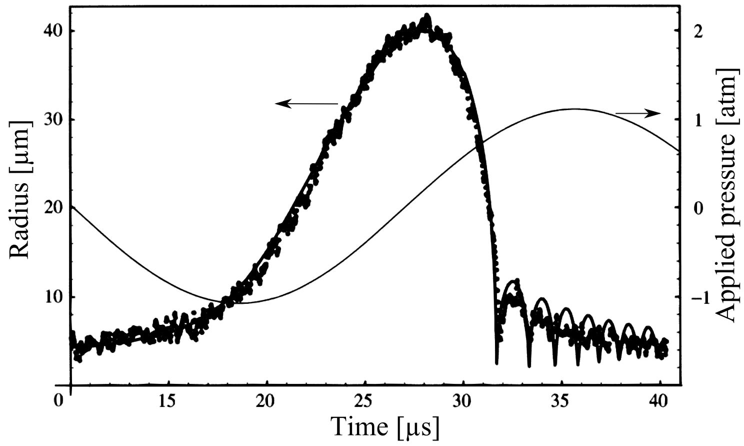

Figure 2.1: Mie scattering measurements of a pulsating bubble and a model for bubble dynamics[25]. Reproduced with permission of The Royal Society.

Single-bubble sonoluminescence

A single sonoluminescing bubble is created by introducing an initial gas bubble in a vessel filled with partially degassed liquid subjected to a standing wave that matches the vessel in dimensions[6,25,26]. A bubble of a specific size is trapped in the antinode of the sound field by the primary Bjerknes force, which is created by action of the compression and rarefaction waves of the sound field on the bubble[27]. The oscillating pressure also displaces the bubble wall. Rarefaction waves increase the bubble radius up to a maximum radius after which the bubble subsequently collapses. The compression creates a hot spot with a high pressure and temperature, and radiation is emitted. Several after-bounces with a rarefaction and a compression phase take place after the first collapse (see Figure 2.1). The unique opportunities in understanding and studying the processes taking place during bubble collapse offered by

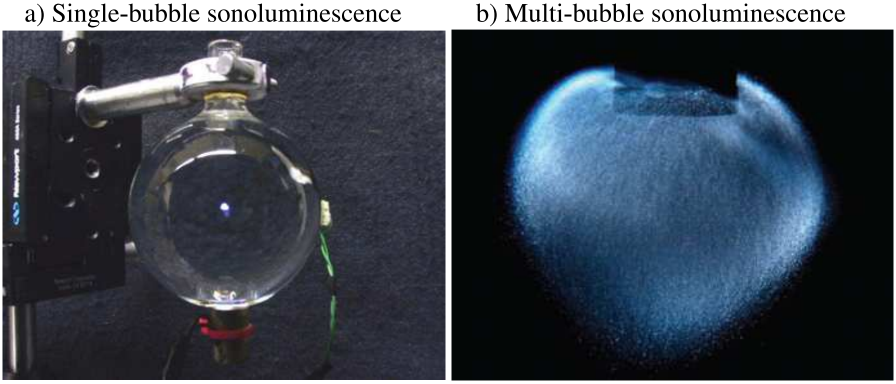

Figure 2.2: Images of a) single-bubble sonoluminescence in 85 wt % H_2SO_4 partially regassed with xenon and b) Multi-bubble sonoluminescence in 96 wt % H_2SO_4 saturated with xenon[5]. Single-bubble sonoluminescence can be seen in a fully lit room a). No external lighting is supplied in image b). Reproduced with permission of Annual Reviews.

the well-controlled case of SBSL have been quickly recognised and many studies on this phenomenon were published after the first report[26].

Experimental observations of oscillating single bubbles have been done by performing measurements on bubble size[25,28], emitted light spectrum[3,21,29], or collapse-induced chemistry[30]. Temperatures up to 15000 K were fitted to SBSL experiments in H_2SO_4 and argon to the black body and argon line emission[3]. The heavier noble gases such as xenon, and to a lesser extent krypton, give the highest hot spot temperatures[3]. Line emission is only observable when the bubble collapse is relatively dim and therefore not overshadowed by black body emission[3,21,29].

The time at which the radiation is emitted and its duration are correlated with the bubble collapse. Gompf *et al.* varied the oxygen concentration in the liquid between 0.5 and 3.3 mg L^{-1} and the driving pressure between 1.14 and 1.27 bar[31]. Hiller *et al.* varied the air pressure between 2.6 and 20 kPa[32]. The SBSL flash under these conditions has a full width at half maximum of 40 – 350 ps. Its duration scales with the gas concentration in the liquid and the driving pressure[31,32]. The bubble temperature can be estimated by fitting a black body temperature or another physical emission mechanism temperature to the emitted radiation.

The oscillating bubble has less chance to fragment during collapse and a longer life time in a single-bubble experiment than in a multi-bubble experiment. Other mechanisms therefore determine the bubble gas contents. Rectified diffusion over many cycles changes the gas content inside the single oscillating bubble[33]. Löfstedt *et al.* showed a decrease in bubble radius at increasing driving pressure[28], and attributed this to an unknown mass ejection mechanism (see Fig. 2.3). Brenner *et al.* interpreted the decrease of the bubble radius being caused by oxidation of nitrogen. The products of this reaction subsequently diffuse out of the bubble[34]. The bubble mainly consists of argon after several cycles. Matula and Crum[35] showed that the luminescence of an air bubble subjected to ultrasound increased initially from the luminescence of a pure nitrogen bubble to the luminescence of a pure argon bubble.

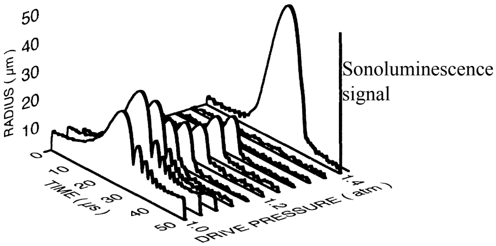

Figure 2.3: Transition to from non-sonoluminescing bubbles to a sonoluminescing bubble for a 0.1 % xenon bubble by increasing the driving pressure[28]. A mass ejection mechanism takes place at increasing acoustic pressures, where more mass is ejected when the drive pressure is increased up to 1.4 bar. At 1.4 bar the threshold for transition between no SL and stable SL is passed and xenon is rectified inside the bubble. The bubble increases in size and SL emission starts when this happens. Reproduced with permission of APS.

The level of degassing is important for the stability of the bubble. The bubble is positionally unstable if the gas content in the liquid is too high (see Fig. 2.4 for a phase diagram of bubble stability). Brenner *et al.* investigated the parameter space of gas concentration and sound amplitude and concluded that there are specific regions that yield either stable, unstable, or no SL[34]. Especially the region that sustains stable SL is small. Shape instabilities occur in the unstable region, resulting in ejection of micro bubbles and irregular motion of the original bubble. The gas concentrations at which stable SL can be realised is higher in degassed air solutions than in degassed argon solutions, since argon initially takes up only 1 % of an air bubble. The other components initially present in the bubble, nitrogen and oxygen, mostly react and diffuse out of the bubble during the life time of the bubble.

In summary, SBSL is a very suitable technique to investigate cavitation. The collapse conditions are well controlled and the reproducibility is high, and effects that take place over a longer period of time, hundreds or thousands of acoustic cycles, such as rectified diffusion become measurable. A gas content of the heavier noble gases such as xenon or krypton in the liquid results in the highest emission temperatures of up to 15000 K, with possibly even higher temperatures in the core[3].

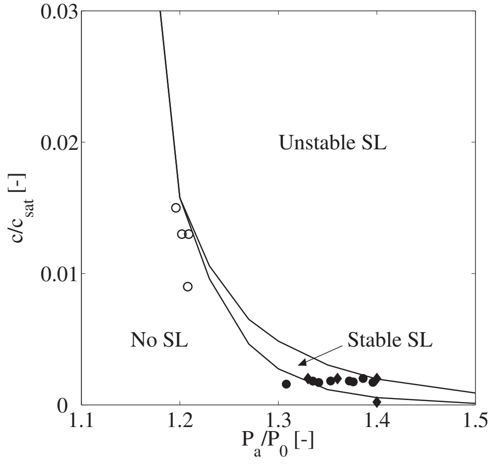

Figure 2.4: Parametric stability of SBSL in argon[34,36]. Open symbols: no SL, closed symbols: SL observed. The regions where SL is expected are indicated by the text. The frequency is 26.5 kHz, the initial bubble radius varies over the diagram. No SL takes place at low acoustic pressures P_a. Either stable or unstable SL starts when the pressure is increased and the bubble wall velocity at collapse reaches the speed of sound and forms a shock wave. Stable SL takes place in a very narrow gas concentration range, where c/c_{sat} is the gas concentration divided by the saturation gas concentration. The upper boundary for unstable SL is not displayed. Reproduced with permission of APS.

Multi-bubble sonoluminescence

In MBSL, luminescence is created by a cloud of oscillating bubbles. The liquid is usually not degassed. Bubbles are grown from the nuclei that are already present, by action of the sound field. Probing the bubble characteristics and sound field is more difficult in MBSL as compared to SBSL, since there are many bubbles which obscure each other and make the sound field spatially and temporally irregular by reflecting and emitting sound[37]. The bubbles do not survive many cycles due to these irregularities.

The hot spot temperature is mainly determined by the gas phase thermal properties such as heat capacity and thermal conductivity. Noble gases give a high luminescence intensity compared to other gases in MBSL due to their high adiabatic ratio of 1.67[38–43], just as in SBSL. Black body temperature fitting to the photon spectrum[39–42], and molecule line emissions[44–46] have been used to determine the temperature. Dissolving the heavier noble gases yields the highest measured intensity during collapse[41,42,47]. Didenko *et al.* have measured SL spectra of $Cr(CO)_6$ in octanol and dodecane solutions[44] and estimated temperatures during collapse. Besides changing the gas content, decreasing the liquid vapour pressure from 200 to 1 Pa by changing the solution temperature increased the collapse temperature from 2300 to 4000 K for $Cr(CO)_6$ line emission in octanol solutions[48]. Addition of polyatomic gases with a low adiabatic ratio ($C_p/C_v = \gamma$) to the solution yields lower temperatures[48]. A

3 % addition of propane (γ = 1.13) to argon (γ = 1.67) gives a hot spot temperature decrease from 4700 K to 2500 K.

Table 2.1: Fitted temperatures to SL in octanol (at 285 K) and dodecane (at 298 K) solutions saturated with noble gas[44].

Noble gas	SL temperature in octanol (K)	in dodecane (K)
Helium	3800	2600
Neon	4100	
Argon	4300	3200
Kryption	4400	
Xenon	5100	3800

A model that includes the differences in thermal conductivity of the noble gases yielded a good fit of temperature and luminescence[49]. Wall *et al.*[50] studied MBSL and found a decrease in MBSL relative intensity from 2.8 to 1.0 at increasing salt concentration (0 – 7 mol L^{-1}). The gas solubility increased from 1 without salt addition to 14 mmol L^{-1} with salt addition and correlated with the observed luminescence. However, the mechanism through which this influence takes place could not be specified.

2.2.2 Sonochemistry

Sonochemistry is a chemical reaction started by action of an oscillating cavitation bubble. The temperature in the hot spot created by the collapse can be so high that molecular bonds are broken. Two radical molecules that have a free electron are formed in this process, which readily react afterwards. In the case of water $H^\bullet$ and $OH^\bullet$ are formed. Two radicals can combine with each other to form a new bond. The radical can also start a chain of reactions by breaking and simultaneously creating a new bond, releasing a new radical into the environment.

Luche *et al.*[51] made a distinction between ‘true’ sonochemistry when the reaction pathway was altered due to the cavitation hot spot, either by formation of radicals or by creating reactive intermediates from the starting compounds, and the ‘false’ effects which were caused by mechanical effects around the bubble, such as enhanced mixing. A similar distinction is made in this section, where radical-initiated reactions and effects induced by the mechanical motion of the oscillating bubbles are discussed separately.

Dosimetry

The term dosimetry originates from radiation physics but in this context refers to a popular way to measure radical production. A simple and easily measured reaction is carried out in an ultrasound set-up, and the results can be compared with those of other researchers. Potassium iodide (KI) dosimetry is often used[52–60]. The $OH^\bullet$ radical is scavenged by the iodide, forming I_3^- which is detected spectroscopically. A comparison between using air and argon as saturation gas at different frequencies is presented in Figure 2.5.

All reports found on KI oxidation with varying saturation gases report a higher efficiency at 20 kHz when using argon than when using air. Higher efficiencies have been obtained at frequencies above 20 kHz using air[52–56]. This increase in radical production rate at high frequencies using air or oxygen[61,62] is not observed by Iida *et al.*[63] in the case of Fricke dosimetry in argon and air-saturated solutions. Fricke dosimetry is the measurement of the reduction of Fe^{2+} to Fe^{3+} by $OH^\bullet$, $HO_2^\bullet$, and H_2O_2.

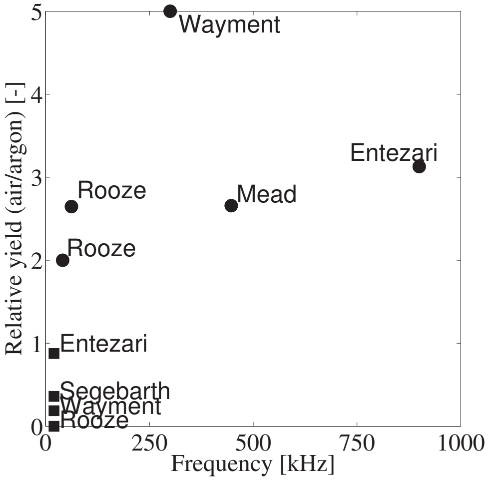

Figure 2.5: Relative KI oxidation yield, calculated by dividing the yield (in mol J^{-1}) under air by the yield under argon for several frequencies. The names of the first authors of the papers are shown in the figure. Filled squares: measurements at 20 kHz, filled circles: measurements at frequencies higher than 20 kHz.[52–56].

Hart and Henglein[64] measured combustion and H_2O_2 yield using Fricke dosimetry and the reduction of Cu^{2+} to Cu^{3+} by $HO_2^\bullet$, and found two maxima in the formation rate of the combustion products in gas mixtures of H_2 and O_2, one at 20 and one at 80 vol% of H_2. Pyrolysis of H_2 and O_2 due to the high temperatures and subsequent recombination was considered the most important mechanism for the formation of products. The maxima were caused by combined effects of thermal conductivity and heat capacity of the gas in the cavitation events, and by changes in chemical composition in the gas phase. The two maxima in hydrogen peroxide formation rate were later reproduced theoretically by Gong and Hart[65], combining the Rayleigh-Plesset modelling and chemical kinetics.

Breakdown of target molecules

Breakdown of undesired molecules is an well-studied application of cavitation chemistry, for example in water remediation[11,12,66]. A comparison of the effect of different gases on component breakdown using data from literature is not straightforward, because different operating conditions, such as contaminant properties, ultrasound frequency, sonicated volume, and ultrasound power were used. An overview of breakdown reactions in water is given in Table 2.2, with the target molecule, frequency, power, volume, initial concentration, and the ratio of efficiency under air to that under argon.

Molecules containing halogens are more efficiently broken down under argon, and those without halogens are more efficiently degraded under air. Possible mechanisms for this difference will be presented in Section 2.3.2.

Other reactions

Comparative rate thermometry Comparative rate thermometry is used to estimate collapse temperatures. Reaction rates for several parallel reactions are measured with this technique. The temperature is subsequently fitted using Arrhenius equations for reaction rates, which are temperature dependent. It is assumed in this approach that formation takes place through a limited number of pathways, and that the reaction products are not decomposed by the high temperatures[5]. Suslick *et al.*[80] found a direct dependency of the reaction rate for sonolysis of $Fe(CO)_5$ on its partial pressure with an excess of triphenylphosphine. Two sites of chemical activity were found, one in the gas with a fitted temperature of 5200 K and one in the liquid with a fitted temperature of 1900 K, with a boundary thickness of $\approx$ 270 nm in the radial direction from the bubble. Okitsu *et al.* analysed the kinetics of pyrolysis of t-butane (see Fig. 2.6)[81]. Interestingly, a constant bubble temperature, but different radical production rate was observed under the noble gases helium, neon, argon, krypton, and xenon. These seemingly contradicting terms were attributed to a difference in solubility of these gases. With a changing solubility the number of active bubbles also changes. These results are not in line with the experimental results from Flannigan *et al.* who measured SBSL with mixed gases[3]. They found varying temperature when varying the dissolved gas. Also an influence of the dissolved gas was found, but this was explained by a difference in thermal conductivity.

Table 2.2: Overview of reports on component breakdown in water using air and argon as saturation gases.

Component	Formula	f [a] (kHz)	Power (W)	Volume (mL)	C_0 [b] (mmol L^{-1})	k_{argon} [c] (×10^2 min^{-1})	k_{air} [c] (×10^2 min^{-1})	$k_{\mathrm{air}}/k_{\mathrm{argon}}$ [c] (-)	Ref.
Alizarin	$C_{14}H_8O_4$	20	80	50	0.005	2.2	2.5	1.14	[67]
Cyanide	HCN	20	80	200	0.55	1.3	3.1	2.43	[67]
Phenol	C_6H_6O	20	100	150	1	0.010	0.014	1.34	[68]
4-Hydroxybenzoic acid	$C_7H_6O_3$	200	200	65	0.1	2.6	5.5	0.61	[69]
Gallic acid	$C_7H_6O_5$	200	200	65	0.1	2.6	5.5	2.12	[69]
Tannic acid	$C_{76}H_{52}O_{46}$	200	200	65	0.1	6.4	16	2.56	[69]
Phenol	C_6H_6O	300	14.7	100	5	0.34	1	3.00	[70]
Bisphenol-A	$C_{15}H_{16}O_2$	300	80	300	0.12	2.8	3.1	1.09	[71]
Bisphenol-A	$C_{15}H_{16}O_2$	300	19	100	0.01	8.5	9.2	1.09	[72]
Alachlor	$C_{14}H_{20}ClNO_2$	300	1.9	10	0.1	3.6	1.2	0.33	[73]
Pentachlorophenol	C_6HCl_5O	200	200	65	0.1	6.4	4.5	0.92	[74]
3-Chlorophenol	C_6H_5ClO	200	200	65	0.1	7.2	6.6	0.91	[74]
2,4-Dichlorophenol	$C_6H_4Cl_2O$	489	20	50	3	4.5	2.6	0.57	[75]
MCPA[e]	$C_9H_9ClO_3$	500	21.4	100	0.5	2.75	4.67	1.70 [d]	[76]
Trichloroethylene	$C_2H_3Cl_3$	520	14	150	0.005	6.2	3.8	0.62	[77]
Chlorobenzene	C_6H_5Cl	520	14	150	0.001	2.9	1.8	0.63	[78]
Pentachlorophenate	$C_6HCl_5O^-Na^+$	530	13.3	100	0.1	0.24	0.15	0.64	[79]

[a] Frequency (f).

[b] Initial concentration (C_0).

[c] First order rate constant of breakdown (k).

[c] The dechlorination of the target compound is higher under argon, overall breakdown is higher under air.

[d] (4-Chloro-2-methylphenoxy) acetic acid

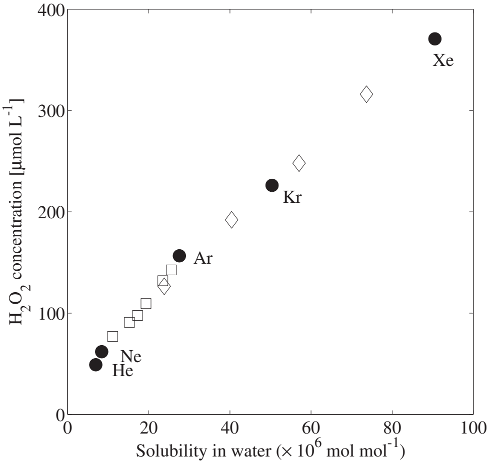

Figure 2.6: The hydrogen peroxide concentration after 30 minutes irradiation at 20 °C as a function of total gas solubility in water. Closed symbols are the noble gases helium, neon, argon, krypton, and xenon, open symbols are mixtures of helium and argon (squares) and mixtures of helium and xenon (diamonds). Adapted from[81]. Reproduced with permission of ACS.

Chemiluminescence Chemiluminescence is the emission of light due to chemical reactions, and can be created by luminol (5-Amino-2,3-dihydro-1,4-phthalazinedione). Luminol reacts with $OH^\bullet$ and $O_2^{-\bullet}$ radicals and subsequently rearranges[82]. Light is emitted during this rearrangement. Since sonochemiluminescence (SCL) is started by radicals, similar gas-induced effects as in radical dosimetry are expected. The radicals transfer to the liquid phase, making the process visible over a larger area than sonoluminescence (see Fig. 2.7).

The oxygen concentration in the solution and the effect of degassing and regassing on luminescence in luminol solutions have been investigated[84–86]. A solution with an oxygen content below saturation was exposed to pulsed ultrasound. No photon emission was observed during the first pulses, and it took a longer time to reach the photon emission steady state[84]. The same behaviour was observed for continuous ultrasound[85,86]. Hatanaka *et al.*[87] observed light emission in the presence of luminol only when the bubble showed irregular motion and emitted small bubbles. The same dancing bubble under oxygen gave a higher number of photon counts than under N_2 or 1% Xe in N_2. Sonoluminescence was only observed with a stable oscillating bubble.

Addition reactions Van Iersel *et al.*[88] studied chlorine addition to low molecular weight hydrocarbons using 20 kHz ultrasound. The usage of chlorine in radical reactions is convenient since the chlorine bond is easily broken and yields two reactive chlorine radicals. The reactants methane and chlorine were fed to the reactor by the gas phase in low concen-

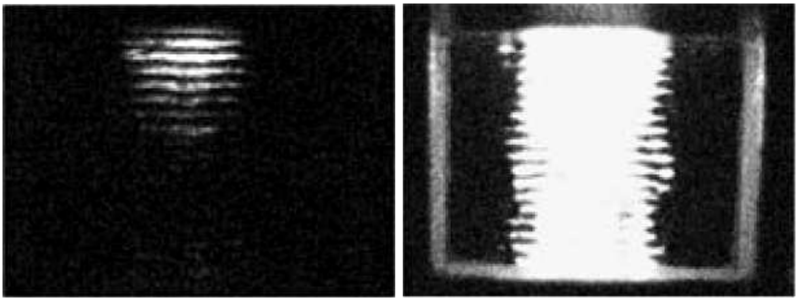

(a) Sonoluminescence (b) Sonochemiluminescence

Figure 2.7: Comparison of sonoluminescence (a) and sonochemiluminescence (b) in a 1 L vessel sonicated at 170 kHz and 20 W[83]. Sonochemiluminescence is the reaction of $OH^\bullet$ with the compound luminol. Light is emitted in subsequent rearrangement reactions. The volume where radical production and thus sonochemiluminescence is found overlaps the volume where sonoluminescence is found. Reproduced with permission of Wiley.

trations. Concentrations of the third gas, argon, of around 80 % were used to obtain hot spot temperatures high enough for reaction. The radical formation rate in this reaction was 2.46 µmol $min^{-1}W^{-1}$ at the optimum gas content. Supeno and Kruus[89] created ammonia in cavitation bubbles using 20, 850, and 900 kHz ultrasound in N_2 and H_2 sparged water. The highest radical formation rate of 4 nmol $min^{-1}W^{-1}$ was found at the lowest temperature measured, 278 K. Moisy *et al.* investigated the formation of HNO_2 from NO, NO_2, and argon bubbles in water[90]. The NO and NO_2 concentrations were below 1.7 vol%. The authors assumed that the bubble thermal properties were equal to those of a pure argon bubble. A maximum formation rate for HNO_2 of 3.3 µmol $W^{-1}min^{-1}$ under 1.7 vol% NO_2 and Ar was measured. In summary, ultrasound-induced cavitation processes can be used to perform addition reactions, but suffers from a low overall reaction rate. Reaction rates of up to 5 µmol $W^{-1}min^{-1}$ have been demonstrated in the works described above.

2.2.3 Mechanical effects induced by cavitation

The oscillation of a cavitation bubble induces liquid flow around it. This effect can be used to beneficially alter processes by local and intense mixing. Strain forces are created on long molecules at and near the bubble wall during a collapse[13]. These can be sufficient to break bonds inside the molecule. This feature is used to control the size distribution of a polymer. Shear forces and liquid jets can occur around the collapsing bubble and can affect surfaces nearby.

Therapeutical applications Current medical applications of ultrasound often make use of the mechanical effects of cavitation. Contrast agents used in echoscopic measurements are gas bubbles with a shell around it consisting of protein, surfactants, and other materials[91–96]. The size of the microbubbles should be below 10 µm for them to be able to pass the lung capillaries. Echoscopic imaging is done by applying a sound field to the region of interest so that the bubbles are driven nonlinearly. Higher and lower harmonics emitted by the bubbles are then measured. The microbubbles can also be destroyed by the ultrasound if the drive pressure is high enough[97], and they are then fragmented into smaller bubbles around which the shell partly reforms[94]. Poration and destruction of neighbouring cells can be achieved during the destruction of the bubble, most likely through mechanical action of a liquid jet. More radicals are formed around the microbubbles than in free solution because the microbubbles serve as nucleation sites, but the radicals do not play a large role in cell killing or poration[92,98–100]. The gas inside the microbubbles often is a perfluorocarbon which has a low solubility in water and blood so that the bubble is stable over time. The relatively high adiabatic index of these gases can also suppress radical formation.

Polymer breakdown Polymer breakdown can be achieved by the mechanical forces that occur during cavitation[13]. The oscillation dynamics of the bubble are important in this process rather than the thermal or chemical properties of the gas phase in the bubble, and the gas solubility seems to be crucial[101–104]. The gases with a higher solubility are less effective in breaking down polymer molecules, resulting in a higher remaining molecular weight. This is because the forces induced by the bubble collapse using these gases are less strong. The bubble collapse is cushioned because there is a higher gas concentration gradient and mass transfer between the liquid and the gas. Henglein and Gutiérrez observed that recombination of the polymer chains was inhibited when 10 vol % O_2 was added to Ar, because the polymer radicals were terminated by oxygen radicals[103]. Kruus *et al.*[105] studied the influence of saturation gas on polymerisation initiation in styrene, and observed a difference in polymerisation rate between transient cavitation in the absence of saturation gas and stable cavitation when gas was bubbled through the solution. Transient cavitation yielded high hot spot temperatures and therefore high rates of polymer pyrolysis and breakdown by mechanical forces. Stable cavitation yielded lower but sufficiently high hot spot temperatures for polymerisation initiation.

Cleaning The mechanical effects of a cavitation bubble are also used to clean materials, which happens either by streaming or by jetting. A collapsing bubble near a wall forms a jet, which can subsequently erode the wall[106]. Cleaning action in an ultrasonic bath and the damaging of ship propellers are examples of processes driven by cavitating jets. Cleaning of particles adhered to a surface is achieved with shear forces, which are induced by bubbles oscillating near a wall at high frequencies. Fluid is sucked towards, and ejected away from the bubble and from the wall [14,107]. The local high velocities near the wall give high shear rates, which can remove particles from the surface. Degasification of the liquid is detrimental to this process [108,109]. Hauptmann *et al.* applied an acoustic pressure to a cleaning jet and found the highest cleaning efficiency with oxygen at supersaturation [109]. A higher acoustic power was needed at high gas concentrations because the gas bubbles formed clusters and reflect the sound, thereby lowering the acoustic field amplitude.

2.3 The effects of dissolved gas on cavitation

2.3.1 Physical properties

Adiabatic ratio The adiabatic ratio $\gamma = C_p/C_v$ of the gas contents of a luminescing bubble mainly determines the hot spot temperature. High hot spot temperatures are obtained if he adiabatic ratio is high. Equation 2.1 is obtained assuming adiabatic compression in an ideal gas [49,110]:

$$T_{\text{collapse}} = T_0 \left(\frac{R_{\max}}{R_{\text{collapse}}} \right)^{3(\gamma-1)} \tag{2.1}$$

Where T is the temperature, and R is the bubble radius

For noble gases the γ ratio is high, 1.67, and therefore these saturation gases yield the highest temperatures. Eq. 2.1 gives a temperature of 4600 K for nitrogen ($\gamma = 1.4$), and a temperature of 30000 K for a noble gas ($\gamma = 1.67$), assuming an initial temperature of 293 K and a ratio of maximum and collapse radius of 10. Similarly, the vapour pressure of the liquid which usually has a lower adiabatic ratio than the gas is important in determining the collapse temperature [59,111]. The temperatures calculated by Equation 2.1 are upper limits. Heat transport by conduction out of the bubble and heat absorption by phase change or endothermic chemical reactions lower the final temperature.

Thermal conductivity The experiments with heavier dissolved noble gases such as xenon, krypton, and argon give higher temperatures in sonoluminescence experiments [3,30,112]. The smaller gases such as helium and neon have a high thermal conductivity making heat transfer from the hot centre of the bubble to the ambient liquid surroundings faster, and the bubble temperature lower. This effect is modelled by applying the heat equation to a bubble at collapse conditions.

Hilgenfeldt *et al.* [23] used the dimensionless Péclet number, the ratio of the rate of advection to the rate of diffusion, to quantify the importance of heat conduction in sonoluminescing bubbles. Both heat capacity and heat conductivity were taken into account in their approach. The Péclet number was defined as Pe $=R|\dot{R}|/\alpha$. Pe becomes large at bubble collapse, and effectively this means that the collapse is adiabatic. The bubble temperature is at equilibrium with the surroundings during the expansion and first stages of the collapse. The adiabatic index was modified during the ultrasound cycle according to these insights: it is unity during isothermal stages, and equal to the adiabatic value of the bubble contents during collapse. This means that the bubble temperature remains at the ambient level during bubble growth, and increases during collapse. Hilgenfeldt *et al.* made a fit of the full analytical solution proposed by Prosperetti[113] for small oscillations and arrived at a formula which is also valid for nonlinear oscillations:

$$\gamma(\mathrm{Pe}) = 1 + (\gamma - 1)\mathrm{exp}\left(-\frac{5.8}{\mathrm{Pe}^{0.6}}\right) \tag{2.2}$$

This modification of γ only affects the calculations during the 0.5 ns around the collapse in a 20 kHz oscillation[23]. Bubble temperatures of about 20000 K were calculated for a 5 µm radius argon bubble driven at 1.3 bar and 20 kHz. Collapsing xenon bubbles gave a much higher calculated light intensity as compared to argon bubbles.

In a similar fashion the Fourier number (Fo, the ratio of the heat conduction to the thermal energy storage capacity of the bubble) can be used to illustrate temperature differences between two gases with different heat conduction after a certain time. The heat transfer resistance in the liquid phase is assumed to be negligible compared to heat conduction resistance in the bubble, and the bubble is considered to be stationary. This model is not an accurate physical description of a collapsing bubble but can be applied to compare the effects of gases with different heat conductivities. The dimensionless heat transfer equation of a spherical bubble in polar coordinates is solved using a Laplace transformation[114]. The difference in temperature between the noble gases during collapse is investigated by assuming there is no water vapor but only noble gas inside the bubble.

$$\theta = \frac{2}{\pi y}\sum_{n=1}^{\infty}\frac{(-1)^{n+1}}{n}\sin(n\pi y)e^{-n^2\pi^2\mathrm{Fo}} \tag{2.3}$$

In this equation θ is the dimensionless temperature $(T - T_{\mathrm{liq}})/(T_{\mathrm{collapse}} - T_{\mathrm{liq}})$, Fo is the Fourier number $\alpha t/R^2$, $\alpha = \kappa/(\rho C_p)$ is the gas thermal diffusivity, and y is the dimensionless radius, r/R.

Assuming a bubble with an initial temperature of 1000 K, a liquid temperature of 293 K, during a period of 5 ns, and a constant radius of 1 µm (the duration and bubble size are estimated from a collapsing bubble[115]), and the gas properties at 10 MPa and 1000 K (the tabulated values at the highest temperature and pressure in[116]). The temperature as a function of the distance from the bubble center is calculated with $\mathrm{Fo}_{\mathrm{He}}$=0.075 and $\mathrm{Fo}_{\mathrm{Ar}}$=0.009 (Figure 2.8). The thermal diffusivity α is the determining factor for bubble temperature after time t when comparing two noble gases. The Fourier time is the only variable changing with gas properties. The Fourier time is 8.3 times higher for helium than for argon. Therefore the temperature is more developed towards the temperature of the surrounding liquid (T_{liq}) in the case of helium. The temperature in the centre of the helium bubble of 900 K is lower than that in the centre of the argon bubble (T = T_0 = 1000 K). The thermal diffusivity increases at increasing temperatures resulting in longer Fourier times and a more developed temperature profile inside the gas. The lower temperatures inside a gas bubble with a higher heat conductivity results in less intensive emission of light and a lower black body emission temperature of SBSL.

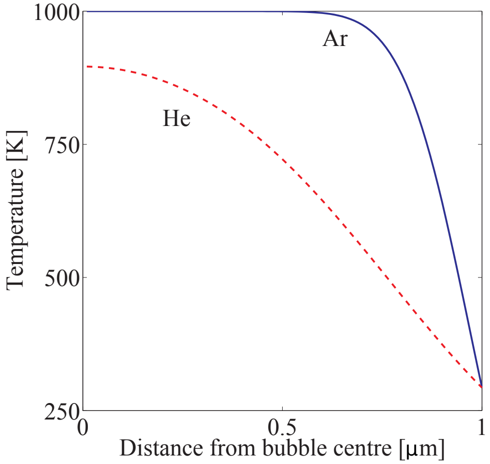

Figure 2.8: Analytical solution of the heat equation for spherical stagnant argon and helium bubbles with a radius of 1 µm with an initial temperature of 1000 K. The temperature distribution is plotted after 5 ns exposure to the ambient surroundings. The argon bubble temperature is higher than the helium bubble temperature due to differences in heat conduction.

Other mechanisms Moss *et al.* derived a model that incorporates the damping of the gas and vapour on the bubble collapse which better described experimental data on single-bubble collapse than previous models. An increased number of gas molecules in the bubble, either by a higher vapour pressure or by a higher gas pressure inside the bubble dampens the bubble oscillation[19]. Several articles describe the effect of solubility on cavitation. The effect has been measured using several methods, such as MBSL spectrum measurement, chemical, and polymer scission measurements, and comparative rate thermometry[50,81,101]. Enhanced gas transport into the bubble due to higher partial pressures can cushion the collapse[110,117,118].

Storey & Szeri and Yasui argued that segregation of species occurs during collapse[119–121]. Lighter molecules migrate to the centre of the bubble due to thermal and pressure diffusion. This can affect for example the light emission in a SL bubble, although the effect on the temperature distribution is small[119]. Yasui suggested that a difference in light emission from SL bubbles of various noble gases arises from the differences in the enthalpy of ionisation of the noble gases[121]. The heavier noble gases xenon and krypton are ionised more easily and therefore have a greater light emission from ion recombination and Bremsstrahlung.

2.3.2 Chemical properties

A chemical enhancement is responsible for the measured increase in cavitation oxidation efficiency when using air as a dissolved gas. The presence of oxygen in sonicated solutions generally gives an increase in radical production. Multiple chemical reaction paths are offered by the diradical oxygen. Scavenging of $H^\bullet$ by O_2 in aqueous systems and the subsequent reaction to H_2O_2 give a higher radical utilisation. The chemical reactions primarily take place inside the collapsing bubble, and radicals subsequently diffuse into the liquid.

There is a difference in oxidation rates between target molecules that contain halogens (bottom part of Table 2.2) and those without halogens (upper part of the Table 2.2). The target molecules containing halogen atoms have a higher decomposition rate under argon, whereas halogen-free compounds show a higher decomposition rate under air. Two different mechanisms can occur during component breakdown with ultrasound. Direct pyrolysis of the target component is favourable when there are molecular bonds with low dissociation energies, *e.g.* carbon-halogen bonds. An indirect mechanism through an $\mathrm{OH}^\bullet$ or an $\mathrm{H}^\bullet$ intermediate becomes likely when the temperature is high enough to break the molecular bonds of the solvent (water). Radical-induced breakdown may become more important when the initial concentration of target molecules decreases[122].

The hot spot temperature in argon-saturated solutions is expected to be higher than that in air-saturated solutions due to similarities with SL experiments described in Section 2.2. Apparently the maximum hot spot temperature does not necessarily match with the maximum radical production in multi-bubble fields. An addition in low quantities (<30 vol%) of molecules that easily dissociate, such as O_2 or Cl_2, promotes radical formation even though the hot spot temperature decreases[43,123,124]. The type of breakdown mechanism is important in optimisation of the gas type and content for the decomposition of molecules. High hot spot temperatures are desired when the target molecule is split by pyrolysis. The carbon-chlorine bonds are prone to destruction by pyrolysis, as is suggested by Table 2.2. An optimum gas concentration for radical production is obviously desired when the destruction mechanism is radical based. A mixture with an Ar/O_2 volumetric ratio of 1.4 – 4 gives the highest hot spot temperature and radical production rate[43,125,126].

2.3.3 Effect of gas on nucleation and stability

The amount of dissolved gas in the liquid has an impact on the bubble nucleation rate; when the amount of gas is increased, the nucleation rate also increases[127–129]. This is likely due to the lowering of the surface tension of the liquid by solution of the gas, although many other possible explanations have been proposed[127]. The more soluble the gas, the more it reduces the surface tension, and the higher the nucleation rate[127]. A lowered surface tension also decreases the tensile strength needed for bubble growth[37,130]. On the other hand lowering the surface tension decreases the intensity of the cavitation effects such as sonoluminescence[131,132] because of a decrease in shape stability. A single oscillating bubble shows jittery motion if the gas content in the liquid is too high – micro bubbles are ejected from the original bubble in this regime[34], and this ejection creates an extra force on the bubble wall. These micro bubbles do not show luminescence, but their collapse creates radicals[87]. There is an increased mass transport rate into the liquid due to the small size and short life time of the micro bubbles, even though their hot spot temperature is lower.

A change in the number of bubbles can alter the overall effects of a multi-bubble cavitation field as well. By increasing the number of bubbles secondary shielding effects can occur[133–135], thereby lowering the radical production rate. Increasing the number of bubbles can be achieved by reducing the surface tension by using a gas with a higher solubility in the liquid[81], by addition of a surfactant[136,137] or by addition of salts[50,132,138–141]. The small bubbles can subsequently grow to bubbles of resonant size which display nonlinear motion.

2.4 Conclusions

The gas content of cavitating bubbles has been a topic of interest for many researchers, both in an experimental sense as well as theoretically. The adiabatic ratio and heat conductivity mainly determine the hot spot temperature. The higher the adiabatic and the lower the heat conduction, the higher the hot spot temperature, and the more pronounced are its effects, such as sonoluminescence and radical formation. Adding gas to a liquid lowers its surface tension, thereby increasing nucleation but decreasing shape stability of the bubbles.

The gas molecules in the bubble can participate in chemical reactions and can form new radical species and components. Adding molecules that easily form radicals, such as oxygen, can increase radical production, although the hot spot temperature may be lowered by this addition, *i.e.* the maximum in radical production does not necessarily coincide with the maximum hot spot temperature.

2.5 Outlook

The effect of a dissolved gas on cavitation processes can be explained at least qualitatively. A number of research questions in this topic are still open. Most prominent among these is the measurement of temperature and pressure inside the bubble. Especially single bubble experiments give a tantalising hint of the high temperature physics that take place inside the opaque core of the collapsing bubble. Most insight can be expected from single-bubble experiments since these are the most controlled. These insights can then be translated to or tested in multi-bubble experiments. Cavitation in non-aqueous solvents, for example H_2SO_4, opens up new views on the topic, not only through altering the liquid properties but also through altering the cavitation bubble gas phase properties. Theoretical calculations of bubble radii with validation in various solvents and gas types may provide more insight into the precise bubble contents. More insight into the behaviour of micro bubble pinch off would be interesting in descriptions of cavitation since these both the original and the ejected bubbles behave differently than stable bubbles in terms of radical production. The composition of the gas content in the collapsing bubble is of interest as well. Experiments with different gas mixtures are an effective tool to probe the relations of gas with the cavitation process, although the actual gas concentrations inside the cavitation bubble are not known.

Bibliography

[1] T. G. Leighton, The acoustic bubble, Academic Press, London, 1994.
[2] F. R. Young, Cavitation, McGraw-Hill, London, 1989.
[3] D. J. Flannigan, K. S. Suslick, Plasma formation and temperature measurement during single-bubble cavitation, Nature 434(7029) (**2005**) 52–55. `doi:10.1038/nature03361`.
[4] R. Hiller, S. J. Putterman, B. P. Barber, Spectrum of synchronous picosecond sonoluminescence, Physical Review Letters 69(8) (**1992**) 1182–1184. `doi:10.1103/PhysRevLett.69.1182`.
[5] K. S. Suslick, D. J. Flannigan, Inside a collapsing bubble: sonoluminescence and the conditions during cavitation, Annual Review of Physical Chemistry 59(1) (**2008**) 659–683. `doi:10.1146/annurev.physchem.59.032607.093739`.
[6] M. P. Brenner, S. Hilgenfeldt, D. Lohse, Single-bubble sonoluminescence, Reviews of Modern Physics 74(2) (**2002**) 425–484. `doi:10.1103/RevModPhys.74.425`.
[7] S. J. Putterman, K. R. Weninger, Sonoluminescence: How bubbles turn sound into light, Annual Review of Fluid Mechanics 32(1) (**2000**) 445–476. `doi:10.1146/annurev.fluid.32.1.445`.
[8] R. Finch, Sonoluminescence, Ultrasonics 1(2) (**1963**) 87–98. `doi:10.1016/0041-624X(63)90060-X`.

[9] K. S. Suslick, G. J. Price, Applications of ultrasound to materials chemistry, Annual Review of Materials Science 29(1) (**1999**) 295–326. `doi:10.1146/annurev.matsci.29.1.295`.

[10] T. J. Mason, Sonochemistry: the uses of ultrasound in chemistry, Royal Society of Chemistry Cambridge, 1990.

[11] J. Lifka, B. Ondruschka, J. Hofmann, The use of ultrasound for the degradation of pollutants in water: Aquasonolysis - a review, Engineering in Life Sciences 3(6) (**2003**) 253–262. `doi:10.1002/elsc.200390040`.

[12] J. González-García, V. Sáez, I. Tudela, M. I. Díez-Garcia, M. Deseada Esclapez, O. Louisnard, Sonochemical treatment of water polluted by chlorinated organocompounds. A review, Water 2(1) (**2010**) 28–74. `doi:10.3390/w2010028`.

[13] A. M. Basedow, K. H. Ebert, Ultrasonic Degradation of Polymers in Solution, Springer-Verlag, Berlin, 1977.

[14] P. Marmottant, M. Versluis, N. de Jong, S. Hilgenfeldt, D. Lohse, High-speed imaging of an ultrasound-driven bubble in contact with a wall: "Narcissus" effect and resolved acoustic streaming, Experiments in Fluids 41 (**2006**) 147–153. `doi:10.1007/s00348-005-0080-y`.

[15] C.-D. Ohl, T. Kurz, R. Geisler, O. Lindau, W. Lauterborn, Bubble dynamics, shock waves and sonoluminescence, Philosophical Transactions: Mathematical, Physical and Engineering Sciences 357(1751) (**1999**) 269–294.

[16] C.-D. Ohl, M. Arora, R. Ikink, N. de Jong, M. Versluis, M. Delius, D. Lohse, Sonoporation from jetting cavitation bubbles, Biophysical Journal 91(11) (**2006**) 4285–4295. `doi:10.1529/biophysj.105.075366`.

[17] L. A. Crum, Nucleation and stabilization of microbubbles in liquids, Applied Scientific Research 38(1) (**1982**) 101–115. `doi:10.1007/BF00385941`.

[18] T. J. Mason, E. D. Cordemans, Ultrasonic intensification of chemical processing and related operations: a review, Transactions of the IChemE 74A (**1996**) 511–516.

[19] W. C. Moss, J. L. Levatin, A. J. Szeri, A new damping mechanism in strongly collapsing bubbles, Proceedings of the Royal Society of London. Series A: Mathematical, Physical and Engineering Sciences 456(2004) (**2000**) 2983–2994. `doi:10.1098/rspa.2000.0649`.

[20] W. C. Moss, D. B. Clarke, D. A. Young, Calculated pulse widths and spectra of a single sonoluminescing bubble, Science 276(5317) (**1997**) 1398–1401. `doi:10.1126/science.276.5317.1398`.

[21] N. C. Eddingsaas, K. S. Suslick, Evidence for a plasma core during multibubble sonoluminescence in sulfuric acid, Journal of the American Chemical Society 129(13) (**2007**) 3838–3839. `doi:10.1021/ja070192z`.

[22] W. C. Moss, D. A. Young, J. A. Harte, J. L. Levatin, B. F. Rozsnyai, G. B. Zimmerman, I. H. Zimmerman, Computed optical emissions from a sonoluminescing bubble, Physical Review E: Statistical, Nonlinear, and Soft Matter Physics 59(3) (**1999**) 2986–2992. `doi:10.1103/PhysRevE.59.2986`.

[23] S. Hilgenfeldt, S. Grossmann, D. Lohse, Sonoluminescence light emission, Physics of Fluids 11(6) (**1999**) 1318–1330. `doi:10.1063/1.869997`.

[24] K. Yasui, T. Tuziuti, M. Sivakumar, Y. Iida, Sonoluminescence, Applied Spectroscopy Reviews 39(3) (**2004**) 399–436. `doi:10.1081/ASR-200030202`.

[25] T. J. Matula, Inertial cavitation and single-bubble sonoluminescence, Philosophical Transactions: Mathematical, Physical and Engineering Sciences 357(1751) (**1999**) 225–249.

[26] D. F. Gaitan, L. A. Crum, C. C. Church, R. A. Roy, Sonoluminescence and bubble dynamics for a single, stable, cavitation bubble, The Journal of the Acoustical Society of America 91(6) (**1992**) 3166–3183. `doi:10.1121/1.402855`.

[27] T. G. Leighton, A. J. Walton, M. J. W. Pickworth, Primary Bjerknes forces, European Journal of Physics 11 (**1990**) 47–50. `doi:10.1088/0143-0807/11/1/009`.

[28] R. Löfstedt, K. Weninger, S. Putterman, B. P. Barber, Sonoluminescing bubbles and mass diffu-

sion, Physical Review E: Statistical, Nonlinear, and Soft Matter Physics 51(5) (**1995**) 4400–4410. doi:10.1103/PhysRevE.51.4400.

[29] J. B. Young, J. A. Nelson, W. Kang, Line emission in single-bubble sonoluminescence, Physical Review Letters 86(12) (**2001**) 2673–2676. doi:10.1103/PhysRevLett.86.2673.

[30] Y. T. Didenko, K. S. Suslick, The energy efficiency of formation of photons, radicals and ions during single-bubble cavitation, Nature 418(6896) (**2002**) 394–397. doi:10.1038/nature00895.

[31] B. Gompf, R. Günther, G. Nick, R. Pecha, W. Eisenmenger, Resolving sonoluminescence pulse width with time-correlated single photon counting, Physical Review Letters 79(7) (**1997**) 1405–1408. doi:10.1103/PhysRevLett.79.1405.

[32] R. A. Hiller, S. J. Putterman, K. R. Weninger, Time-resolved spectra of sonoluminescence, Physical Review Letters 80(5) (**1998**) 1090–1093. doi:10.1103/PhysRevLett.80.1090.

[33] A. Eller, H. G. Flynn, Rectified diffusion during nonlinear pulsations of cavitation bubbles, The Journal of the Acoustical Society of America 37(3) (**1965**) 493–503. doi:10.1121/1.1909357.

[34] M. P. Brenner, S. Hilgenfeldt, D. Lohse, Why air bubbles in water glow so easily, Nonlinear physics of complex systems – Current status and future trends, Springer Berlin, 1996, Ch. 8, pp. 79–97. doi:10.1007/BFb0105431.

[35] T. J. Matula, L. A. Crum, Evidence for gas exchange in single-bubble sonoluminescence, Physical Review Letters 80(4) (**1998**) 865–868. doi:10.1103/PhysRevLett.80.865.

[36] D. Lohse, M. P. Brenner, T. F. Dupont, S. Hilgenfeldt, B. Johnston, Sonoluminescing air bubbles rectify argon, Physical Review Letters 78(7) (**1997**) 1359–1362. doi:10.1103/PhysRevLett.78.1359.

[37] C. E. Brennen, Cavitation and Bubble Dynamics, Oxford University Press, 1995.

[38] R. O. Prudhomme, T. Guilmart, Photogénèse ultraviolette par irradiation ultrasonore de l'eau en présence des gaz rares, Journal de Chimie Physique 54 (**1957**) 336.

[39] D. Srinivasan, L. V. Holroyd, Optical spectrum of the sonoluminescence emitted by cavitated water, Journal of Applied Physics 32(3) (**1961**) 446–449. doi:10.1063/1.1736022.

[40] P. Günther, W. Zeil, U. Grisar, E. Heim, Versuche über die Sonolumineszenz wäßriger Lösungen, Zeitschrift für Elektrochemie 61(1) (**1957**) 188–201.

[41] K. R. Weninger, C. G. Camara, S. J. Putterman, Energy focusing in a converging fluid flow: Implications for sonoluminescence, Physical Review Letters 83(10) (**1999**) 2081–2084. doi:10.1103/PhysRevLett.83.2081.

[42] S. Hirayama, H. Morinaga, T. Ohmi, J.-I. Soejima, Sonoluminescence measurement of 1 MHz ultrasonic cavitation and effect of dissolved gases, Acoustical Science and Technology 29(6) (**2008**) 345–350. doi:10.1250/ast.29.345.

[43] M. A. Beckett, I. Hua, Impact of ultrasonic frequency on aqueous sonoluminescence and sonochemistry, The Journal of Physical Chemistry 105 (**2001**) 3796–3802. doi:10.1021/jp003226x.

[44] Y. T. Didenko, W. B. McNamara III, K. S. Suslick, Effect of noble gases on sonoluminescence temperatures during multibubble cavitation, Physical Review Letters 84(4) (**2000**) 777–780. doi:10.1103/PhysRevLett.84.777.

[45] Y. T. Didenko, W. B. McNamara III, K. S. Suslick, Temperature of multibubble sonoluminescence in water, The Journal of Physical Chemistry A 103(50) (**1999**) 10783–10788. doi:10.1021/jp991524s.

[46] W. B. McNamara III, Y. T. Didenko, K. S. Suslick, The nature of the continuum in multibubble sonoluminescence, Journal of the American Chemical Society 122(35) (**2000**) 8563–8564. doi:10.1021/ja001238q.

[47] H. Harada, N. Iwata, K. Shiratori, Observation of multibubble sonoluminescence from water saturated with various gases during ultrasonic atomization, Japanese Journal of Applied Physics

48(7) (**2009**) 07GH01. `doi:10.1143/JJAP.48.07GH01`.

[48] W. B. McNamara III, Y. T. Didenko, K. S. Suslick, Sonoluminescence temperatures during multi-bubble cavitation, Nature 401(6755) (**1999**) 772–775. `doi:10.1038/44536`.

[49] F. R. Young, Sonoluminescence from water containing dissolved gases, The Journal of the Acoustical Society of America 60(1) (**1976**) 100–104. `doi:10.1121/1.381076`.

[50] M. Wall, M. Ashokkumar, R. Tronson, F. Grieser, Multibubble sonoluminescence in aqueous salt solutions, Ultrasonics Sonochemistry 6(1–2) (**1999**) 7–14. `doi:10.1016/S1350-4177(98)00037-6`.

[51] J.-L. Luche, C. Einhorn, J. Einhorn, J. V. Sinisterra-Gago, Organic sonochemistry: A new interpretation and its consequences, Tetrahedron Letters 31(29) (**1990**) 4125–4128. `doi:10.1016/S0040-4039(00)97559-2`.

[52] N. Segebarth, O. Eulaerts, Y. Kegelaers, J. Vandercammen, J. Reisse, About the Janus double-horn sonicator and its use in quantitative homogenous sonochemistry, Ultrasonics Sonochemistry 9(2) (**2002**) 113–119. `doi:10.1016/S1350-4177(01)00112-2`.

[53] D. G. Wayment, D. J. Casadonte Jr., Design and calibration of a single-transducer variable-frequency sonication system, Ultrasonics Sonochemistry 9(4) (**2002**) 189–195. `doi:10.1016/S1350-4177(01)00127-4`.

[54] E. L. Mead, R. G. Sutherland, R. E. Verrall, The effect of ultrasound on water in the presence of dissolved gases, Canadian Journal of Chemistry 54 (**1976**) 1114–1120.

[55] M. H. Entezari, P. Kruus, Effect of frequency on sonochemical reactions. I: Oxidation of iodide, Ultrasonics Sonochemistry 1(2) (**1994**) S75–S79. `doi:10.1016/1350-4177(94)90001-9`.

[56] J. Rooze, E. V. Rebrov, J. C. Schouten, J. T. F. Keurentjes, Effect of resonance frequency, power input, and saturation gas type on the oxidation efficiency of an ultrasound horn, Ultrasonics Sonochemistry 18(1) (**2011**) 209–215. `doi:10.1016/j.ultsonch.2010.05.007`.

[57] D. V. Prasad Naidu, R. Rajan, R. Kumar, K. S. Gandhi, V. H. Arakeri, S. Chandrasekaran, Modelling of a batch sonochemical reactor, Chemical Engineering Science 49(6) (**1994**) 877–888. `doi:10.1016/0009-2509(94)80024-3`.

[58] T. Kondo, M. Kuwabara, F. Sato, E. Kano, Influence of dissolved gases on chemical and biological effects of ultrasound, Ultrasound in Medicine and Biology 12(2) (**1986**) 151–155. `doi:10.1016/0301-5629(86)90020-7`.

[59] K. S. Suslick, M. M. Mdleleni, J. T. Ries, Chemistry induced by hydrodynamic cavitation, Journal of the American Chemical Society 119(39) (**1997**) 9303–9304. `doi:10.1021/ja972171i`.

[60] M. M. van Iersel, Sensible sonochemistry, Ph.D. thesis, Eindhoven University of Technology (2008).

[61] G. Mark, A. Tauber, R. Laupert, H.-P. Schuchmann, D. Schulz, A. Mues, C. von Sonntag, OH-radical formation by ultrasound in aqueous solution – part II: Terephthalate and Fricke dosimetry and the influence of various conditions on the sonolytic yield, Ultrasonics Sonochemistry 5(2) (**1998**) 41–52. `doi:10.1016/S1350-4177(98)00012-1`.

[62] I. Hua, M. R. Hoffmann, Optimization of ultrasonic irradiation as an advanced oxidation technology, Environmental Science & Technology 31(8) (**1997**) 2237–2243. `doi:10.1021/es960717f`.

[63] Y. Iida, K. Yasui, T. Tuziuti, M. Sivakumar, Sonochemistry and its dosimetry, Microchemical Journal 80(2) (**2005**) 159–164. `doi:10.1016/j.microc.2004.07.016`.

[64] E. J. Hart, A. Henglein, Sonochemistry of aqueous solutions: hydrogen-oxygen combustion in cavitation bubbles, The Journal of Physical Chemistry 91(13) (**1987**) 3654–3656. `doi:10.1021/j100297a038`.

[65] C. Gong, D. P. Hart, Ultrasound induced cavitation and sonochemical yields, The Journal of the Acoustical Society of America 104(5) (**1998**) 2675–2682. `doi:10.1121/1.423851`.

[66] M. R. Hoffmann, I. Hua, R. Höchemer, Application of ultrasonic irradiation for the degradation of chemical contaminants in water, Ultrasonics Sonochemistry 3(3) (**1996**) S163–S172. `doi:10.1016/S1350-4177(96)00022-3`.

[67] Q. Hong, J. L. Hardcastle, R. A. J. McKeown, F. Marken, R. G. Compton, The 20 kHz sonochemical degradation of trace cyanide and dye stuffs in aqueous media, New Journal of Chemistry 23 (**1999**) 845–849. `doi:10.1039/a903990b`.

[68] T. Sivasankar, V. S. Moholkar, Mechanistic approach to intensification of sonochemical degradation of phenol, Chemical Engineering Journal 149(1–3) (**2009**) 57–69. `doi:10.1016/j.cej.2008.10.004`.

[69] Y. Nagata, K. Hirai, H. Bandow, Y. Maeda, Decomposition of hydroxybenzoic and humic acids in water by ultrasonic irradiation, Environmental Science & Technology 30(4) (**1996**) 1133–1138. `doi:10.1021/es950336m`.

[70] R. Kidak, N. Ince, Effects of operating parameters on sonochemical decomposition of phenol, Journal of Hazardous Materials 137(3) (**2006**) 1453–1457. `doi:10.1016/j.jhazmat.2006.04.021`.

[71] R. A. Torres, C. Pétrier, E. Combet, M. Carrier, C. Pulgarin, Ultrasonic cavitation applied to the treatment of bisphenol A. Effect of sonochemical parameters and analysis of BPA by-products, Ultrasonics Sonochemistry 15(4) (**2008**) 605–611. `doi:10.1016/j.ultsonch.2007.07.003`.

[72] I. Gültekin, N. H. Ince, Ultrasonic destruction of bisphenol-A: The operating parameters, Ultrasonics Sonochemistry 15(4) (**2008**) 524–529. `doi:10.1016/j.ultsonch.2007.05.005`.

[73] D. G. Wayment, D. J. Casadonte Jr., Frequency effect on the sonochemical remediation of alachlor, Ultrasonics Sonochemistry 9(5) (**2002**) 251–257. `doi:10.1016/S1350-4177(02)00081-0`.

[74] Y. Nagata, M. Nakagawa, H. Okuno, Y. Mizukoshi, B. Yim, Y. Maeda, Sonochemical degradation of chlorophenols in water, Ultrasonics Sonochemistry 7(3) (**2000**) 115–120. `doi:10.1016/S1350-4177(99)00039-5`.

[75] M. Helal Uddin, S. Hayashi, Effects of dissolved gases and pH on sonolysis of 2,4-dichlorophenol, Journal of Hazardous Materials 170(2–3) (**2009**) 1273–1276. `doi:10.1016/j.jhazmat.2009.05.130`.

[76] Y. Kojima, T. Fujita, E. P. Ona, H. Matsuda, S. Koda, N. Tanahashi, Y. Asakura, Effects of dissolved gas species on ultrasonic degradation of (4-chloro-2-methylphenoxy) acetic acid (MCPA) in aqueous solution, Ultrasonics Sonochemistry 12(5) (**2005**) 359–365. `doi:10.1016/j.ultsonch.2004.04.002`.

[77] D. Drijvers, R. de Baets, A. de Visscher, H. van Langenhove, Sonolysis of trichloroethylene in aqueous solution: volatile organic intermediates, Ultrasonics Sonochemistry 3(2) (**1996**) S83–S90. `doi:10.1016/1350-1477(96)00012-3`.

[78] D. Drijvers, H. van Langenhove, K. Vervaet, Sonolysis of chlorobenzene in aqueous solution: organic intermediates, Ultrasonics Sonochemistry 5(1) (**1998**) 13–19. `doi:10.1016/S1350-4177(98)00006-6`.

[79] C. Pétrier, M. Micolle, G. Merlin, J.-L. Luche, G. Reverdy, Characteristics of pentachlorophenate degradation in aqueous solution by means of ultrasound, Environmental Science and Technology 26(8) (**1992**) 1639–1642. `doi:10.1021/es00032a023`.

[80] K. S. Suslick, D. A. Hammerton, R. E. Cline, Sonochemical hot spot, Journal of the American Chemical Society 108(18) (**1986**) 5641–5642. `doi:10.1021/ja00278a055`.

[81] K. Okitsu, T. Suzuki, N. Takenaka, H. Bandow, R. Nishimura, Y. Maeda, Acoustic multibubble cavitation in water: A new aspect of the effect of a rare gas atmosphere on bubble temperature and its relevance to sonochemistry, Journal of Physical Chemistry B 110(41) (**2006**) 20081–20084. `doi:10.1021/jp064598u`.

[82] H. N. McMurray, B. P. Wilson, Mechanistic and spatial study of ultrasonically induced luminol chemiluminescence, The Journal of Physical Chemistry A 103(20) (**1999**) 3955–3962. `doi:10.1021/jp984503r`.

[83] M. Ashokkumar, J. Lee, Y. Iida, K. Yasui, T. Kozuka, T. Tuziuti, A. Towata, Spatial distribution of acoustic cavitation bubbles at different ultrasound frequencies, ChemPhysChem 11(8) (**2010**) 1680–1684. `doi:10.1002/cphc.200901037`.

[84] A. Henglein, D. Herburger, M. Gutiérrez, Sonochemistry: some factors that determine the ability of a liquid to cavitate in an ultrasonic field, The Journal of Physical Chemistry 96(3) (**1992**) 1126–1130. `doi:10.1021/j100182a020`.

[85] T. Tuziuti, K. Yasui, M. Sivakumar, Y. Iida, Influence of dissolved-air concentration on spatial distribution of bubbles for sonochemistry, Ultrasonics 44 (**2006**) e357–e361. `doi:10.1016/j.ultras.2006.05.002`.

[86] H. Yanagida, The effect of dissolve gas concentration in the initial growth stage of multi cavitation bubbles: Differences between vacuum degassing and ultrasound degassing, Ultrasonics Sonochemistry 15(4) (**2008**) 492–496. `doi:10.1016/j.ultsonch.2007.06.008`.

[87] S.-I. Hatanaka, H. Mitome, K. Yasui, S. Hayashi, Single-bubble sonochemiluminescence in aqueous luminol solutions, Journal of the American Chemical Society 124(35) (**2002**) 10250–10251. `doi:10.1021/ja0258475`.

[88] M. M. van Iersel, M. A. van Schilt, N. E. Benes, J. T. F. Keurentjes, Controlled methyl chloride synthesis at mild conditions using ultrasound irradiation, Ultrasonics Sonochemistry 17(2) (**2010**) 315–317. `doi:10.1016/j.ultsonch.2009.08.002`.

[89] Supeno, P. Kruus, Fixation of nitrogen with cavitation, Ultrasonics Sonochemistry 9(1) (**2002**) 53–59. `doi:10.1016/S1350-4177(01)00070-0`.

[90] P. Moisy, I. Bisel, F. Genvo, F. Rey-Gaurez, L. Venault, P. Blanc, Preliminary results on the effect of power ultrasound on nitrogen oxide and dioxide atmosphere in nitric acid solutions, Ultrasonics Sonochemistry 8(3) (**2001**) 175–181. `doi:10.1016/S1350-4177(01)00075-X`.

[91] K. Ferrara, R. Pollard, M. Borden, Ultrasound microbubble contrast agents: Fundamentals and application to gene and drug delivery, Annual Review of Biomedical Engineering 9(1) (**2007**) 415–447. `doi:10.1146/annurev.bioeng.8.061505.095852`.

[92] P. A. Dijkmans, L. J. M. Juffermans, R. J. P. Musters, A. van Wamel, F. J. ten Cate, W. van Gilst, C. A. Visser, N. de Jong, O. Kamp, Microbubbles and ultrasound: from diagnosis to therapy, European Journal of Echocardiography 5(4) (**2004**) 245–246. `doi:10.1016/j.euje.2004.02.001`.

[93] S. Hernot, A. L. Klibanov, Microbubbles in ultrasound-triggered drug and gene delivery, Advanced Drug Delivery Reviews 60(10) (**2008**) 1153–1166. `doi:10.1016/j.addr.2008.03.005`.

[94] K. W. Ferrara, M. A. Borden, H. Zhang, Lipid-shelled vehicles: Engineering for ultrasound molecular imaging and drug delivery, Accounts of Chemical Research 42(7) (**2009**) 881–892. `doi:10.1021/ar8002442`.

[95] V. Frenkel, Ultrasound mediated delivery of drugs and genes to solid tumors, Advanced Drug Delivery Reviews 60(10) (**2008**) 1193–1208. `doi:10.1016/j.addr.2008.03.007`.

[96] D. L. Miller, Overview of experimental studies of biological effects of medical ultrasound caused by gas body activation and inertial cavitation, Progress in Biophysics and Molecular Biology 93(1–3) (**2007**) 314–330. `doi:10.1016/j.pbiomolbio.2006.07.027`.

[97] A. Bouakaz, M. Versluis, N. de Jong, High-speed optical observations of contrast agent destruction, Ultrasound in Medicine & Biology 31(3) (**2005**) 391–399. `doi:10.1016/j.ultrasmedbio.2004.12.004`.

[98] T. Kondo, J. Gamson, J. B. Mitchell, P. Riesz, Free radical formation and cell lysis induced by ultrasound in the presence of different rare gases, International Journal of Radiation Biology 54(6) (**1988**) 955–962. `doi:10.1080/09553008814552351`.

[99] R. Ogawa, T. Kondo, H. Honda, Q. L. Zhao, S. Fukuda, P. Riesz, Effects of dissolved gases and an echo contrast agent on ultrasound mediated in vitro gene transfection, Ultrasonics Sonochemistry 9(4) (**2002**) 197–203. `doi:10.1016/S1350-4177(02)00075-5`.

[100] T. Kondo, E. Kano, Effect of free radicals induced by ultrasonic cavitation on cell killing, International Journal of Radiation Biology 54(3) (**1988**) 475–486. `doi:10.1080/09553008814551841`.

[101] G. J. Price, P. F. Smith, Ultrasonic degradation of polymer solutions: 2. The effect of temperature, ultrasound intensity and dissolved gases on polystyrene in toluene, Polymer 34(19) (**1993**) 4111–4117. `doi:10.1016/0032-3861(93)90675-Z`.

[102] H. W. W. Brett, H. H. G. Jellinek, Degradation of long chain molecules by ultrasonic waves. part v. cavitation and the effect of dissolved gases, Journal of Polymer Science 13(71) (**1954**) 441–459. `doi:10.1002/pol.1954.120137103`.

[103] A. Henglein, M. Gutiérrez, Sonolysis of polymers in aqueous solution. new observations on pyrolysis and mechanical degradation, The Journal of Physical Chemistry 92(13) (**1988**) 3705–3707. `doi:10.1021/j100324a005`.

[104] J. Rooze, R. Groote, R. T. M. Jakobs, R. P. Sijbesma, M. M. van Iersel, E. V. Rebrov, J. C. Schouten, J. T. F. Keurentjes, Mechanism of ultrasound scission of a silver-carbene coordination polymer, The Journal of Physical Chemistry B 115(38) (**2011**) 11038–11043. `doi:10.1021/jp203780a`.

[105] P. Kruus, M. O'Neill, D. Robertson, Ultrasonic initiation of polymerization, Ultrasonics 28(5) (**1990**) 304–309. `doi:10.1016/0041-624X(90)90036-N`.

[106] D. Krefting, R. Mettin, W. Lauterborn, High-speed observation of acoustic cavitation erosion in multibubble systems, Ultrasonics Sonochemistry 11(3–4) (**2004**) 119–123. `doi:10.1016/j.ultsonch.2004.01.006`.

[107] S. A. Elder, Cavitation microstreaming, The Journal of the Acoustical Society of America 31(1) (**1959**) 54–64. `doi:10.1121/1.1907611`.

[108] G. W. Ferrell, L. A. Crum, A novel cavitation probe design and some preliminary measurements of its application to megasonic cleaning, The Journal of the Acoustical Society of America 112(3) (**2002**) 1196–1201. `doi:10.1121/1.1498856`.

[109] M. Hauptmann, S. Brems, E. Camerotto, A. Zijlstra, G. Doumen, T. Bearda, P. Mertens, W. Lauriks, Influence of gasification on the performance of a 1 MHz nozzle system in megasonic cleaning, Microelectronic Engineering 87(5–8) (**2010**) 1512–1515. `doi:10.1016/j.mee.2009.11.061`.

[110] B. E. Noltingk, E. A. Neppiras, Cavitation produced by ultrasonics, Proceedings of the Physical Society. Section B 63(9) (**1950**) 674–685. `doi:10.1088/0370-1301/63/9/305`.

[111] K. S. Suslick, J. J. Gawienowski, P. F. Schubert, H. H. Wang, Alkane sonochemistry, The Journal of Physical Chemistry 87(13) (**1983**) 2299–2301. `doi:10.1021/j100236a013`.

[112] B. P. Barber, R. A. Hiller, R. Löfstedt, S. J. Putterman, K. R. Weninger, Defining the unknowns of sonoluminescence, Physics Reports 281(2) (**1997**) 65–143. `doi:10.1016/S0370-1573(96)00050-6`.

[113] A. Prosperetti, Thermal effects and damping mechanisms in the forced radial oscillations of gas bubbles in liquids, The Journal of the Acoustical Society of America 61(1) (**1977**) 17–27. `doi:10.1121/1.381252`.

[114] H. S. Carslaw, J. C. Jaeger, Conduction of Heat in Solids, 2nd Edition, Oxford University Press, Oxford, 1959.

[115] K. Yasui, Alternative model of single-bubble sonoluminescence, Physical Review E: Statistical, Nonlinear, and Soft Matter Physics 56(6) (**1997**) 6750–6760. `doi:10.1103/PhysRevE.56.6750`.

[116] D. R. Lide, W. M. Haynes, Handbook of chemistry and physics, Vol. 90, CRC Press, Boca Raton, 2009.

[117] E. Neppiras, Acoustic cavitation series: part one: Acoustic cavitation: an introduction, Ultrasonics 22(1) (**1984**) 25–28. `doi:10.1016/0041-624X(84)90057-X`.

[118] M. M. van Iersel, J. Cornel, N. E. Benes, J. T. F. Keurentjes, Inhibition of nonlinear acoustic cavitation dynamics in liquid CO_2, The Journal of Chemical Physics 126(6) (**2007**) 064508. `doi:10.1063/1.2434962`.

[119] B. D. Storey, A. J. Szeri, Mixture segregation within sonoluminescence bubbles, Journal of Fluid Mechanics 396 (**1999**) 203–221.

[120] K. Yasui, Single-bubble sonoluminescence from noble gases, Physical Review E: Statistical, Nonlinear, and Soft Matter Physics 63(3) (**2001**) 035301. `doi:10.1103/PhysRevE.63.035301`.

[121] K. Yasui, Segregation of vapor and gas in a sonoluminescing bubble, Ultrasonics 40(1–8) (**2002**) 643–647. `doi:10.1016/S0041-624X(02)00190-7`.

[122] J. Dewulf, H. van Langenhove, A. de Visscher, S. Sabbe, Ultrasonic degradation of trichloroethylene and chlorobenzene at micromolar concentrations: kinetics and modelling, Ultrasonics Sonochemistry 8(2) (**2001**) 143–150. `doi:10.1016/S1350-4177(00)00031-6`.

[123] I. Hua, R. H. Höchemer, M. R. Hoffmann, Sonochemical degradation of p-nitrophenol in a parallel-plate near-field acoustical processor, Environmental Science & Technology 29(11) (**1995**) 2790–2796. `doi:10.1021/es00011a014`.

[124] M. A. Beckett, I. Hua, Elucidation of the 1,4-dioxane decomposition pathway at discrete ultrasonic frequencies, Environmental Science and Technology 34(18) (**2000**) 3944–3953. `doi:10.1021/es000928r`.

[125] A. Henglein, Chemical effects of continuous and pulsed ultrasound in aqueous solutions, Ultrasonics Sonochemistry 2(2) (**1995**) S115–S121. `doi:10.1016/1350-4177(95)00022-X`.

[126] J. D. Schramm, I. Hua, Ultrasonic irradiation of dichlorvos: Decomposition mechanism, Water Research 35(3) (**2001**) 665–674. `doi:10.1016/S0043-1354(00)00304-3`.

[127] S. D. Lubetkin, Why is it much easier to nucleate gas bubbles than theory predicts?, Langmuir 19(7) (**2003**) 2575–2587. `doi:10.1021/la0266381`.

[128] H.-Y. Kwak, S.-D. Oh, Gas-vapor bubble nucleation – a unified approach, Journal of Colloid and Interface Science 278(2) (**2004**) 436–446. `doi:10.1016/j.jcis.2004.06.020`.

[129] Y. Mori, K. Hijikata, T. Nagatani, Effect of dissolved gas on bubble nucleation, International Journal of Heat and Mass Transfer 19(10) (**1976**) 1153–1159. `doi:10.1016/0017-9310(76)90149-6`.

[130] R. E. Apfel, The role of impurities in cavitation-threshold determination, The Journal of the Acoustical Society of America 48(5B) (**1970**) 1179–1186. `doi:10.1121/1.1912258`.

[131] P. Jarman, Measurements of sonoluminescence from pure liquids and some aqueous solutions, Proceedings of the Physical Society 73(4) (**1959**) 628–640.

[132] K. Nozaki, S.-I. Hatanaka, S. Hayashi, Dynamics of single sonoluminecsing bubble in concentrated aqueous alkaline halide solutions, Japanese Journal of Applied Physics 43(9A) (**2004**) 6481–6483. `doi:10.1143/JJAP.43.6481`.

[133] J. P. Dear, J. E. Field, A study of the collapse of arrays of cavities, Journal of Fluid Mechanics 190 (**1988**) 409–425. `doi:10.1017/S0022112088001387`.

[134] N. Bremond, M. Arora, C.-D. Ohl, D. Lohse, Controlled multibubble surface cavitation, Physical Review Letters 96(22) (**2006**) 224501. `doi:10.1103/PhysRevLett.96.224501`.

[135] M. M. van Iersel, N. E. Benes, J. T. F. Keurentjes, Importance of acoustic shielding in sonochemistry, Ultrasonics Sonochemistry 15(4) (**2008**) 294–300. `doi:10.1016/j.ultsonch.2007.09.015`.

[136] M. Ashokkumar, The characterization of acoustic cavitation bubbles – an overview, Ultrasonics Sonochemistry 18(4) (**2011**) 864–872. `doi:10.1016/j.ultsonch.2010.11.016`.

[137] M. Ashokkumar, M. Hodnett, B. Zeqiri, F. Grieser, G. J. Price, Acoustic emission spectra from 515 kHz cavitation in aqueous solutions containing surface-active solutes, Journal of the Ameri-

can Chemical Society 129(8) (**2007**) 2250–2258. `doi:10.1021/ja067960r`.

[138] A. Brotchie, T. Statham, M. Zhou, L. Dharmarathne, F. Grieser, M. Ashokkumar, Acoustic bubble sizes, coalescence, and sonochemical activity in aqueous electrolyte solutions saturated with different gases, Langmuir 26(15) (**2010**) 12690–12695. `doi:10.1021/la1017104`.

[139] G. Marrucci, L. Nicodemo, Coalescence of gas bubbles in aqueous solutions of inorganic electrolytes, Chemical Engineering Science 22(9) (**1967**) 1257–1265. `doi:10.1016/0009-2509(67)80190-8`.

[140] R. R. Lessard, S. A. Zieminski, Bubble coalescence and gas transfer in aqueous electrolytic solutions, Industrial & Engineering Chemistry Fundamentals 10(2) (**1971**) 260–269. `doi:10.1021/i160038a012`.

[141] N. F. Bunkin, O. A. Kiseleva, A. V. Lobeyev, T. G. Movchan, B. W. Ninham, O. I. Vinogradova, Effect of salts and dissolved gas on optical cavitation near hydrophobic and hydrophilic surfaces, Langmuir 13(11) (**1997**) 3024–3028. `doi:10.1021/la960265k`.

Effect of resonance frequency, power input, and saturation gas type on the oxidation efficiency of an ultrasound horn

3

The sonochemical oxidation efficiency (η_{ox}) of a commercial titanium alloy ultrasound horn has been measured using potassium iodide as a dosimeter at its main resonance frequency (20 kHz) and two higher resonance frequencies (41 and 62 kHz). Narrow power and frequency ranges have been chosen to minimise secondary effects such as changing bubble stability, and time available for radical diffusion from the bubble to the liquid. The oxidation efficiency is proportional to the frequency and to the power transmitted to the liquid (275 mL) in the applied power range (1–6 W) under argon. Luminol radical visualisation measurements show that the radical generation rate increases and a redistribution of radical producing zones is achieved at increasing frequency. Argon, helium, air, nitrogen, oxygen, and carbon dioxide have been used as saturation gases in potassium iodide oxidation experiments. The highest η_{ox} at 5 W has been observed under air at 62 kHz. The presence of carbon dioxide in air gives enhanced nucleation at 41 and 62 kHz and has a strong influence on η_{ox}. This is supported by the luminol images, the measured dependence of η_{ox} on input power, and bubble images recorded under carbon dioxide. The results give insight into the interplay between saturation gas and frequency, nucleation, and their effect on η_{ox}.

This Chapter has been published as: J. Rooze, E. V. Rebrov, J. C. Schouten, J. T. F. Keurentjes, Effect of resonance frequency, power input, and saturation gas type on the oxidation efficiency of an ultrasound horn, *Ultrasonics Sonochemistry* 18 **2011** 209–215.

3.1 Introduction

The effect of ultrasound frequency on the sonochemical oxidation efficiency has been a topic of interest in the past two decades[1–14]. The higher frequencies around 300 kHz are usually more efficient for radical formation in these studies due to an optimal bubble resonance size for bubble collapse and mass transport of radicals from the bubble[11–15]. The saturation gas type and composition play an important role in the frequency dependence. Air is the saturation gas with the highest oxidation efficiency in the work of Pétrier et al.[2] and Wayment and Casadonte[11]. Beckett and Hua measured sonoluminescence and radical production under argon-oxygen mixture atmospheres[12]. Mason et al.[5] measured terephthalic acid oxidation at 20, 40, and 60 kHz in an Undatim sonoreactor. The oxidation efficiency of the system not only depends on operating frequency and saturation gas, but also on reactor dimensions and shape[16,17], liquid depth[9,18], liquid viscosity, surface tension, liquid temperature[19], and power input[11,13].

This work focuses on the efficiency of potassium iodide oxidation using a commercial titanium alloy 20-kHz horn operated at 20 kHz and two higher order resonance frequencies, 41, and 62 kHz. A single ultrasound source has been used to make a comparison of the results easier than when using for example a horn at 20 kHz and a piezoelectric element at higher frequencies. A custom-made power supply has been used to operate the horn. Several saturation gases have been used in the experiments (argon, helium, air, nitrogen, oxygen, and carbon dioxide). A narrow power range (1–6 W) and frequency range (20, 41, and 62 kHz) have been chosen to minimise the influence of secondary effects on radical production due to changing bubble dynamics, different time scales, and changing bubble stability. The spatial distribution of radical producing zones has been visualised using luminol imaging.

3.2 Experimental

3.2.1 Ultrasound horn

A 20-kHz full wave Sonics and Materials ultrasound horn (part 630-0220) with replaceable tip was driven by a custom-made square wave charge driven amplifier[20] and an Agilent 33220A waveform generator. A Delta Elektronika ES 0300-0.45 was used to supply the power to the amplifier. The power delivered to the liquid was manually controlled by adjusting the frequency and voltage. It was below the minimum power that can be delivered using the Sonics and Materials generator belonging to this horn for this system at all times.

The impedance of the horn was measured in air at 20 °C using a Hioki 3532-50 impedance analyzer. The smallest obtainable resolution of 10 Hz was used. Many distinct impedance

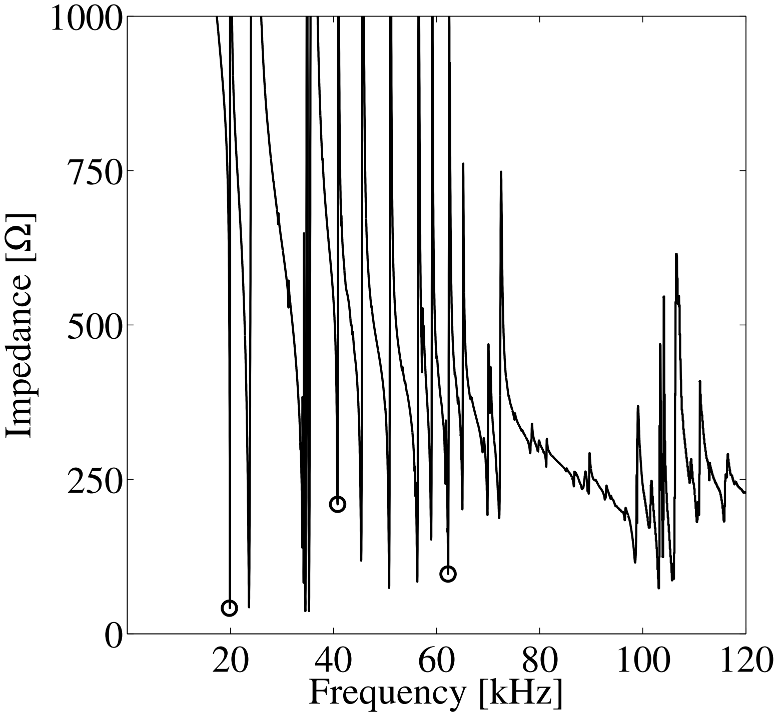

Figure 3.1: Impedance spectrum of a Sonics and Materials 20 kHz full wave horn for the frequency range of 10-120 kHz. The chosen resonance frequencies are indicated by circles.

minima, which represent resonance frequencies of the system, were found in the range of 10–120 kHz in the impedance spectrum of the horn (see Figure 3.1). Minima were observed at 20 kHz, the designed longitudinal resonance frequency of the horn, and at the flexural resonances 23 and 35 kHz. Less pronounced impedance minima were found at 41 and 62 kHz, the expected higher order vibrations of the 20 kHz longitudinal vibration.

3.2.2 Calorimetry

Calorimetry experiments were conducted in a cylindrical, double-jacketed glass reactor (internal diameter 6.5 cm and height 9 cm). The ultrasound power input into the liquid (275 mL) was determined over a period of 3 minutes in the reactor without coolant and with foam insulation. The transducer electrical to ultrasonic efficiency, $\eta_{\mathrm{E-U}}$, was calculated from the temperature change using a heat balance (see Table 3.1). Corrections were made for heat losses to the surroundings. At 20 and 62 kHz $\eta_{\mathrm{E-U}}$ was constant using driving voltages in the range from 100–500 V_{pp}. The horn used in this work has a slightly lower $\eta_{\mathrm{E-U}}$ at 20 kHz than that of 0.63, reported previously for a Sonics and Materials horn at a liquid depth of 8 cm[21], due to the square wave signal output of the amplifier. Power values in this paper are the ultrasonic input power into the liquid ($J_{\mathrm{ultrasonic}}$), unless mentioned otherwise.

Table 3.1: Electric to ultrasonic energy transfer efficiency with a 95% confidence interval of a commercial titanium alloy 20-kHz horn driven by a square voltage signal at resonance frequency.

Frequency (kHz)	$\eta_{\mathrm{E-U}}$ ($J_{\mathrm{ultrasonic}}\ J^{-1}_{\mathrm{electric}}$)
20	0.46 ± 0.03
41	0.17 ± 0.01
62	0.21 ± 0.02

3.2.3 Potassium iodide oxidation

An aqueous potassium iodide (Merck, p.a.) solution (275 mL, 0.1 mol L^{-1}) was sonicated in the glass reactor. A trade-off has been made in the vessel selection between larger vessels with a low signal-to-noise ratio at the same irradiation time, and smaller vessels with a larger wall influence on the ultrasonic field. The temperature was maintained at 20.0 ± 0.2 °C using a Lauda E300 thermostat. A gas flow was fed through the solution using a steel sparger for at least 30 minutes prior to, and during all experiments. Samples (1.0 mL) were taken and analyzed using a Shimadzu 2501-PC UV spectrometer operated at 350 nm. The I_3^- concentrations were calculated using a spectroscopic extinction coefficient of 26.4×10^3

L mol^{-1} cm^{-1} [22]. The amount of I_3^- produced was divided by the ultrasonic input power to obtain the oxidation efficiency, η_{ox}. At 41 kHz $\eta_{\mathrm{E-U}}$ is shifted during experiments due to heat production in the horn, therefore potassium iodide oxidation experiments at this frequency were shorter (12 minutes maximum) than experiments at other frequencies (30 minutes).

3.2.4 Luminol and bubble mapping

An aqueous solution (250 mL) of 0.05 mol L^{-1} luminol (Merck, p.a.) and 0.1 mol L^{-1} Na_2CO_3 (Merck, p.a.) was sonicated in an approximately cylindrical stainless steel reactor (6 cm internal diameter, 9 cm height) with two quartz windows, one at the bottom and one at the side. Luminol reacted with OH radicals, and light was emitted during this reaction[23]. Images were captured in a dark room using a Nikon D80 camera with an 18–55 mm lens at 35 mm focal distance. The exposure time was 3 minutes, the f-number was 5.0, and the ISO setting was Hi1, which is ISO 3200 equivalent, with the high ISO noise reduction setting turned on. Argon was bubbled into the solution for at least 30 minutes prior to initiating the reaction.

Bubble field images were captured using the same reactor and camera with the lens at a focal distance of 35 mm. Photographs were taken through the window at the side of the reactor. The ISO value was 400, exposure time was 0.2 s, the f-number was 7.0. Gas was bubbled through the solution prior to recordings. Light was introduced into the vessel through the quartz window in the reactor bottom to illuminate the bubble fields using a Dedocool CoolT3 250 W lamp.

3.3 Results and discussion

3.3.1 Effect of frequency

Sonochemiluminescence profiles have been obtained by luminol imaging using argon as a saturation gas (see Figure 3.2). A high radical formation rate is observed in a conical volume directly underneath the horn tip at 20 kHz. Large wave-like areas with light emission have been registered throughout the vessel. Apparently it is easier to obtain hydroxyl radicals in the solution at higher frequency. At lower power input, the pattern observed at 41 kHz reduces to a conical radical producing zone similar to that in Figure 3.2 (a) (not shown). The total normalised intensity of the images, obtained by dividing by the total intensity at 20 kHz, is 1 : 1.8 : 2.4 for 20, 41, and 62 kHz, respectively. The total normalised intensity is lower for images at smaller power input (not shown).

A characteristic feature of the measurement at 41 kHz and 4.8 W is the light emission around the horn shaft at 1 cm from the horn tip (the straight shaft of the horn is 5 cm long). This suggests that there is lateral sound emission from either a flexural wave, or from the radial extension and compression of the shaft originating from a longitudinal wave. Active radical producing bands at the top of the images are found near the liquid fill level. An interaction of the sound field with the stainless steel wall is observed, which was also found for a 100 kHz sound field in a glass vessel[24].

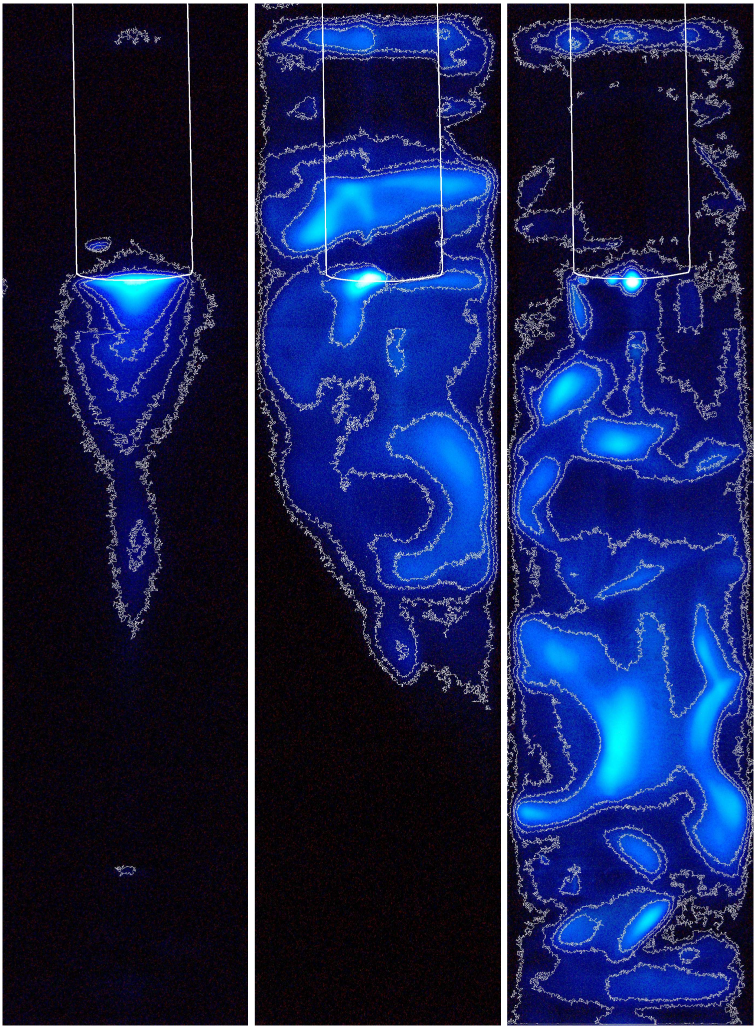

(a) 20 kHz (b) 41 kHz (c) 62 kHz

Figure 3.2: Luminol light emission images recorded of a horn vibrating at resonance frequencies of (a) 20, (b) 41, and (c) 62 kHz at 4.9±0.1 W power input, in an aqueous luminol solution saturated with argon. The probe outline (diameter 1.27 cm) and intensity contours (20, 40, 60, and 80%, blue channel) are marked with white lines.

3.3.2 Effect of input power

The oxidation efficiency, η_{ox}, as a function of input power under argon is shown in Figure 3.3. It is proportional to the input power in the liquid for all resonance frequencies measured; the system becomes more efficient at higher power inputs. This is consistent with results obtained by other researchers at power input below 10 W[11,13]. At higher power input (10–100 W, depending on the frequency used) the efficiency is expected to level off or to have a maximum[25,26]. With the amplifier used in this work, higher power outputs could not be reached, and no plateau or maximum has been observed. Large deviations from the mean value are observed at 41 kHz in Figure 3.3 due to heating of the probe, which is discussed in 3.2.2.

The increasing efficiency per Joule at increasing power input can be explained with the non-uniformity of the sound field combined with a power threshold. An energy threshold for radical production is exceeded in the active zones (see Figure 3.2), while the energy transferred to the non-active zones is immediately lost since it is not used for cavitation events. The total active volume increases at a higher rate than the input power with increasing input power, resulting in a higher η_{ox}.

The η_{ox} of the horn, designed for operation at 20 kHz, increases at 41 and 62 kHz, even when using the electrical power input instead of the ultrasonic power input in efficiency calculations.

3.3.3 Effect of frequency and gas saturation type

The η_{ox} of potassium iodide has been measured at a power level of 5 W under several saturation gases: argon, helium, air, nitrogen, oxygen, and carbon dioxide (Figure 3.4). η_{ox} increases with increasing operating frequency for all saturation gases, except for carbon dioxide. Under carbon dioxide there is no measurable radical production at any of the operating frequencies. The oxidation efficiencies under air, oxygen and argon show the most pronounced trends at the three frequencies. At 20 kHz η_{ox} is higher under argon than under air or oxygen (0.6×10^{-10} mol J^{-1}, 0.0×10^{-10} mol J^{-1}, and 0.5×10^{-10} mol J^{-1}, respectively). At 62 kHz the highest η_{ox} has been observed under air (4.4×10^{-10} mol J^{-1}), followed by η_{ox} under oxygen (2.2×10^{-10} mol J^{-1}), and under argon (1.7×10^{-10} mol J^{-1}).

Images captured of the bubble fields under air and carbon dioxide using a light source demonstrate that the nucleation of bubbles seems to be important for the process (Figure 3.5). Hardly any bubbles are visible in the air-saturated solution. The active cavitation bubbles are too small and short-lived for the camera to capture. The same holds when saturating the solution with argon, helium, oxygen and nitrogen. Many big, stable bubbles are visible in the solution under the horn when using carbon dioxide on the other hand. The bubbles grow

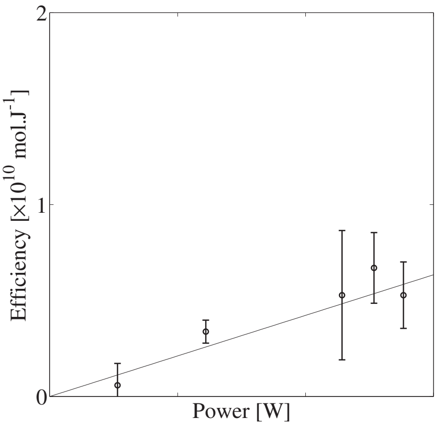

(a) 20 kHz

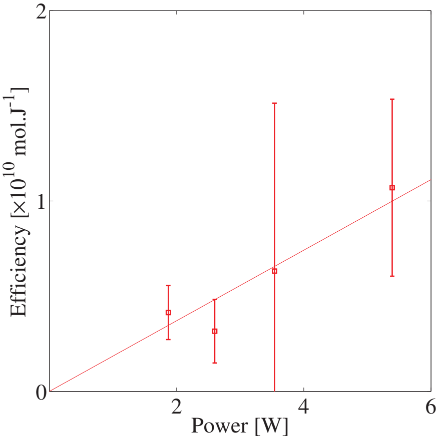

(b) 41 kHz

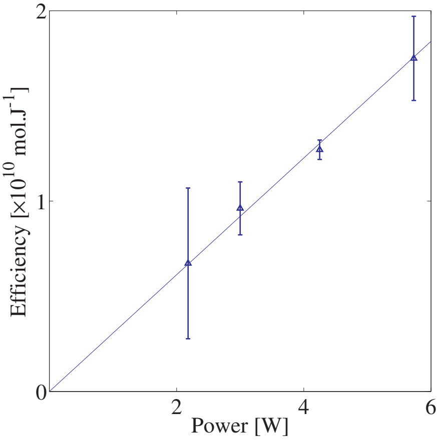

(c) 62 kHz

Figure 3.3: Potassium iodide oxidation efficiency at (a) 20, (b) 41, and (c) 62 kHz in a 275 mL reactor using 1–6 W input power and argon as the saturation gas. The error bars indicate 95% confidence intervals.

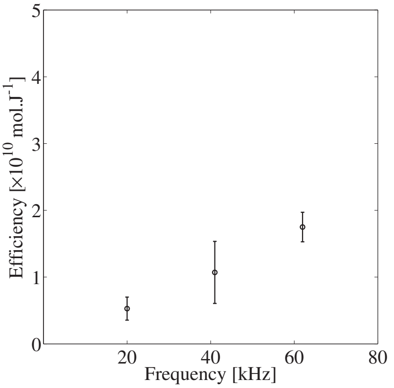

(a) argon (b) air

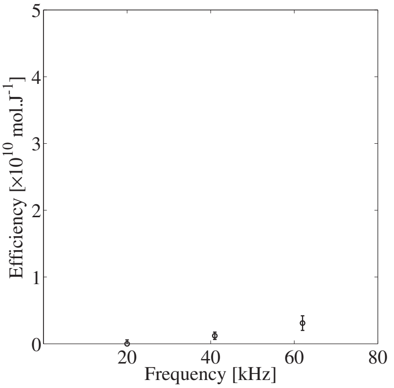

(c) helium (d) nitrogen

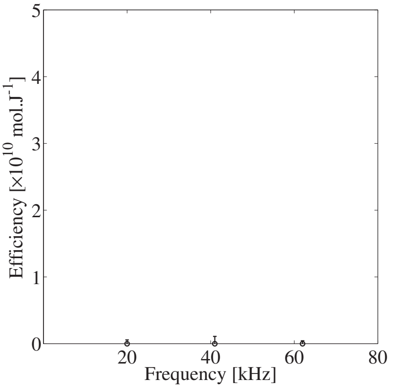

(e) carbon dioxide (f) oxygen

Figure 3.4: Potassium iodide oxidation efficiency at 20, 41, and 62 kHz in a 275 mL reactor using 5 W input power and several saturation gases. The error bars indicate 95% confidence intervals.

bigger since carbon dioxide has a high solubility in water (see Table 3.2), which makes more nuclei available for cavitation, and it makes bubble growth easier. The higher oxidation efficiencies at 41 and 62 kHz under air appear to originate from the presence of CO_2. A CO_2 concentration of 370 ppm in air is sufficient to accelerate bubble nucleation and growth, resulting in a higher number of active bubbles and a higher oxidation rate.

Table 3.2: Gas solubility in water and heat capacity of several gases at 20 °C[27].

Gas	Solubility ($mol\ mol^{-1}$)	Heat capacity ($J\ mol^{-1}\ K^{-1}$)
Helium	7.0×10^{-6}	20.9
Argon	2.7×10^{-5}	20.8
Nitrogen	1.5×10^{-5}	29.2
Oxygen	2.5×10^{-5}	29.4
Carbon dioxide	7.1×10^{-4}	37.5

A similar relation between frequency, η_{ox}, and the saturation gases argon and air was found by Pétrier et al. at 514 kHz and 20 W and 20 kHz and 30 W[2] and Wayment and Casadonte at 300 and 20 kHz at 0.8 W[11]. The experiments at 20 kHz were more efficient under argon, and the experiments at higher frequencies under air. Iida et al. found that argon gave higher conversions in Fricke dosimetry at 130 kHz and 100 W[28]. Beckett and Hua found an optimal argon to oxygen ratio of 3:1 for the decomposition of 1,4-dioxane at 358 kHz and 128 W[12]. Pétrier et al. suggested that the different time scales (514 and 20 kHz) at which the collapse and diffusion of radicals around a bubble occurred were dominant in the changing behavior. The hydrogen and hydroxyl radicals had more time to recombine to form water inside the bubble at 20 kHz.

The collapse time scale is expected to have much less influence for the narrow frequency range used in this work. However, a frequency dependence has been observed for η_{ox}. It is unlikely that the lower hot spot temperature is the only determining factor in the experiments performed. Iodide oxidation has been measured under oxygen (0.5×10^{-10} mol J^{-1}) but not under air at 20 kHz, and the hot spot temperature is expected to be similar under oxygen as under air, due to similar heat capacities of these gases (see Table 3.2). The carbon dioxide in air can increase both bubble size on collapse and bubble shielding and interference (see Figure 3.5). This can lower the number of regular collapses, especially in the focussed cavitation zone created by the horn at 20 kHz, and thereby lower the radical production.

Oxygen addition to the mixture may increase the average radical lifetime since oxygen radicals are more stable than the hydrogen and hydroxyl radicals that are produced under an argon atmosphere. The more stable radicals diffuse out of the bubble in larger quantities,

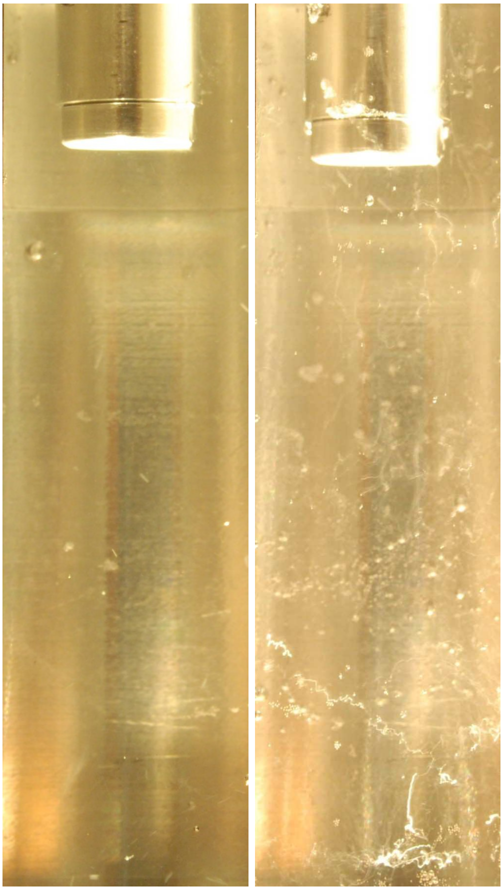

(a) air (b) carbon dioxide

Figure 3.5: Bubble field images at 62 kHz and 5 W using (a) air and (b) carbon dioxide as a saturation gas.

resulting in a higher η_{ox}. The low radical production under a helium atmosphere was observed before[25,29,30], and was due to either the high heat conductivity of helium[29,30] or a high water vapour content in the bubble. The latter was due to a high water diffusion coefficient in the helium-rich bubble[31].

3.4 Conclusions

The oxidation efficiency of a commercial titanium alloy 20-kHz horn was investigated at the resonance frequencies 20, 41, and 62 kHz, and at a power input of 1–6 W using potassium iodide oxidation as a dosimeter. The radical formation rate was proportional to input power under argon, and proportional to frequency under several saturation gases. Potassium iodide oxidation at 20 kHz was most efficient under argon, and at 41 and 62 kHz under air. Luminol visualisation experiments under argon showed a conical radical producing region directly underneath the tip at 20 kHz under argon. Radical producing zones of increasing size were observed in the reactor at 41 and 62 kHz. The results indicate that the nucleation of radical producing bubbles is an important factor in the overall process.

Bibliography

[1] G. Cum, G. Galli, R. Gallo, A. Spadaro, Role of frequency in the ultrasonic activation of chemical reactions, Ultrasonics 30(4) (**1992**) 267–270. `doi:10.1016/0041-624X(92)90086-2`.

[2] C. Pétrier, A. Jeunet, J.-L. Luche, G. Reverdy, Unexpected frequency effects on the rate of oxidative processes induced by ultrasound, Journal of the American Chemical Society 114 (**1992**) 3148–3150. `doi:10.1021/ja00034a077`.

[3] Y. T. Didenko, D. N. Nastich, S. P. Pugach, Y. A. Polovinka, V. I. Kvochka, The effect of bulk solution temperature on the intensity and spectra of water sonoluminescence, Ultrasonics 32(1) (**1994**) 71–76. `doi:10.1016/0041-624X(94)90083-3`.

[4] M. H. Entezari, P. Kruus, Effect of frequency on sonochemical reactions. I: Oxidation of iodide, Ultrasonics Sonochemistry 1(2) (**1994**) S75–S79. `doi:10.1016/1350-4177(94)90001-9`.

[5] T. Mason, J. Lorimer, D. Bates, Y. Zhao, Dosimetry in sonochemistry: the use of aqueous terephthalate ion as a fluorescence monitor, Ultrasonics Sonochemistry 1(2) (**1994**) S91–S95. `doi:10.1016/1350-4177(94)90004-3`.

[6] C. Pétrier, M.-F. Lamy, A. Francony, A. Benahcene, B. David, V. Renaudin, N. Gondrexon, Sonochemical degradation of phenol in dilute aqueous solutions: Comparison of the reaction rates at 20 and 487 kHz, The Journal of Physical Chemistry 41(98) (**1994**) 10514–10520. `doi:10.1021/j100092a021`.

[7] A. Francony, C. Pétrier, Sonochemical degradation of carbon tetrachloride in aqueous solution at two frequencies: 20 kHz and 500 kHz, Ultrasonics Sonochemistry 3(2) (**1996**) S77–S82. `doi:10.1016/1350-1477(96)00010-1`.

[8] S. Fındık, G. Gündüz, E. Gündüz, Direct sonication of acetic acid in aqueous solutions, Ultrasonics Sonochemistry 13(3) (**2006**) 203–207. `doi:10.1016/j.ultsonch.2005.11.005`.

[9] Y. Asakura, T. Nishida, T. Matsuoka, S. Koda, Effects of ultrasonic frequency and liquid height on sonochemical efficiency of large-scale sonochemical reactors, Ultrasonics Sonochemistry 15(3) (**2008**) 244–250. `doi:10.1016/j.ultsonch.2007.03.012`.

[10] B. Ondruschka, J. Lifka, J. Hofmann, Aquasonolysis of ether - effect of frequency and acoustic power of ultrasound, Chemical Engineering & Technology 23(7) (**2000**) 588–592. `doi:10.1002/1521-4125(200007)23:7<588::AID-CEAT588>3.0.CO;2-Y`.

[11] D. G. Wayment, D. J. Casadonte Jr., Design and calibration of a single-transducer variable-frequency sonication system, Ultrasonics Sonochemistry 9(4) (**2002**) 189–195. `doi:10.1016/S1350-4177(01)00127-4`.

[12] M. A. Beckett, I. Hua, Impact of ultrasonic frequency on aqueous sonoluminescence and sonochemistry, The Journal of Physical Chemistry 105 (**2001**) 3796–3802. `doi:10.1021/jp003226x`.

[13] P. Kanthale, M. Ashokkumar, F. Grieser, Sonoluminescence, sonochemistry (H_2O_2 yield) and bubble dynamics: Frequency and power effects, Ultrasonics Sonochemistry 15(2) (**2008**) 143–150. `doi:10.1016/j.ultsonch.2007.03.003`.

[14] S. Koda, T. Kimura, T. Kondo, H. Mitome, A standard method to calibrate sonochemical efficiency of an individual reaction system, Ultrasonics Sonochemistry 10(3) (**2003**) 149–156. `doi:10.1016/S1350-4177(03)00084-1`.

[15] J. D. Seymour, H. C. Wallace, R. B. Gupta, Sonochemical reactions at 640 kHz using an efficient reactor. Oxidation of potassium iodide, Ultrasonics Sonochemistry 4(4) (**1997**) 289–293. `doi:10.1016/S1350-4177(97)00039-4`.

[16] S. de la Rochebrochard d'Auzay, J.-F. Blais, E. Naffrechoux, Comparison of characterization methods in high frequency sonochemical reactors of differing configurations, Ultrasonics Sonochemistry 17(3) (**2010**) 547–554. `doi:10.1016/j.ultsonch.2009.10.024`.

[17] Y. Kojima, Y. Asakura, G. Sugiyama, S. Koda, The effects of acoustic flow and mechanical flow on the sonochemical efficiency in a rectangular sonochemical reactor, Ultrasonics Sonochemistry 6 (**2009**) 978–984. `doi:10.1016/j.ultsonch.2009.11.020`.

[18] A. Henglein, Sonochemistry: Historical developments and modern aspects, Ultrasonics 25(1) (**1987**) 6–16. `doi:10.1016/0041-624X(87)90003-5`.

[19] M. P. Brenner, S. Hilgenfeldt, D. Lohse, Single-bubble sonoluminescence, Reviews of Modern Physics 74(2) (**2002**) 425–484. `doi:10.1103/RevModPhys.74.425`.

[20] J.-W. Waanders, Piezoelectric Ceramics, Properties & Applications, Philips Components, Eindhoven, 1991.

[21] R. F. Contamine, A. M. Wilhelm, J. Berlan, H. Delmas, Power measurement in sonochemistry, Ultrasonics Sonochemistry 2(1) (**1995**) S43–S47. `doi:10.1016/1350-4177(94)00010-P`.

[22] D. A. Palmer, R. W. Ramette, R. E. Mesmer, Triiodide ion formation equilibrium and activity coefficients in aqueous solution, Journal of Solution Chemistry 13(9) (**1984**) 673–683. `doi:10.1007/BF00650374`.

[23] T. Tuziuti, K. Yasui, M. Sivakumar, Y. Iida, Influence of dissolved-air concentration on spatial distribution of bubbles for sonochemistry, Ultrasonics 44 (**2006**) e357–e361. `doi:10.1016/j.ultras.2006.05.002`.

[24] K. Yasui, T. Kozuka, T. Tuziuti, A. Towata, Y. Iida, J. King, P. Macey, FEM calculation of an acoustic field in a sonochemical reactor, Ultrasonics Sonochemistry 14(5) (**2007**) 605–614. `doi:10.1016/j.ultsonch.2006.09.010`.

[25] G. Mark, A. Tauber, R. Laupert, H.-P. Schuchmann, D. Schulz, A. Mues, C. von Sonntag, OH-radical formation by ultrasound in aqueous solution – part II: Terephthalate and Fricke dosimetry and the influence of various conditions on the sonolytic yield, Ultrasonics Sonochemistry 5(2) (**1998**) 41–52. `doi:10.1016/S1350-4177(98)00012-1`.

[26] M. Gutiérrez, A. Henglein, Chemical action of pulsed ultrasound: observation of an unprecedented intensity effect., The Journal of Physical Chemistry 94(9) (**1990**) 3625–3628. `doi:`

`10.1021/j100372a048`.

[27] D. R. Lide, W. M. Haynes, Handbook of chemistry and physics, Vol. 90, CRC Press, Boca Raton, 2009.

[28] Y. Iida, K. Yasui, T. Tuziuti, M. Sivakumar, Sonochemistry and its dosimetry, Microchemical Journal 80(2) (**2005**) 159–164. `doi:10.1016/j.microc.2004.07.016`.

[29] W. B. McNamara III, Y. T. Didenko, K. S. Suslick, Sonoluminescence temperatures during multi-bubble cavitation, Nature 401(6755) (**1999**) 772–775. `doi:10.1038/44536`.

[30] F. R. Young, Sonoluminescence from water containing dissolved gases, The Journal of the Acoustical Society of America 60(1) (**1976**) 100–104. `doi:10.1121/1.381076`.

[31] B. D. Storey, A. J. Szeri, A reduced model of cavitation physics for use in sonochemistry, Proceedings: Mathematical, Physical and Engineering Sciences 457(2011) (**2001**) 1685–1700. `doi:10.1098/rspa.2001.0784`.

Enhanced ultrasonic radical production in water saturated with argon-oxygen-carbon dioxide gas mixtures

4

The mechanism behind the high radical production of air-bubbled solutions in sonochemical experiments with potassium iodide is investigated. Air-bubbled solutions can give a higher radical production than than argon-bubbled solutions even though argon has a higher adiabatic index than air. Various gases in different compositions have been used to saturate the liquid, most importantly argon, oxygen, and carbon dioxide. Argon has a high adiabatic index which gives a high collapse temperature, oxygen takes part in chemical reactions, and acidification by carbon dioxide or citric acid prevents a back reaction. These mechanisms enhance the radical production, and by tuning the gases an optimum radical production can be obtained.

This Chapter is in preparation to be submitted as: J. Rooze, E. V. Rebrov, J. C. Schouten, J. T. F. Keurentjes, Enhanced ultrasonic radical production in water saturated with argon-oxygen-carbon dioxide gas mixtures.

4.1 Introduction

The chemical effect induced by ultrasonic cavitation processes is strongly influenced by the type of gas in the liquid. It determines the thermal properties of the cavitation bubble, such as the adiabatic index $\gamma = C_p/C_v$, where C_p is the heat capacity at constant pressure, and C_v is the heat capacity at constant volume, and the thermal conductivity. These are important parameters that determine the hot spot temperature[1]. The gas can also participate in chemical reactions during bubble collapse. Collapsing bubbles can emit light, a process called sonoluminescence[1]. The gas content of sonoluminescing bubbles is important for the intensity of the luminescence, where bubbles containing noble gases give the highest intensity in single bubble sonoluminescence[2,3] and multi bubble sonoluminescence[4–6]. It is also important for the stability of the bubble[7]. The effect of gas on the radical production rate[8–18], and on the breakdown rate of organic molecules[19–30] has been reported in literature before. A higher efficiency, usually expressed in number of converted mol per unit energy input, is often found when air is used as a saturation gas during cavitation at frequencies above 20 kHz[15–25]. This is remarkable because experiments under air are expected to give a lower hot spot temperature and therefore a lower reactivity as compared to those under argon due to the higher adiabatic ratio of air as compared to that of argon. The highest radical yield in aqueous systems saturated with binary gas mixtures was observed under saturation with argon-oxygen mixtures, where an optimum oxygen concentration for radical production was reported to be between 20 and 42 vol%[30–32]. The highest hydrogen peroxide production in a 40 vol% methanol aqueous solution has been measured under pure oxygen rather than under pure argon or mixtures thereof[33]. The highest rate constant in a UV-enhanced sonophotocatalytic degradation of 2-chlorophenol over a titania catalyst was obtained at an oxygen concentration 50 – 100 vol% in an argon-oxygen mixture[34]. The highest rate of inactivation of Escherichia Coli was reported to be at 30 vol% oxygen concentration in an argon-oxygen mixture[35]. The likely inactivation mechanism was by free-radical attack.

This study is aimed to investigate the higher efficiency of air as a saturation gas in sonochemical radical chemistry experiments. This effect can be explained by looking at the physical and chemical effects of the different gases separately. The effect of saturation gas, present mainly as gas bubbles in the liquid, has been measured by potassium iodide oxidation at a relatively low power input of 2.9 W and a frequency of 62 kHz. Water saturated with binary or ternary gas mixtures of nitrogen, oxygen, argon, and carbon dioxide has been used. Subsequently, the increased radical formation upon the addition of citric acid has been investigated, since the acidifying effect of carbon dioxide can not be decoupled from its impact on the hot spot temperature. These experiments further explore results obtained in previous work where radical production in air saturated solutions was higher than that in argon saturated solutions[18].

4.2 Experimental

A Sonics and Materials 20-kHz ultrasound horn was driven at the frequency of 62.0 ± 0.2 kHz at constant input power input using an Agilent 33220A waveform generator, a Delta Elektronika ES 0300-0.45 power supply, and a custom built amplifier[36], similar to previous work[18]. The peak-to-peak voltage and current were kept constant at 120 V and 170 ± 10 mA, corresponding to an input power into the liquid of 2.9 ± 0.2 W, which was determined calorimetrically. The frequency was kept slightly above the resonance frequency to allow better control of the power input into the liquid. The power input did not depend on the saturation gas type. The coolant temperature was continuously monitored to observe deviations in the power input. The created cavitation field is relatively stable as compared to a conventional 20 kHz field since the power input is low and since a standing wave is created. The field consists of larger bubbles which exist in planes in the liquid, which have a relatively long estimated life time of several seconds, and eject smaller bubbles that move through the liquid, and

Argon (99.996 vol% purity, Linde), oxygen (99.995 vol%, Linde), nitrogen (99.999 vol% purity, Linde), carbon dioxide (99.995 vol% purity, Linde), and compressed air flows were controlled by Bronkhorst mass flow controllers (F-200CV). A total gas flow of 0.5×10^{-3} NL s^{-1} was bubbled through the solution using a steel sparger for at least 30 minutes prior to, and during all experiments.

A 250 mL 0.1 mol L^{-1} aqueous potassium iodide (Merck, >99.8 wt%) solution was sonicated in a double-jacketed glass reactor, with a 6 cm internal diameter, 10 cm height, and a 1 mm thick bottom plate. The temperature was maintained at 20 ±0.1°C using a Lauda E300 thermostat and a Pt-100 temperature sensor. The pH was systematically changed with citric acid (VWR Prolabo, Ph.Eur.) and it was measured before and after the experiment with a GC-840 pH meter (Schott). The triiodide concentration was measured in 1 mL samples using a Shimadzu 2501-PC UV spectrometer and using a spectroscopic extinction coefficient of 26.4×10^3 L mol^{-1} cm^{-1}[37].

4.3 Results and discussion

4.3.1 Effect of binary gas mixture composition on oxidation efficiency using argon, nitrogen and oxygen

The potassium iodide oxidation efficiency, also called the triiodide yield in this work, in oxygen-nitrogen saturated water is shown in Fig. 4.1. Similar yields of 2.0 and 2.6×10^{-10} mol J^{-1} are observed under nitrogen and oxygen, respectively. A slightly higher oxidation efficiency is observed in solutions saturated with oxygen-nitrogen mixtures as compared to those saturated with the pure gases. An efficiency of 9.5×10^{-10} mol J^{-1} is obtained using air as a saturation gas. A linear relation between the yield and the concentration of nitrogen in binary argon-nitrogen saturated water is observed (not shown).

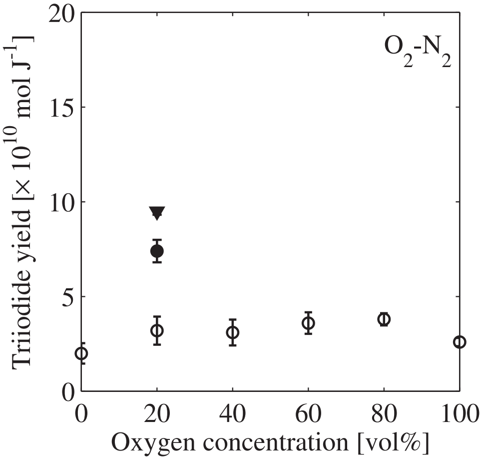

Figure 4.1: Potassium iodide oxidation efficiency in water saturated with various nitrogen-oxygen mixtures versus the oxygen concentration in the feed. The error bars are 95% confidence intervals. The closed triangle is the radical production when using air as a saturation gas, and the closed circle is the radical production of a 0.15 vol% carbon dioxide and 20 vol% oxygen in nitrogen.

A maximum oxidation efficiency of 14×10^{-10} mol J^{-1} is found at an oxygen concentration of 20 vol% in the argon-oxygen mixture (Fig. 4.2). This efficiency is 6.2 times higher as compared to that under pure argon (2.3×10^{-10} mol J^{-1}). The optimum oxygen composition is in good agreement with those previously reported[30–32]. Oxygen addition to the saturation gas mixture increases radical production because oxygen dissociates above 2500 K[38]. Oxygen scavenges hydrogen radicals to form either a hydroxyl or a hydroperoxyl radical which participates in further reactions. Two hydrogen radicals can form a hydrogen molecule which escapes, or a hydrogen radical can recombine with hydroxyl radicals and form a water molecule in the absence of oxygen. The highest oxidation efficiency is obtained in the argon-oxygen mixture due to the combined effect of the high adiabatic index of argon, which results in high hot spot temperatures, and additional chemical reaction pathways in the presence of oxygen. The two effects that operate at the same time result in a maximum in the radical production. A factor that can influence these results is the relatively long lifetime of some of the bubbles, in which the bubble contents can change[7].

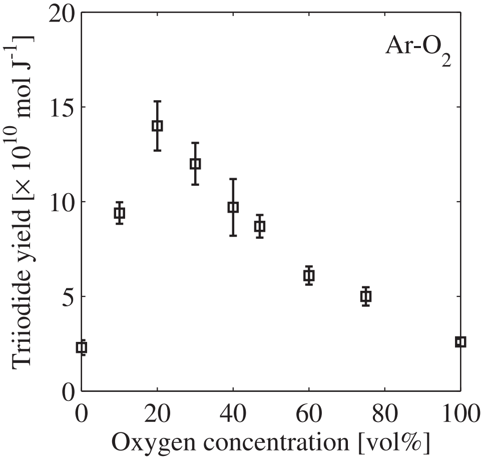

Figure 4.2: Potassium iodide oxidation efficiency in water saturated with an argon-oxygen mixture as a function of the oxygen concentration. The error bars are 95% confidence intervals. A maximum radical production is found at 20 vol% oxygen, 80 vol% argon.

4.3.2 Effect of carbon dioxide addition on oxidation efficiency

The oxidation efficiency increases under addition of small amounts of carbon dioxide to water saturated with either argon (see Fig. 4.3) or the 20 vol% oxygen-argon mixture (see Fig. 4.4). A mixture of 0.15 vol% of carbon dioxide and 20 vol% oxygen in nitrogen closely resembles the composition of air. The triiodide oxidation efficiency in water saturated with this mixture increases from 3.2 to 7.4×10^{-10} mol J^{-1}, which is close to the value of 9.5×10^{-10} mol J^{-1} obtained in an air saturated mixture. The highest oxidation efficiency of 7.5×10^{-10} mol J^{-1} is observed between carbon dioxide concentrations from 0.3 to 1.5 vol% in solutions saturated with carbon dioxide-argon binary saturation gas mixtures. The carbon dioxide addition to the binary 20 vol% oxygen-argon mixture increases the triiodide oxidation efficiency (see Fig. 4.4). The highest oxidation efficiency in the ternary mixture is observed at a carbon dioxide concentration of 0.15 vol%, which is lower than that in the carbon dioxide-argon binary saturation gas mixture. The triiodide oxidation efficiency decreases both in the binary and ternary mixtures as the carbon dioxide concentration increases above the optimum value.

This is due to a lower adiabatic index resulting in lower hot spot temperature in the presence of larger amounts of carbon dioxide. The hot spot temperatures are much closer to the radical production threshold in water saturated with an argon-oxygen mixture as compared to those saturated with argon. The hot spot temperature decreases even further when carbon dioxide is added.

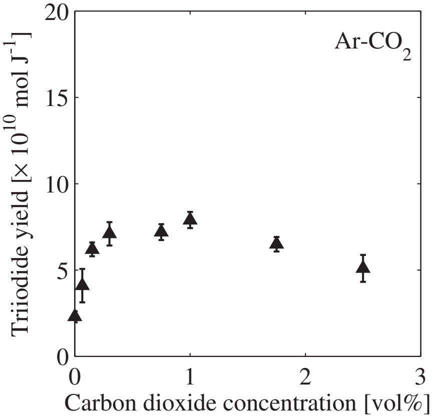

Figure 4.3: Potassium iodide oxidation efficiency in water saturated with the argon-carbon dioxide mixtures as a function of the carbon dioxide concentration. The error bars are 95% confidence intervals.

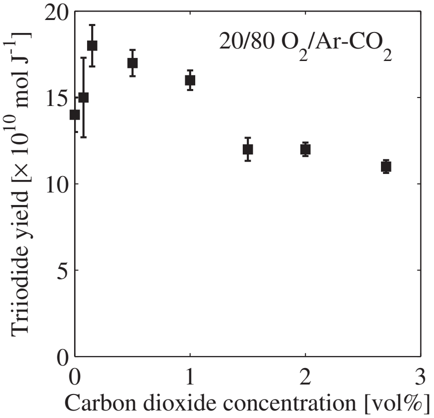

Figure 4.4: Potassium iodide oxidation efficiency in water saturated with 20 vol% oxygen in argon and carbon dioxide mixtures as a function of the carbon dioxide concentration. The error bars are 95% confidence intervals.

The triiodide production as a function of pH is shown in Figure 4.5. The highest production of 26×10^{-10} mol J^{-1} is found at a pH of 3. The pH shifts from 5.0 to 8.5 during experiments starting at a pH of 5. This shift is not observed at pH values of 3 and 4. The oxidation efficiency of 12×10^{-10} mol J^{-1} mol J^{-1} is constant at the pH in the range above 6.

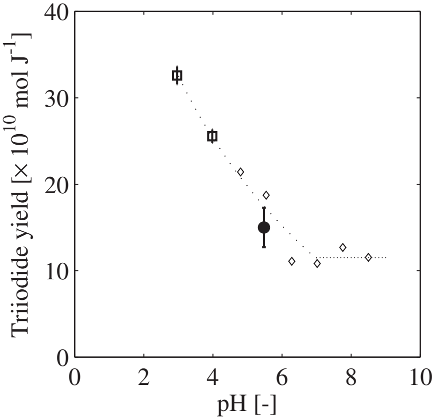

Figure 4.5: Potassium iodide oxidation efficiency in water saturated with 20 vol% oxygen in argon mixtures as a function of pH (circles). The error bars are 95% confidence intervals. The measurements in the range of pH from 5.0 to 8.5 are plotted at linearly interpolated pH values (diamonds, N=2). The dotted line is drawn as a guide to the eye. A similar radical production enhancement is measured when using carbon dioxide as an acidifier instead of citric acid. The filled circle at pH is 5.5 is the measurement with 20 vol% oxygen in argon and 750 ppm carbon dioxide. Carbon dioxide also quenches the cavitation hot spot temperature so measurements with higher carbon dioxide concentrations in the feed gas deviate more from the values measured in the solutions with corresponding pH created by citric acid addition.

Several mechanisms can be suggested that account for this behaviour. The hydronium cations can be consumed during the reaction by the direct oxidation of iodide with oxygen and hydronium (see Eq. 4.1)[8,39]. This direct route can create an apparent sonochemical oxidation rate which is higher than the actual reaction rate. High temperatures in the collapsing bubbles might be needed to accelerate this reaction to measurable values. This reaction does not explain the increased oxidation rate in absence of oxygen (See *e.g.* Fig. 4.3).

Drijvers *et al.*[40,41] find an increased reaction rate at increasing pH for ultrasonic degradation by pyrolysis of trichloroethylene (TCE). They ascribe this to a decreasing amount of carbon dioxide in the cavitating bubbles, since the carbon dioxide is in ionised form at high pH. The difference between these results and the results presented above is the reaction mechanism, TCE breakdown takes place inside the bubble where the carbon dioxide has a suppressing effect, whereas the iodine is oxidised in solution, where the carbon dioxide depresses the backward reaction. Jiang *et al.*[42] found an optimum pH for hydrogen peroxide formation, measured with potassium iodide, at pH = 3.2, and ascribe this to chemical interaction between radicals and the acid used in their work, phosphoric acid. At low pH less OH radicals are scavenged by the less ionized acid. The increased radical production upon acid addition described above is not explained by this mechanism.

Hydrogen peroxide reacts with triiodide to form iodide under neutral or alkaline conditions (see Eq. 4.2)[32]. Acidification of the solution by carbonic acid, formed by dissolution of carbon dioxide in water, or by citric acid therefore hinders this consumption reaction.

$$2H^+ + 2I^- + 0.5O_2 \rightarrow I_2 + H_2O \tag{4.1}$$

$$H_2O_2 + I_3^- \rightarrow 3I^- + O_2 + 2H^+ \tag{4.2}$$

The degree of suppression of the backward reaction (Eq. 4.1) is in good agreement with the increase of the oxidation efficiency at increasing acidity (Fig. 4.5). This mechanism does not explain the increased breakdown of different organic compounds when using air as a saturation gas instead of argon under varying conditions (20–300 kHz, 15–200 W, 0.005–5 mmol L^{-1}, 50–300 mL)[19–25]. Other reactions such as the pyrolysis of the compounds may play a role in those studies. Carbon dioxide additition can also increase the nucleation rate due to a surface tension suppression in the liquid[43–46]. A higher radical production rate can be obtained if more active bubbles are formed.

4.4 Conclusions

The rate of sonochemical potassium iodide oxidation has been measured in water saturated with binary and ternary mixtures of argon, oxygen, nitrogen, and carbon dioxide at constant power input and ultrasound frequency. A linear relationship has been observed for the triiodide oxidation yield in the both nitrogen-argon and nitrogen-oxygen mixtures. A maximum radical production rate of 14×10^{-10} mol J^{-1} is observed in the 20 vol% oxygen in argon mixture. The oxidation efficiency under air was 3 times higher as compared to that in the 20 vol% oxygen in nitrogen mixture. Addition of carbon dioxide to a 20 vol% oxygen-80 vol% nitrogen mixture reduced this difference to a factor of 1.3. This is likely due to acidification by carbon dioxide. Addition of low amounts of carbon dioxide (up to 3 vol%) to argon-oxygen feed gas as well as an addition of an acid also increases potassium iodide oxidation efficiency. A mechanism for this observation can be the suppression of the reaction between triiodine and hydrogen peroxide at low pH.

Bibliography

[1] T. G. Leighton, The acoustic bubble, Academic Press, London, 1994.

[2] R. Löfstedt, K. Weninger, S. Putterman, B. P. Barber, Sonoluminescing bubbles and mass diffusion, Physical Review E: Statistical, Nonlinear, and Soft Matter Physics 51(5) (**1995**) 4400–4410. `doi:10.1103/PhysRevE.51.4400`.

[3] D. J. Flannigan, K. S. Suslick, Plasma formation and temperature measurement during single-bubble cavitation, Nature 434(7029) (**2005**) 52–55. `doi:10.1038/nature03361`.

[4] K. R. Weninger, C. G. Camara, S. J. Putterman, Energy focusing in a converging fluid flow: Implications for sonoluminescence, Physical Review Letters 83(10) (**1999**) 2081–2084. `doi:10.1103/PhysRevLett.83.2081`.

[5] Y. T. Didenko, W. B. McNamara III, K. S. Suslick, Effect of noble gases on sonoluminescence temperatures during multibubble cavitation, Physical Review Letters 84(4) (**2000**) 777–780. `doi:10.1103/PhysRevLett.84.777`.

[6] S. Hirayama, H. Morinaga, T. Ohmi, J.-I. Soejima, Sonoluminescence measurement of 1 MHz ultrasonic cavitation and effect of dissolved gases, Acoustical Science and Technology 29(6) (**2008**) 345–350. `doi:10.1250/ast.29.345`.

[7] M. P. Brenner, S. Hilgenfeldt, D. Lohse, Why air bubbles in water glow so easily, Nonlinear physics of complex systems – Current status and future trends, Springer Berlin, 1996, Ch. 8, pp. 79–97. `doi:10.1007/BFb0105431`.

[8] Y. Iida, K. Yasui, T. Tuziuti, M. Sivakumar, Sonochemistry and its dosimetry, Microchemical Journal 80(2) (**2005**) 159–164. `doi:10.1016/j.microc.2004.07.016`.

[9] G. Mark, A. Tauber, R. Laupert, H.-P. Schuchmann, D. Schulz, A. Mues, C. von Sonntag, OH-radical formation by ultrasound in aqueous solution – part II: Terephthalate and Fricke dosimetry and the influence of various conditions on the sonolytic yield, Ultrasonics Sonochemistry 5(2) (**1998**) 41–52. `doi:10.1016/S1350-4177(98)00012-1`.

[10] N. Segebarth, O. Eulaerts, Y. Kegelaers, J. Vandercammen, J. Reisse, About the Janus double-horn sonicator and its use in quantitative homogenous sonochemistry, Ultrasonics Sonochemistry 9(2) (**2002**) 113–119. `doi:10.1016/S1350-4177(01)00112-2`.

[11] D. V. Prasad Naidu, R. Rajan, R. Kumar, K. S. Gandhi, V. H. Arakeri, S. Chandrasekaran, Modelling of a batch sonochemical reactor, Chemical Engineering Science 49(6) (**1994**) 877–888. `doi:10.1016/0009-2509(94)80024-3`.

[12] T. Kondo, M. Kuwabara, F. Sato, E. Kano, Influence of dissolved gases on chemical and biological effects of ultrasound, Ultrasound in Medicine and Biology 12(2) (**1986**) 151–155. `doi:10.1016/0301-5629(86)90020-7`.

[13] K. S. Suslick, M. M. Mdleleni, J. T. Ries, Chemistry induced by hydrodynamic cavitation, Journal of the American Chemical Society 119(39) (**1997**) 9303–9304. `doi:10.1021/ja972171i`.

[14] A. Brotchie, T. Statham, M. Zhou, L. Dharmarathne, F. Grieser, M. Ashokkumar, Acoustic bubble sizes, coalescence, and sonochemical activity in aqueous electrolyte solutions saturated with different gases, Langmuir 26(15) (**2010**) 12690–12695. `doi:10.1021/la1017104`.

[15] D. G. Wayment, D. J. Casadonte Jr., Design and calibration of a single-transducer variable-frequency sonication system, Ultrasonics Sonochemistry 9(4) (**2002**) 189–195. `doi:10.1016/S1350-4177(01)00127-4`.

[16] E. L. Mead, R. G. Sutherland, R. E. Verrall, The effect of ultrasound on water in the presence of dissolved gases, Canadian Journal of Chemistry 54 (**1976**) 1114–1120.

[17] M. H. Entezari, P. Kruus, Effect of frequency on sonochemical reactions. I: Oxidation of iodide, Ultrasonics Sonochemistry 1(2) (**1994**) S75–S79. `doi:10.1016/1350-4177(94)90001-9`.

[18] J. Rooze, E. V. Rebrov, J. C. Schouten, J. T. F. Keurentjes, Effect of resonance frequency, power input, and saturation gas type on the oxidation efficiency of an ultrasound horn, Ultrasonics Sono-

chemistry 18(1) (**2011**) 209–215. `doi:10.1016/j.ultsonch.2010.05.007`.

[19] Q. Hong, J. L. Hardcastle, R. A. J. McKeown, F. Marken, R. G. Compton, The 20 kHz sonochemical degradation of trace cyanide and dye stuffs in aqueous media, New Journal of Chemistry 23 (**1999**) 845–849. `doi:10.1039/a903990b`.

[20] T. Sivasankar, V. S. Moholkar, Mechanistic approach to intensification of sonochemical degradation of phenol, Chemical Engineering Journal 149(1–3) (**2009**) 57–69. `doi:10.1016/j.cej.2008.10.004`.

[21] Y. Nagata, M. Nakagawa, H. Okuno, Y. Mizukoshi, B. Yim, Y. Maeda, Sonochemical degradation of chlorophenols in water, Ultrasonics Sonochemistry 7(3) (**2000**) 115–120. `doi:10.1016/S1350-4177(99)00039-5`.

[22] R. Kidak, N. Ince, Effects of operating parameters on sonochemical decomposition of phenol, Journal of Hazardous Materials 137(3) (**2006**) 1453–1457. `doi:10.1016/j.jhazmat.2006.04.021`.

[23] R. A. Torres, C. Pétrier, E. Combet, M. Carrier, C. Pulgarin, Ultrasonic cavitation applied to the treatment of bisphenol A. Effect of sonochemical parameters and analysis of BPA by-products, Ultrasonics Sonochemistry 15(4) (**2008**) 605–611. `doi:10.1016/j.ultsonch.2007.07.003`.

[24] I. Gültekin, N. H. Ince, Ultrasonic destruction of bisphenol-A: The operating parameters, Ultrasonics Sonochemistry 15(4) (**2008**) 524–529. `doi:10.1016/j.ultsonch.2007.05.005`.

[25] Y. Kojima, T. Fujita, E. P. Ona, H. Matsuda, S. Koda, N. Tanahashi, Y. Asakura, Effects of dissolved gas species on ultrasonic degradation of (4-chloro-2-methylphenoxy) acetic acid (MCPA) in aqueous solution, Ultrasonics Sonochemistry 12(5) (**2005**) 359–365. `doi:10.1016/j.ultsonch.2004.04.002`.

[26] D. G. Wayment, D. J. Casadonte Jr., Frequency effect on the sonochemical remediation of alachlor, Ultrasonics Sonochemistry 9(5) (**2002**) 251–257. `doi:10.1016/S1350-4177(02)00081-0`.

[27] M. Helal Uddin, S. Hayashi, Effects of dissolved gases and pH on sonolysis of 2,4-dichlorophenol, Journal of Hazardous Materials 170(2–3) (**2009**) 1273–1276. `doi:10.1016/j.jhazmat.2009.05.130`.

[28] C. Pétrier, M. Micolle, G. Merlin, J.-L. Luche, G. Reverdy, Characteristics of pentachlorophenate degradation in aqueous solution by means of ultrasound, Environmental Science and Technology 26(8) (**1992**) 1639–1642. `doi:10.1021/es00032a023`.

[29] I. Hua, R. H. Höchemer, M. R. Hoffmann, Sonochemical degradation of p-nitrophenol in a parallel-plate near-field acoustical processor, Environmental Science & Technology 29(11) (**1995**) 2790–2796. `doi:10.1021/es00011a014`.

[30] M. A. Beckett, I. Hua, Elucidation of the 1,4-dioxane decomposition pathway at discrete ultrasonic frequencies, Environmental Science and Technology 34(18) (**2000**) 3944–3953. `doi:10.1021/es000928r`.

[31] J. D. Schramm, I. Hua, Ultrasonic irradiation of dichlorvos: Decomposition mechanism, Water Research 35(3) (**2001**) 665–674. `doi:10.1016/S0043-1354(00)00304-3`.

[32] M. Gutiérrez, A. Henglein, F. Ibañez, Radical scavenging in the sonolysis of aqueous solutions of iodide, bromide, and azide, The Journal of Physical Chemistry 95(15) (**1991**) 6044–6047. `doi:10.1021/j100168a061`.

[33] J. Büttner, M. Gutiérrez, A. Henglein, Sonolysis of water-methanol mixtures, The Journal of Physical Chemistry 95(4) (**1991**) 1528–1530. `doi:10.1021/j100157a004`.

[34] V. Ragaini, E. Selli, C. L. Bianchi, C. Pirola, Sono-photocatalytic degradation of 2-chlorophenol in water: kinetic and energetic comparison with other techniques, Ultrasonics Sonochemistry 8(3) (**2001**) 251–258. `doi:10.1016/S1350-4177(01)00085-2`.

[35] I. Hua, J. E. Thompson, Inactivation of Escherichia coli by sonication at discrete ultrasonic frequencies, Water Research 34(15) (**2000**) 3888–3893. `doi:10.1016/S0043-1354(00)`

`00121-4`.

[36] J.-W. Waanders, Piezoelectric Ceramics, Properties & Applications, Philips Components, Eindhoven, 1991.

[37] D. A. Palmer, R. W. Ramette, R. E. Mesmer, Triiodide ion formation equilibrium and activity coefficients in aqueous solution, Journal of Solution Chemistry 13(9) (**1984**) 673–683. `doi:10.1007/BF00650374`.

[38] G. v. Elbe, B. Lewis, Thermal equilibrium between oxygen molecules and atoms, Journal of the American Chemical Society 55(2) (**1933**) 507–511. `doi:10.1021/ja01329a010`.

[39] S. Merouani, O. Hamdaoui, F. Saoudi, M. Chiha, Influence of experimental parameters on sonochemistry dosimetries: KI oxidation, fricke reaction and H_2O_2 production, Journal of Hazardous Materials 178(1–3) (**2010**) 1007–1014. `doi:10.1016/j.jhazmat.2010.02.039`.

[40] D. Drijvers, R. de Baets, A. de Visscher, H. van Langenhove, Sonolysis of trichloroethylene in aqueous solution: volatile organic intermediates, Ultrasonics Sonochemistry 3(2) (**1996**) S83–S90. `doi:10.1016/1350-1477(96)00012-3`.

[41] D. Drijvers, H. van Langenhove, K. Vervaet, Sonolysis of chlorobenzene in aqueous solution: organic intermediates, Ultrasonics Sonochemistry 5(1) (**1998**) 13–19. `doi:10.1016/S1350-4177(98)00006-6`.

[42] Y. Jiang, C. Pétrier, T. D. Waite, Effect of pH on the ultrasonic degradation of ionic aromatic compounds in aqueous solution, Ultrasonics Sonochemistry 9(3) (**2002**) 163–168. `doi:10.1016/S1350-4177(01)00114-6`.

[43] S. D. Lubetkin, Why is it much easier to nucleate gas bubbles than theory predicts?, Langmuir 19(7) (**2003**) 2575–2587. `doi:10.1021/la0266381`.

[44] H.-Y. Kwak, S.-D. Oh, Gas-vapor bubble nucleation – a unified approach, Journal of Colloid and Interface Science 278(2) (**2004**) 436–446. `doi:10.1016/j.jcis.2004.06.020`.

[45] Y. Mori, K. Hijikata, T. Nagatani, Effect of dissolved gas on bubble nucleation, International Journal of Heat and Mass Transfer 19(10) (**1976**) 1153–1159. `doi:10.1016/0017-9310(76)90149-6`.

[46] J. Rooze, E. V. Rebrov, J. C. Schouten, J. T. F. Keurentjes, Dissolved gas and cavitation: a review, Ultrasonics Sonochemistry, Accepted.

Mechanism of ultrasound scission of a silver-carbene coordination polymer

5

Scission of a supramolecular polymer-metal complex can be carried out using collapsing cavitation bubbles created by ultrasound. Although the most plausible scission mechanism of the coordinative bonds is through mechanical force, the influence of radicals and high hot-spot temperatures on scission has to be considered. A silver(I)-N-heterocyclic carbene complex was exposed to 20 kHz ultrasound in argon, nitrogen, methane, and isobutane saturated toluene. Scission percentages were almost equal under argon, nitrogen, and methane. Radical production differs by a factor of 10 under these gases, indicating that radical production is not a significant contributor to the scission process. A model to describe the displacement of the bubble wall, strain rates, and temperature in the gas shows that critical strain rates for coil-to-stretch transition, needed for scission, can be achieved at reactor temperatures of 298 K, an acoustic pressure of 1.2×10^5 Pa, and an acoustic frequency of 20 kHz. Lower scission percentages were measured under isobutane, which also shows lower strain rates in model simulations. The activation of the polymer-metal complexes in toluene under the influence of ultrasound occurs through mechanical force.

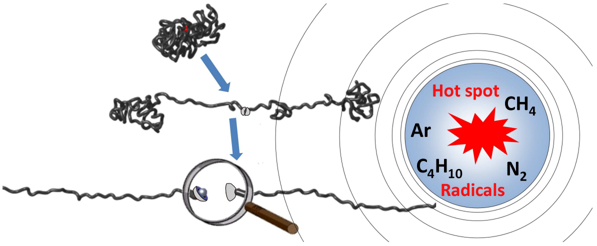

This Chapter has been published as: J. Rooze, R. Groote, R. T. M. Jakobs, R. P. Sijbesma, M. M. van Iersel, E. V. Rebrov and J. C. Schouten and J. T. F. Keurentjes, Mechanism of ultrasound scission of a silver-carbene coordination polymer, *The Journal of Physical Chemistry B* 115(38) (**2011**) 11038 – 11043

5.1 Introduction

Chemical bonds can be activated by mechanical forces, instead of by using conventional means such as thermal or photochemical activation.[1,2] The energy landscape of mechanically and thermally activated reactions is sometimes substantially different, resulting in different reaction pathways for each activation method[2–5]. A handle is required for efficient transduction of (external) mechanical forces onto the chemical bond that needs to be activated. Polymer chains have shown to be very effective for this purpose[1,5–11]. The use of mechanical forces to carry out chemical transformation within molecules has recently gained interest as it opens the way to the development of mechanoresponsive materials (*e.g.* materials that give a color change upon strain[6], or self-healing materials). In this respect it is especially interesting to look at activation of catalytic processes induced by mechanical forces (mechanocatalysis)[10–12]. Recent work has shown the promising prospects of using mechanical forces for activation of latent transition metal complexes[10–12], which can subsequently be used as catalysts. Transesterification and metathesis reactions have been successfully performed by subjecting a solution of the polymer mechanocatalyst complexes to ultrasound irradiation in the presence of reactants. Activation of the organometallic complexes is achieved by breakage of the coordination bond between the metal center and the N-heterocyclic carbene (NHC) ligand. This leads to either an active ruthenium(II)-NHC Grubbs catalyst, widely used as an olefin metathesis catalyst[13], or to a free NHC, which is an organocatalyst commonly used in *e.g.* ring-opening polymerisation reactions of cyclic esters[14–16] and transesterification reactions[11,17,18]. The silver(I)-NHC complex is of interest in this study as it has a low critical molecular weight for scission with ultrasound[11]. The polymer chains attached to the complex are short and scission can therefore be measured directly by ^{1}H NMR spectroscopy. A free NHC is formed in solution when scission of the silver(I)-NHC bond occurs (see Fig. 5.1), which can re-coordinate to a silver(I) ion since the complexed and free NHCs are in a dynamic equilibrium. However, if a source of protons (such as water) is present, the strongly basic NHC is converted to the corresponding imidazolium salt and reformation of the complex is prevented. The solvent toluene was saturated with water to scavenge the free NHCs during the sonication experiments.

Ultrasound in a liquid can create the forces needed for mechanoscission, by inducing growth of gaseous nuclei, which subsequently collapse[19]. This process is called cavitation and it may lead to radical formation[20], high heating and cooling rates[21], and polymer scission[22]. Radical formation results from the dissociation of gas molecules at the high temperatures and pressures inside the bubble during the collapse due to compression. High temperatures are also reached because the collapse time is shorter than the relevant times for mass and heat transfer. Polymer scission is caused by the high strain rates generated at the

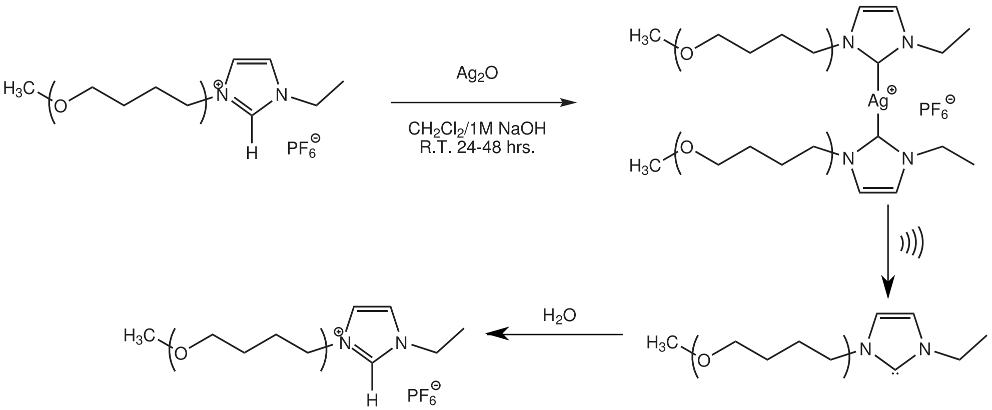

Figure 5.1: Schematic overview of the synthesis and mechanochemical scission of the silver(I)-NHC polymer catalyst complex by ultrasound and the subsequent reaction of the free NHC with water.

bubble wall. The strain rates are in the order of 10^7 s^{-1} [9,22,23]. The resulting forces are large enough to induce stretching and breaking of a covalent bond in a polymer above a critical molecular weight[22,24]. There is a strong influence of gas solubility on the efficiency of an ultrasonic scission process as was demonstrated in work by Price *et al.* on scission of covalent polymers[25]. They found that ultrasonic scission was less efficient under gases with a high solubility.

Here, the relative contributions of mechanical scission, thermal, and radical-induced dissociation mechanisms to ultrasonic scission of a silver(I)-NHC coordination bond are investigated. The bubble internal and interface temperatures and the radical production rate are varied by using different saturation gases (argon, nitrogen, methane, and isobutane) during ultrasound experiments. Both polymer scission and radical production experiments are compared with a model of the radial dynamics of a gas bubble under influence of an ultrasound field in order to identify the relevant scission pathways. The scission and radical production experiments are presented first, followed by a qualitative interpretation of the results using the model.

5.2 Experimental

5.2.1 Synthesis of the polymer-metal complex

All solvents used in the synthesis and work-up were obtained from BioSolve and of at least AR grade quality and used without further purification, unless otherwise stated. N-ethyl imidazole-terminated ω-methoxy poly(tetrahydrofuran) polymer was synthesised via cationic ring-opening polymerization of 75 mL tetrahydrofuran (THF) using 100 µL methyl triflate (purity 98 %, Sigma-Aldrich) as initiator[11], and 50 µL di-tert-butyl pyridine (Sigma-Aldrich) was added as a base. The polymerisation was carried out under inert argon atmosphere using Schlenk line techniques. THF was dried and purified by passage over an alumina-packed column prior to use. After 2.5 hours the polymerisation was terminated by adding approximately 200 µL (2 molar equivalents with respect to the initiator) of N-ethyl imidazole (98 %, TCI). The polymer was obtained as white powder in good quantity after precipitation of the crude polymer (obtained as a colourless oil) in water (overnight at ambient temperature) and diethyl ether (overnight at 253 K). Ion exchange to the chloride anion was carried out by stirring the polymer with Dowex® exchange resin (1×8 50–100 mesh, Acros) in methanol for 2–3 hours. The exchange resin was then removed by filtration and the methanol was evaporated *in vacuo*. Subsequent ion exchange of the chloride to the hexafluorophosphate (PF_6^-) anion was carried out by stirring the polymer in the presence of an excess (1.1–1.5 equivalents) of ammonium hexafluorophosphate (99.99 %, Acros) in methanol for 2–3 hours, followed by evaporation of the solvent *in vacuo*. The polymer was characterised after synthesis and work-up by ^{1}H NMR in acetone-d_6 (Cambridge Isotope Laboratories, Inc.) on a 400 MHz Varian spectrometer to confirm end-group functionalisation of the polymer and to determine the number-average molecular weight, M_n. Gel permeation chromatography (GPC) was carried out on a Polymer Laboratories PL-GPC 50 system using DMF/LiBr as eluent. ^{1}H NMR analysis confirmed end-functionalization with N-ethyl imidazole and gave an estimated number-average molecular weight of 7.82 kg mol^{-1}. This value is in good agreement with the results obtained from GPC analysis on this polymer: M_n = 7.18 kg mol^{-1} with a narrow polydispersity index (1.11). A typical ^{1}H NMR spectrum of the polymer is provided in the Appendices.

Complexation of the N-ethyl imidazole-terminated polymer with silver(I) was typically performed by stirring 500 mg polymer with an excess of silver(I) oxide (99 %, Sigma-Aldrich) in 5–10 mL dichloromethane and 1 mL 1M NaOH solution for 24–48 hours at ambient temperature. Approximately 5 mg tetrabutyl ammonium hexafluorophospate (98 %, Acros) was added as phase transfer catalyst. Work-up of the complex was done by separating the dichloromethane/water layers, followed by filtration of the dichloromethane layer over celite to adsorb small ionic species. The filtrate was dried with magnesium sulfate and filtered. The dichloromethane was subsequently evaporated to obtain the polymer complex in good yields. A typical ^{1}H NMR spectrum of the complex is provided as an Appendix to this chapter.

5.2.2 Sonication experiments

Scission experiments A home made, double-jacketed glass reactor with a volume of 10 mL was used in the sonication experiments. A Sonics and Materials 20-kHz, 0.5 inch diameter titanium alloy ultrasound probe with half wave extension (parts 630-0220 and 630-0410) was operated using a Sonics and Materials VC750 power supply. The temperature in the reactor was maintained with a Lauda E300 cooling bath and measured using a 0.5 mm diameter thermocouple. Isobutane (99.5 vol. %, Linde), methane (99.995 vol. %, Linde), nitrogen (99.999 vol. %, Linde, or argon (99.996 vol. %, Linde) was bubbled at 5 mL min^{-1} through the experimental solution for at least 30 minutes prior to, and during all experiments. The gas flow rate was controlled using a mass flow controllers (Bronkhorst High-Tech B.V., F-201CV).

The polymer-metal complex (15 mg) was dissolved in 5 mL toluene (AR grade, Biosolve) that was saturated with demineralised water prior to use. The solution was then transferred into the reactor and was allowed to saturate with argon, nitrogen, methane or isobutane for at least 30 minutes prior to sonication. During this time the solution was kept at 283 K. The solution was sonicated for 5 minutes at 25 % of the maximum amplitude (corresponding to an input power into the liquid of 12–17 W, varying per experiment) after gas saturation. The solution temperature inside the reactor increased to 301 ± 4 K during the first minute, and was constant afterwards. The whole solution was removed from the reactor when the sonication was stopped and the solvent was evaporated *in vacuo*. The residual solid was redissolved in ca. 600 µL acetone-d_6 to allow determination of the extent of scission by ^{1}H NMR (see the appendices for details on the analysis procedure). The scission percentage is defined as the fraction of the integrated NMR peak of the ligand over that of the initial complex (see Appendix).

Radical formation experiments A volume of 10 mL of the radical scavenger 1,1-diphenyl-2-picryl-hydrazyl (DPPH) with a concentration of 30 µmol L^{-1} in toluene (99.8 wt. %, Aldrich) was sonicated for 5–30 minutes after saturation at a temperature of 279–288 K with argon, nitrogen, methane or isobutane. The power delivered to the liquid was 10–30 W (20–30 % of the maximum amplitude). The initial temperature was varied so that the final temperature was 298 ± 3 K after 1 minute. DPPH reacts to 2,2-diphenyl-l-picrylhydrazine ($\mathrm{DPPH_2}$) with H radicals, if present[26–28]. UV spectroscopy (Shimadzu 2501-PC) was used for product analysis. Absorption peaks at 330 and 520 nm were assigned to DPPH and that at 380 nm to $\mathrm{DPPH_2}$. The 520 nm peak was selected for analysis because it was relatively isolated from the other peaks. Gaussian peak fitting between 440 and 580 nm with a $\mathrm{DPPH_2}$ baseline correction yielded concentration values. The number of experiments was at least 6 for each gas, with 1 to 6 sample points per experiment. Only the measurements obtained in the linear part of DPPH concentration decline were used when calculating the reaction rate.

5.2.3 Bubble oscillation model

The bubble oscillation model of van Iersel *et al.*[29] which is based on the model by Yasui[30] has been used to describe the displacement of the wall of a spherical gas bubble in a Newtonian liquid under influence of a pressure field. It also describes thermodynamic properties such as the bubble temperature and pressure. The model consists of a Keller-Miksis variation of the Rayleigh-Plesset equation[31], a Hertz-Knudsen-Langmuir description of vapour transport across the bubble-liquid interface[30], coupled with Maxwell-Stefan diffusion equations[32], and an energy balance (see the appendices for the equations and pure-component properties, further elaboration on the model and its assumptions is present in literature[29]).

The model has been simplified in order to make it more robust. The ideal gas equation has been used for the description of the gas in the cavity instead of the Van der Waals-equation because the latter gives singularities in a number of simulations when the pressure approached the maximum theoretical Van der Waals pressure. Hot spot temperature changes by chemical reactions have not been taken into account in this model. The relation $\dot{\epsilon} = -2\dot{R}/R$ has been used to calculate the strain rate at the wall of a collapsing bubble[9,33], where $\dot{\epsilon}$ is the strain rate, $\dot{R}$ is the bubble wall velocity, and R is the bubble radius. It is expected that the scission percentage scales with the strain rate, because the critical strain rate is attained in a larger volume around the collapsing bubble at increasing strain rate near the bubble wall. The silver-NHC complex chains have to be (partially) extended by the strain rates before the polymer complex can undergo mechanical scission[9,24,34]. The transition of conformation of a polymer chain from a random coil to a stretched state occurs when $\dot{\epsilon} \times \lambda_0 \approx 1$[24,34], where λ_0 is the relaxation time. Determination of the relaxation times of these polymer-metal complexes based on viscosity measurements has shown that the critical strain rates for coil-to-stretch transition are in the order of 10^6–10^7 s^{-1}. [1]

The NDsolve function with varying time step in Mathematica (Wolfram Research, version 6.0.3.0) has been used to solve the system of ordinary differential equations and linear equations, using the model settings shown in Table 5.1. The interface temperature has been used as an indication for the degree of thermal scission. The possible effect of droplet injection from a distorted bubble interface[37] is not taken into account. Bubble oscillations have

---

[1] The longest characteristic relaxation time of a polymer chain in dilute solution is calculated according to $\lambda_0 = [\eta]_0 \times \eta_{\mathrm{solvent}} M R_g^{-1} T^{-1}$[35]. For covalent poly(tetrahydrofuran) in toluene the intrinsic viscosity $[\eta]_0 = 5.5 \times 10^{-3} M^{0.78}$ L g^{-1},[36] the viscosity of toluene $\eta_{\mathrm{solvent}} \approx 10^{-3}$ Pa s^{-1} and $R_g T$ is 2500 J mol^{-1} at room temperature. Substitution of the values results in $\lambda_0 \approx 2.2 \times 10^{-9} M^{1.78}$ s. This results in a longest characteristic relaxation time of the polymer chain of $\lambda_0 \approx 10^{-7}$ s with $M \approx 10$ kg mol^{-1}.

been calculated for multiple initial bubble radii from 1 to 50 µm with a step of 1 µm). The results obtained can not directly be related to a bubble in the multi bubble field generated in the experiments since the sound field inside the liquid is not expected to be uniform due to distortions and reflections by other bubbles, and due to possible break-up of the bubble during the collapse. Interpretation of the results by comparing various gases and liquids yields the most insight. Conclusions have been drawn based on comparisons.

Table 5.1: Model parameters.

Parameter	Symbol	Value
Acoustic pressure	P_a	1.2×10^5 N m^{-2}
Frequency	f	20 kHz
Initial pressure	P_0	1.0×10^5 N m^{-2}
Initial temperature	T_0	298 K

5.3 Results and discussion

5.3.1 Sonication of polymer complex solutions

The measured scission percentages of the silver(I)-NHC complex in argon, nitrogen, and methane saturated toluene after 5 minutes of sonication are similar (11 – 14 %, see Fig. 5.2). A slightly lower scission percentage of 6 % is observed in an isobutane saturated toluene solution. The thermal background conversion at 283 K in toluene measured without exposure to ultrasound is less than 1 %. When the silver(I)-NHC complex in toluene is kept at 383 K for one hour, 20 % scission is observed.

5.3.2 Radical formation measurements

The radical formation rate has been measured spectroscopically using the radical scavenger DPPH. Reaction yields are shown in Fig. 5.3. The highest reaction yield of 23×10^{-10} mol L^{-1} J^{-1} is found under argon. An intermediate reaction yield of 11×10^{-10} mol L^{-1} J^{-1} is found under nitrogen, and low reaction yields of 1.1 and 1.4×10^{-10} mol L^{-1} J^{-1}, respectively, under methane and isobutane (see Fig. 5.3). The measured reaction constants of DPPH conversion under argon (17 – 70 nmol L^{-1} s^{-1}) are of the same order of magnitude as to those measured by Suslick *et al.* (36 nmol L^{-1} s^{-1}) under similar conditions[28].

There is a different trend in the radical and scission experiments when varying the dissolved gas type; only a small difference between the efficacy of the gases is seen in the

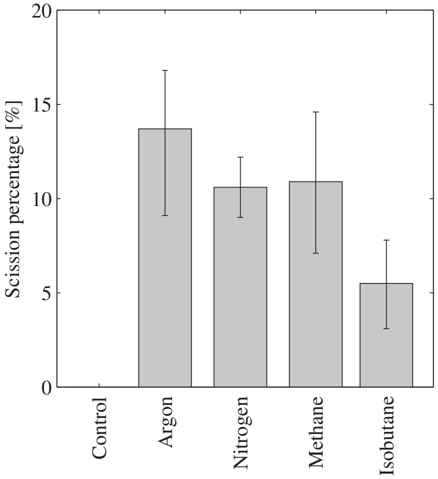

Figure 5.2: Scission percentage of silver(I)-NHC complex in toluene at 301 K saturated with argon, nitrogen, methane, and isobutane after 5 minutes of sonication and a power input of 16, 17, 15, and 12 W, respectively. The percentage of scission is averaged over two or three experiments. The error bars are the minimum and maximum value. No scission is observed in control experiments.

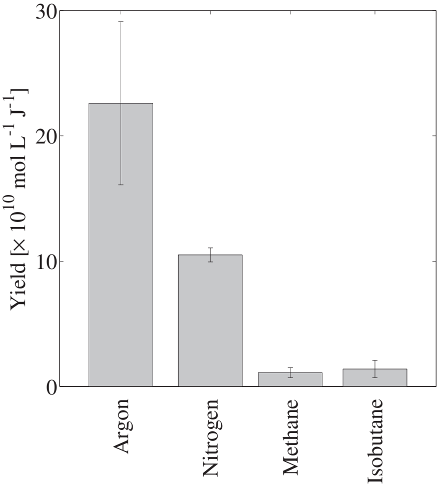

Figure 5.3: $DPPH_2$ production per Joule energy input at 298 K in argon, nitrogen, methane, and isobutane saturated toluene. The error bars represent the standard deviation.

scission experiments, and a large difference in the radical experiments. These results are consistent with previous experimental work on scission with polymers of varying length[11], and indicate that radical production has a negligible influence on the scission process.

5.3.3 Modeling

A model has been used to obtain insight into the possible activation pathways. The bubble radii for argon, nitrogen, and methane saturated toluene are approximately the same during the ultrasound cycle, therefore only results for argon and isobutane saturated solutions are depicted in Fig. 5.4. The strain rates are larger than 10^7 s^{-1}, which is the estimated strain rate for coil-to-stretch transition of the polymer-metal complexes under all gases except isobutane at small initial radii (< 8 µm). The strain rate at collapse in the isobutane saturated toluene solution is lower than that of the other gases due to a slower collapse. The collapse is cushioned by a higher number of isobutane molecules inside the bubble in isobutane saturated toluene than in argon saturated toluene. The strain rates averaged over all collapses and all initial bubble radii are between 65 and 75 × 10^6 s^{-1} for argon, nitrogen, and methane-saturated toluene, and 9 × 10^6 s^{-1} when using isobutane. This trend is similar to that observed in scission experiments, where these argon, nitrogen, and methane have approximately equal scission percentages, as opposed to isobutane which has a lower scission percentage.

A hot spot is formed during the collapse due to compression of the gas. The heat that is released is subsequently transported to the gas-liquid interface, and further into the liquid[38]. The maximum hot spot temperatures in the gas vary with the heat capacity of the gases. The calculated temperatures are given as maximum values for each initial radius averaged over all initial radii, with the standard deviation. The hot spot temperature in the calculations is 580 ± 50 K for argon, 560 ± 40 K for nitrogen, 520 ± 30 K for methane, and 460 ± 10 K for isobutane. The larger the initial bubble radius, the lower the bubble vapour content, and the higher the hot spot temperature. The heat capacity changes with the density and is therefore a factor 1000 higher in the liquid than in the gas, and lower temperatures are therefore expected in the liquid. The maximum liquid interface temperature averaged over all initial bubble radii is 335 ± 20 K under argon, nitrogen, and methane, and 310 ± 10 K under isobutane. The calculated temperatures are lower than those reported in literature obtained spectroscopically by Didenko *et al.* for octanol (4300 K) and dodecane (3200 K)[39]. These solvents have a much lower vapour pressure (3 and 9 Pa, respectively) than toluene (1300 Pa) and therefore much higher hot spot temperatures are expected. Mišík and Riesz[40] have reported a hot spot temperature in toluene measured by thermometry of 6300 K. The reason for the discrepancy between these results and the temperatures obtained by Didenko *et al.* is unknown, possibly the ultrasound conditions are different for both experiments.

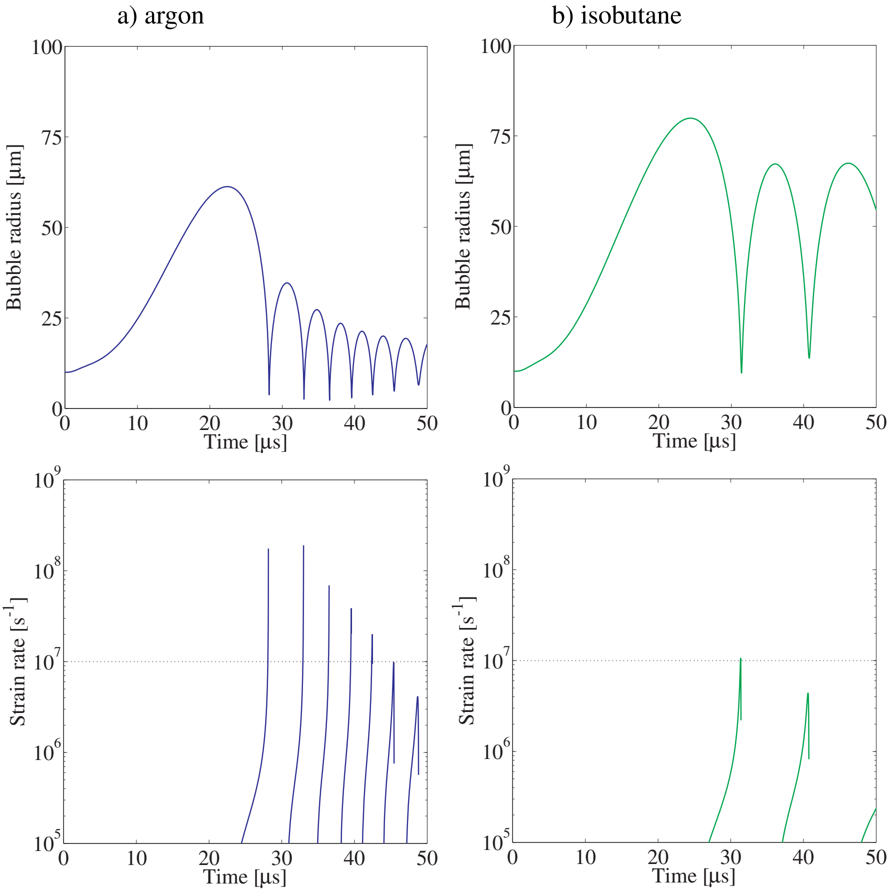

Figure 5.4: Modeled radial dynamics (top) and strain rate (bottom) for oscillation of a bubble with an initial radius of 10 µm in toluene saturated with a) argon and b) isobutane.

The model provides insight into the relations between hot spot and interface temperature, strain rates and bubble collapse velocity, heat capacity and heat conduction, and gas solubility. The strain rate and the hot spot temperature vary with the dissolved gas, although a constant scission value is measured experimentally in toluene. The strain rates averaged over multiple collapses and initial bubble radii are similar for argon, nitrogen, and methane. The calculated values of strain rate and hot spot temperature cannot be considered quantitative since they strongly depend on the conditions upon collapse. The assumptions of the model and the equation of state are not valid anymore at in the final stage of bubble collapse, and the model results can therefore only be considered in a qualitative way. Thermal dissociation of the silver(I)-NHC bond can not be excluded at the calculated liquid interface temperatures. The radical production experiments can be qualitatively evaluated using results from the model. Szwarc reports pyrolysis of toluene at temperatures of 738 K and higher[41]. This temperature is feasible in hot spots during ultrasonic cavitation, although the modeled hot spot temperatures are lower (the maximum temperature obtained is 690 K for an argon bubble with an initial radius of 46 µm). However, the calculated temperatures are averaged over the entire bubble volume, so the temperatures in the center of the bubble are expected to be higher than the average values. The experimental radical production rate coefficients qualitatively agree with modeled maximum hot spot temperatures, where the experiments with higher hot spot temperatures had higher radical production rates than those with lower hot spot temperatures. The hot spot interface temperatures are moderate, around 335 K, but may be a cause for thermal scission. However, the complex is not necessarily present at the gas-liquid interface, and may therefore experience a lower temperature.

The gas solubility seems to have a strong influence on radial dynamics, strain rates, and temperature maxima, which has been reported before using several observation methods (covalent polymer scission, sonoluminescence, and radical production)[25,42–44]. The gases with a higher solubility showed less intense cavitation effects in these studies. Cushioning of the collapse by mass transport into the bubble may be a cause for these effects.

5.4 Conclusions

Scission of a polymer silver(I)-N-heterocyclic carbene complex by ultrasound has been investigated experimentally and theoretically to provide insight into the most likely scission mechanism. The mechanisms considered include thermal scission, scission by radicals, and mechanical scission by strain imposed on the polymer chain during collapse of the cavitation bubble.

Experimental studies have been performed using argon, nitrogen, methane, and isobutane as saturation gases in toluene. The physical properties of the cavitation bubble have been varied in order to be able to discern the dominant scission mechanism. Scission after five minutes of sonication varied by a factor of approximately 2, from 6 % under isobutane to 11–14 % for the other gases. Experiments using DPPH as a radical scavenger showed that the radical production rate varied by an order of magnitude using the various saturation gases. These experimental findings, which are supported by numerical modeling of the cavitation bubble collapse, indicate that the effect of radicals can be excluded as the predominant mechanism for polymer chain scission. Modeling also indicated that solvent temperature increase at the bubble interface is moderate. The numerical simulations have indicated that the critical strain rates required to fulfill the coil-to-stretch can be achieved in the sonication experiments. Therefore mechanical forces in solution arising from the collapse of cavitation bubbles are the most likely cause of scission. This conclusion is in line with the observation of molecular weight dependent scission rates[11], which also indicate a mechanical origin of scission by ultrasound.

It is of interest to implement the findings of this study in future work on mechanocatalysis experiments, such as transesterification reactions or ring-closing metathesis reactions using the Grubbs polymer catalyst.

Bibliography

[1] M. K. Beyer, H. Clausen-Schaumann, Mechanochemistry: The mechanical activation of covalent bonds, Chemical Reviews 105(8) (**2005**) 2921–2948. `doi:10.1021/cr030697h`.

[2] J. Ribas-Arino, M. Shiga, D. Marx, Understanding covalent mechanochemistry, Angewandte Chemie International Edition 48(23) (**2009**) 4190–4193. `doi:10.1002/anie.200900673`.

[3] J. Ribas-Arino, M. Shiga, D. Marx, Unravelling the mechanism of force-induced ring-opening of benzocyclobutenes, Chemistry: a European Journal 15(48) (**2009**) 13331–13335. `doi:10.1002/chem.200902573`.

[4] M. T. Ong, J. Leiding, H. Tao, A. M. Virshup, T. J. Martínez, First principles dynamics and minimum energy pathways for mechanochemical ring opening of cyclobutene, Journal of the American Chemical Society 131(18) (**2009**) 6377–6379. `doi:10.1021/ja8095834`.

[5] C. R. Hickenboth, J. S. Moore, S. R. White, N. R. Sottos, J. Baudry, S. R. Wilson, Biasing reaction pathways with mechanical force, Nature 446(7134) (**2007**) 423–427. `doi:10.1038/nature05681`.

[6] D. A. Davis, A. Hamilton, J. Yang, L. D. Cremar, D. Van Gough, S. L. Potisek, M. T. Ong, P. V. Braun, T. J. Martinez, S. R. White, J. S. Moore, N. R. Sottos, Force-induced activation of covalent bonds in mechanoresponsive polymeric materials, Nature 459(7243) (**2009**) 68–72. `doi:10.1038/nature07970`.

[7] J. M. J. Paulusse, Reversible mechanochemistry of coordination polymers and networks, Ph.D. thesis, Eindhoven University of Technology (2006).

[8] S. L. Potisek, D. A. Davis, N. R. Sottos, S. R. White, J. S. Moore, Mechanophore-linked addition polymers, Journal of the American Chemical Society 129(45) (**2007**) 13808–13809. `doi:10.1021/ja076189x`.

[9] M. W. Kuijpers, P. D. Iedema, M. F. Kemmere, J. T. F. Keurentjes, The mechanism of cavitation-

induced polymer scission; experimental and computational verification, Polymer 45(19) (**2004**) 6461–6467. `doi:10.1016/j.polymer.2004.06.051`.

[10] A. Piermattei, S. Karthikeyan, R. P. Sijbesma, Activating catalysts with mechanical force, Nature Chemistry 1(2) (**2009**) 133–137. `doi:10.1038/nchem.167`.

[11] S. Karthikeyan, S. L. Potisek, A. Piermattei, R. P. Sijbesma, Highly efficient mechanochemical scission of silver-carbene coordination polymers, Journal of the American Chemical Society 130(45) (**2008**) 14968–14969.

[12] A. G. Tennyson, K. M. Wiggins, C. W. Bielawski, Mechanical activation of catalysts for c-c bond forming and anionic polymerization reactions from a single macromolecular reagent, Journal of the American Chemical Society 132 (**2010**) 16631–16636. `doi:10.1021/ja107620y`.

[13] T. M. Trnka, R. H. Grubbs, The development of l2x2ru=chr olefin metathesis catalysts: An organometallic success story, Accounts of Chemical Research 34(1) (**2001**) 18–29. `doi:10.1021/ar000114f`.

[14] A. C. Sentman, S. Csihony, R. M. Waymouth, J. L. Hedrick, Silver(I)-carbene complexes/ionic liquids: Novel N-heterocyclic carbene delivery agents for organocatalytic transformations, Journal of Organic Chemistry 70(6) (**2005**) 2391–2393. `doi:10.1021/jo048555q`.

[15] N. E. Kamber, W. Jeong, S. Gonzalez, J. L. Hedrick, R. M. Waymouth, N-heterocyclic carbenes for the organocatalytic ring-opening polymerization of ϵ-caprolactone, Macromolecules 42(5) (**2009**) 1634–1639. `doi:10.1021/ma802618h`.

[16] N. Marion, S. Díez-González, S. Nolan, N-heterocyclic carbenes as organocatalysts, Angewandte Chemie International Edition 46(17) (**2007**) 2988–3000.

[17] G. A. Grasa, R. M. Kissling, S. P. Nolan, N-heterocyclic carbenes as versatile nucleophilic catalysts for transesterification/acylation reactions, Organic Letters 4(21) (**2002**) 3583–3586. `doi:10.1021/ol0264760`.

[18] R. Singh, R. M. Kissling, M.-A. Letellier, S. P. Nolan, Transesterification/acylation of secondary alcohols mediated by n-heterocyclic carbene catalysts, Journal of Organic Chemistry 69(1) (**2004**) 209–212. `doi:10.1021/jo035431p`.

[19] T. G. Leighton, The acoustic bubble, Academic Press, London, 1994.

[20] K. Makino, M. M. Mossoba, P. Riesz, Chemical effects of ultrasound on aqueous solutions. formation of hydroxyl radicals and hydrogen atoms, The Journal of Physical Chemistry 87(8) (**1983**) 1369–1377. `doi:10.1021/j100231a020`.

[21] K. S. Suslick, G. J. Price, Applications of ultrasound to materials chemistry, Annual Review of Materials Science 29(1) (**1999**) 295–326. `doi:10.1146/annurev.matsci.29.1.295`.

[22] A. M. Basedow, K. H. Ebert, Ultrasonic Degradation of Polymers in Solution, Springer-Verlag, Berlin, 1977.

[23] A. Weissler, Depolymerization by ultrasonic irradiation: The role of cavitation, Journal of Applied Physics 21(2) (**1950**) 171–173. `doi:10.1063/1.1699618`.

[24] J. A. Odell, A. Keller, A. J. Muller, Thermomechanical degradation of macromolecules, Colloid and Polymer Science 270(4) (**1992**) 307–324.

[25] G. J. Price, P. F. Smith, Ultrasonic degradation of polymer solutions: 2. The effect of temperature, ultrasound intensity and dissolved gases on polystyrene in toluene, Polymer 34(19) (**1993**) 4111–4117. `doi:10.1016/0032-3861(93)90675-Z`.

[26] C. Sehgal, T. J. Yu, R. G. Sutherland, R. E. Verrall, Use of 2,2-diphenyl-1-picrylhydrazyl to investigate the chemical behavior of free radicals induced by ultrasonic cavitation, The Journal of Physical Chemistry 86(15) (**1982**) 2982–2986. `doi:10.1021/j100212a034`.

[27] C. E. H. Bawn, S. F. Mellish, A method of determination of the rate of molecular dissociation in solution, Transactions of the Faraday Society 47 (**1951**) 1216–1227. `doi:10.1039/TF9514701216`.

[28] K. S. Suslick, J. J. Gawienowski, P. F. Schubert, H. H. Wang, Sonochemistry in non-aqueous liquids, Ultrasonics 22(1) (**1984**) 33–36. `doi:10.1016/0041-624X(84)90059-3`.

[29] M. M. van Iersel, J. Cornel, N. E. Benes, J. T. F. Keurentjes, Inhibition of nonlinear acoustic cavitation dynamics in liquid CO_2, Journal of Chemical Physics 126(6) (**2007**) 064508. `doi:10.1063/1.2434962`.

[30] K. Yasui, Alternative model of single-bubble sonoluminescence, Physical Review E: Statistical, Nonlinear, and Soft Matter Physics 56(6) (**1997**) 6750–6760. `doi:10.1103/PhysRevE.56.6750`.

[31] J. B. Keller, M. Miksis, Bubble oscillations of large amplitude, The Journal of the Acoustical Society of America 68(2) (**1980**) 628–633. `doi:10.1121/1.384720`.

[32] J. A. Wesselingh, R. Krishna, Mass transfer in multicomponent mixtures, Delft University Press, Delft, 2000.

[33] U. S. Agarwal, Simulation of bubble growth and collapse in linear and *pom-pom* polymers, e-Polymers 14 (**2002**) 1–15.

[34] T. Nguyen, H.-H. Kausch, Mechanochemical degradation in transient elongational flow, in: Macromolecules: Synthesis, Order and Advanced Properties, Vol. 100 of Advances in Polymer Science, Springer Berlin / Heidelberg, 1992, pp. 73–182.

[35] R. G. Larson, Constitutive Equation for polymer melts and solutions, Butterworths, New York, 1988.

[36] J. M. Evans, M. B. Huglin, Unperturbed dimensions of polytetrahydrofuran, Die Makromolekulare Chemie 127(1) (**1969**) 141–152. `doi:10.1002/macp.1969.021270108`.

[37] K. S. Suslick, W. B. McNamara III, Y. Didenko, Sonochemistry and sonoluminescence, Vol. 524 of NATO ASI Series C: Mathematical and Physical Sciences, Kluwer Academic Publishers, Dordrecht, The Netherlands, 1999, Ch. Hot spot conditions during multi-bubble cavitation, pp. 191–204.

[38] K. S. Suslick, D. A. Hammerton, R. E. Cline, Sonochemical hot spot, Journal of the American Chemical Society 108(18) (**1986**) 5641–5642. `doi:10.1021/ja00278a055`.

[39] Y. T. Didenko, W. B. McNamara III, K. S. Suslick, Effect of noble gases on sonoluminescence temperatures during multibubble cavitation, Physical Review Letters 84(4) (**2000**) 777–780. `doi:10.1103/PhysRevLett.84.777`.

[40] V. Mišík, P. Riesz, Recent applications of EPR and spin trapping to sonochemical studies of organic liquids and aqueous solutions, Ultrasonics Sonochemistry 3(3) (**1996**) S173–S186. `doi:10.1016/S1350-4177(96)00023-5`.

[41] M. Szwarc, The C-H bond energy in toluene and xylenes, Journal of Chemical Physics 16(2) (**1948**) 128–136. `doi:10.1063/1.1746794`.

[42] K. Okitsu, T. Suzuki, N. Takenaka, H. Bandow, R. Nishimura, Y. Maeda, Acoustic multibubble cavitation in water: A new aspect of the effect of a rare gas atmosphere on bubble temperature and its relevance to sonochemistry, Journal of Physical Chemistry B 110(41) (**2006**) 20081–20084. `doi:10.1021/jp064598u`.

[43] M. Wall, M. Ashokkumar, R. Tronson, F. Grieser, Multibubble sonoluminescence in aqueous salt solutions, Ultrasonics Sonochemistry 6(1–2) (**1999**) 7–14. `doi:10.1016/S1350-4177(98)00037-6`.

[44] A. Brotchie, T. Statham, M. Zhou, L. Dharmarathne, F. Grieser, M. Ashokkumar, Acoustic bubble sizes, coalescence, and sonochemical activity in aqueous electrolyte solutions saturated with different gases, Langmuir 26(15) (**2010**) 12690–12695. `doi:10.1021/la1017104`.

[45] W. Schneider, Vapor flow through a porous membrane - a throttling process with condensation and evaporation, Acta Mechanica 47(1) (**1983**) 15–25. `doi:10.1007/BF01176497`.

[46] R. B. Bird, W. E. Stewart, E. N. Lightfoot, Transport Phenomena, 2nd Edition, John Wiley & Sons, Inc., New York, 2002.

[47] The National Institute of Standards and Technology database, http://webbook.nist.gov, as accessed on August 11, 2010.

[48] D. R. Lide, W. M. Haynes, Handbook of chemistry and physics, Vol. 90, CRC Press, Boca Raton,

2009.

[49] C. Wohlfarth, Surface tension of toluene, Vol. 24: Supplement to IV/16 of Landolt-Börnstein - Group IV Physical Chemistry. Numerical Data and Functional Relationships in Science and Technology, Springer-Verlag, Berlin, 2008. `doi:10.1007/978-3-540-75508-1_137`.

[50] F. J. V. Santos, C. A. N. de Castro, J. H. Dymond, N. K. Dalaouti, M. J. Assael, A. Nagashima, Standard reference data for the viscosity of toluene, Journal of Physical and Chemical Reference Data 35(1) (**2006**) 1–8. `doi:10.1063/1.1928233`.

[51] H. Kashiwagi, T. Hashimoto, Y. Tanaka, H. Kubota, T. Makita, Thermal conductivity and density of toluene in the temperature range 273-373 K at pressures up to 250 MPa, International Journal of Thermophysics 3(3) (**1982**) 201–215. `doi:10.1007/BF00503316`.

[52] L. S. Zaitseva, L. V. Yakush, N. A. Vanicheva, Thermal conductivities of benzene and toluene vapors, Journal of Engineering Physics and Thermophysics 31(5) (**1976**) 1292–1295. `doi:10.1007/BF00859307`.

Appendices

Determination of the percentage of catalyst scission from ^{1}H NMR

The ^{1}H NMR spectra of the silver(I)-NHC complex and the corresponding non-complexed imidazolium salt show distinct chemical shifts for both species. In addition, the C_2 proton (between 9-10 ppm) becomes visible in the spectrum of the imidazolium salt, whereas is it obviously absent in the spectrum of the silver(I)-NHC complex. Two typical ^{1}H NMR spectra are shown in Fig. 5.5. The top spectrum is of the free (polymer-functionalised) imidazolium salt, the bottom spectrum is of a partly dissociated polymer catalyst complex. The characteristic peaks for complex and imidazolium salt have been assigned and the percentage of complex scission can be calculated from the ratio between the areas obtained by integration.

The ^{1}H NMR spectra were processed using standard VNMRJ software (Version 2.2 Revision D, by Inova). The integral regions of the individual peaks were calculated by deconvolution of the peaks in the region between 4.2 and 4.5 ppm when necessary. It was not always possible to resolve all individual peaks in multiplets in the deconvolution software. It was assured that the result of the deconvolution procedure was the best possible representation of the original spectrum in all cases.

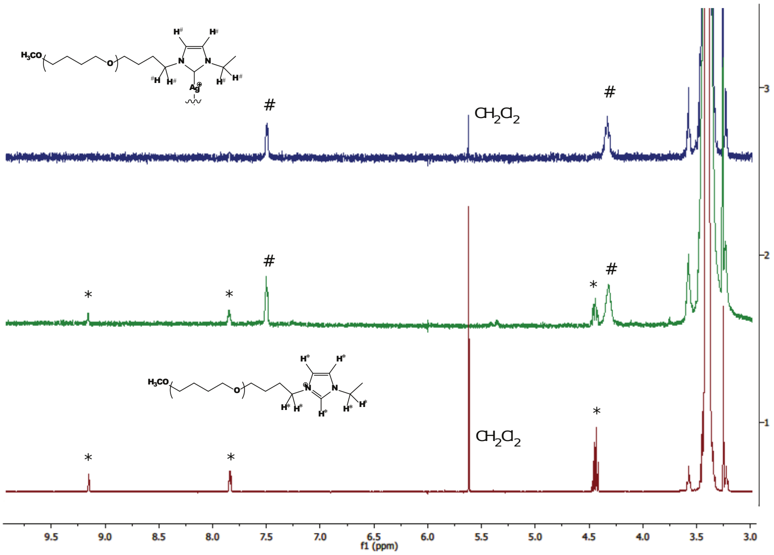

Figure 5.5: Typical NMR spectra of the silver(I)-NHC complex (top) and the corresponding non-complexed imidazolium salt (bottom).

Model equations

$$\rho_l\left(1-\frac{\dot{R}}{c_S}\right)R\ddot{R}+\frac{3}{2}\rho_l\left(1-\frac{\dot{R}}{3c_S}\right)\dot{R}^2=\left(1+\frac{\dot{R}}{c_S}\right)(P_v-P_\infty)+\frac{R}{c_S}\dot{P}_v-\frac{2\sigma}{R}-4\mu\frac{\dot{R}}{R} \quad (5.1)$$

$$\dot{N}_v=4\pi R^2\frac{F_{\text{vap/cond}}}{M_v\sqrt{\frac{2\pi R_g}{M_v}}}\left(\frac{P_{v,i}^{\text{sat}}}{\sqrt{T_{l,i}}}-\frac{P_{v,i}}{\sqrt{T_i}}\right) \quad (5.2)$$

$$\dot{N}_v=\frac{D_gC_b}{\delta_m}\frac{P_{v,i}-P_v}{P_{\text{tot}}-0.5(P_{v,i}+P_v)} \quad (5.3)$$

$$\dot{N}_g=\frac{A_bD_l}{\delta_g}\frac{C_l^{\text{sat}}-C_l}{C_l-0.5(C_l^{\text{sat}}+C_i)} \quad (5.4)$$

$$\dot{Q}-\dot{W}=-h_v\dot{N}_vkN_A-h_g\dot{N}_gkN_A+\frac{d}{dt}(N_gC_{p,g}T+N_vC_{p,v}T) \quad (5.5)$$

$$T_{l,i}=T_i+\frac{1}{2k_BN_a}\sqrt{\frac{\pi M_v}{2kT_i}}\frac{2-FF_{\text{th}}}{F_{\text{th}}}\kappa_b\frac{T_i-T}{\delta_b} \quad (5.6)$$

$$4\pi R^2\kappa_l\frac{T_l-T_{l,i}}{\delta_l}=4\pi R^2\kappa_b\frac{T_l-T}{\delta_b}+\dot{N}_v\left(\Delta H_{\text{vap}}+C_{p,v}\left(T_i-T_{l,i}\right)\right) \quad (5.7)$$

$$\delta_{\text{th},l}=\text{Min}\left(\sqrt{\frac{R\alpha_l\pi}{|\dot{R}|}},\frac{R}{\pi}\right) \quad (5.8)$$

$$\delta_{\text{m},l}=\text{Min}\left(\sqrt{\frac{RD_l\pi}{|\dot{R}|}},\frac{R}{\pi}\right) \quad (5.9)$$

$$\delta_{\text{th},b}=\frac{R}{\pi} \quad (5.10)$$

$$\delta_{\text{m},b}=\frac{R}{\pi} \quad (5.11)$$

See page 117 for the Nomenclature

Pure component properties used in the model

Table 5.2: Argon pure component properties used in the cavitation dynamics model

Property		Relation	Dimension	Ref.
Gas heat conduction	κ_g	$0.009 + 3.2 \times 10^{-5} T_i$	W m^{-1} K^{-1}	[45]
Enthalpy per molecule	h_v	$\frac{3}{2} k_b T$	J mol^{-1}	
Lennard-Jones parameter	ϵ	122.4	K	[46]
Lennard-Jones parameter	σ_m	3.432×10^{-10}	m	[46]
Heat capacity gas	$C_{p,g}$	20.94	J mol^{-1} K^{-1}	[47]

Table 5.3: Nitrogen pure component properties used in the cavitation dynamics model

Property		Relation	Dimension	Ref.
Gas heat conduction	κ_g	$6.7 \times 10^{-5} T_i + 5.7 \times 10^{-3}$	W m^{-1} K^{-1}	[48]
Enthalpy per molecule	h_v	$\frac{3}{2} k_b T$	J mol^{-1}	
Lennard-Jones parameter	ϵ	99.8	K	[46]
Lennard-Jones parameter	σ_m	3.667×10^{-10}	m	[46]
Heat capacity gas	$C_{p,g}$	$-2.08\times10^{-9} T^3 + 5.82 \times 10^{-6} T^2$		
		$+2.25 \times 10^{-4} T + 28.5$	J mol^{-1} K^{-1}	[47]

Table 5.4: Methane pure component properties used in the cavitation dynamics model

Property		Relation	Dimension	Ref.
Gas heat conduction	κ_g	$1.1 \times 10^{-7} T_i^2 + 8.3 \times 10^{-5} T_i$	W m^{-1} K^{-1}	[47]
Enthalpy per molecule	h_v	$\frac{15}{2} k_b T$	J mol^{-1}	
Lennard-Jones parameter	ϵ	154	K	[46]
Lennard-Jones parameter	σ_m	3.78×10^{-10}	m	[46]
Heat capacity gas	$C_{p,g}$	$0.0563 T + 18.466$	J mol^{-1} K^{-1}	[47]

Table 5.5: Isobutane pure component properties used in the cavitation dynamics model

Property		Relation	Dimension	Ref.
Gas heat conduction	κ_g	$1.07\times10^{-4}T_i - 0.0148$	W m^{-1} K^{-1}	[47]
Enthalpy per molecule	h_v	$\frac{39}{2}k_bT$	J.mol^{-1}	
Lennard-Jones parameter	ϵ	295	K	[46]
Lennard-Jones parameter	σ_m	5.393×10^{-10}	m	[46]
Heat capacity gas	$C_{p,g}$	$305.18\left(1 - e^{-1.37\times10^{-3}T}\right)$	J mol^{-1} K^{-1}	[47]

Table 5.6: Toluene pure component properties used in the cavitation dynamics model

Property		Relation	Dimension	Ref.
Surface tension	σ	$-1.12 \times 10^{-4} T_{l,i} + 6.09 \times 10^{-2}$	N m^{-1}	[49]
Speed of sound	C	$3743 e^{-0.0035 T_{l,i}}$	m s^{-1}	[47]
Viscosity	μ	$5.9 \times 10^{-4} e^{-5.22 + \frac{2.67 \times 10^3}{T_{l,i}} - \frac{5.18 \times 10^5}{T_{l,i}^2} + \frac{5.53 \times 10^7}{T_{l,i}^3}}$	Pa s	[50]
Density	ρ	$1248 e^{-0.0012 T_{l,i}}$	kg m^{-3}	[47]
Vapourisation enthalpy	ΔH_{vap}	33000	J mol^{-1}	[47]
Heat conduction (liquid)	κ_l	0.207	W m^{-1} K^{-1}	[51]
Heat conduction (vapour)	κ_v	$1.16 \times 10^{-4} T_{l,i} - 2.77 \times 10^{-2}$	W m^{-1} K^{-1}	[52]
Heat capacity (liquid)	$C_{p,l}$	160.46	J mol^{-1} K^{-1}	[48]
Heat capacity (vapour)	$C_{p,v}$	102	J mol^{-1} K^{-1}	[47]
Enthalpy per molecule	h_v	$\frac{30}{2} k_b T$	J mol^{-1}	
Molecular weight	MW	94	g mol	
Vapour pressure	P^{sat}	$10^{\left(4.54 - \frac{1738.12}{T_{l,i} + 0.394}\right)} \times 10^5$	Pa	[47]
Lennard-Jones parameter	ϵ	387	K	[46]
Lennard-Jones parameter	σ_m	5.44×10^{-10}	m	[46]

6 Hydrodynamic cavitation in micrometer and millimeter sized geometries and measured chemical effect

Decreasing the constriction size and residence time in hydrodynamic cavitation is predicted to give increased hot spot temperatures at bubble collapse and increased radical formation rate. Cavitation in a 100 × 100 μm^2 rectangular micro channel and in a circular 750 μm diameter milli channel has been investigated with computational fluid dynamics software and with imaging and radical production experiments. No radical production has been measured in the micro channel. This is probably because there is no spherically symmetrical collapse of the gas pockets in the channel which yield high hot spot temperatures. The potassium iodide oxidation yield in presence of chlorohydrocarbons in the milli channel of up to 60 nM min^{-1} is comparable to values reported on hydrodynamic cavitation in literature, but lower than values for ultrasonic cavitation. The small constrictions investigated in this work can create high apparent cavitation collapse frequencies.

This Chapter has been published as: J. Rooze, M. André, G.-J. S. van der Gulik, D. Fernández-Rivas, J. G. E. Gardeniers, E. V. Rebrov and J. C. Schouten and J. T. F. Keurentjes, Hydrodynamic cavitation in micro channels with channel sizes of 100 and 750 micrometers, *Microfluidics Nanofluidics* 12(1–4) (**2011**) 499–508

Cavitation is the growth and collapse of a gas bubble in a liquid[1]. The characteristic collapse time is much shorter than the characteristic time for heat transfer. High temperatures and pressures are therefore reached inside the bubble due to compression[2,3]. Estimations for the temperature and pressure during a collapse in ultrasound are generally around several thousand K[4,5] and several hundred bar[6]. Applications of cavitation are *e.g.* making surface modifications[7], creating radical species[8], or mixing liquids[9]. The energy of the collapse is dissipated after the event, and the average liquid temperature stays at ambient values. Common ways to create cavitation are with ultrasound, in a hydrodynamic flow field, and with a focussed laser burst. The pressure in a flow field decreases between a point before a constriction (1) and inside a constriction (2), and is described by Bernoulli's equation:

$$p_1 - p_2 = \frac{1}{2}\rho\left(v_2^2 - v_1^2\right) \tag{6.1}$$

where p is the pressure, ρ is the liquid density, and v is the liquid velocity. A cavitation bubble is generated when the pressure decreases to a sufficiently low value to generate growth of an existing gas pocket in the liquid.

The dimensionless cavitation number (CN) is often used to characterise cavitation:

$$\mathrm{CN} = \frac{p_{\mathrm{ref}} - p_v}{\frac{1}{2}\rho v_c^2} \tag{6.2}$$

where $\dot{R}$ is the time derivative of the bubble radius, p_{ref} is the reference pressure, often the downstream pressure, p_v is the liquid vapour pressure, and v_c is the liquid velocity inside the constriction. The CN is the ratio between the static pressure and the pressure drop due to the flow through the constriction. Theoretically, the liquid velocity is sufficient to start forming vapour at a CN of below 1. Nuclei already present in the liquid can grow under these conditions. However, the experimental CN value at inception depends on constriction size and geometry. Cavitation starts at a CN of 1 – 7 in constrictions with diameters of 1.5 – 3 cm in a 3.8 cm diameter pipe[10]. It starts at a CN of 0.1 – 0.5 in 10 × 100 to 40 × 100 $\mu\mathrm{m}^2$ constrictions in 100 × 100 $\mu\mathrm{m}^2$ channels[11,12]. Since the CN is not consistent for different geometries, pressures and velocities have been provided instead in this article when known.

Ultrasound-induced cavitation is regarded as the most energy efficient process for radical formation[13–15]. Ultrasonic cavitation at 850 kHz has a 14 times higher breakdown efficiency of aromatic compounds than hydrodynamic cavitation[14]. However, several authors report that hydrodynamic cavitation (HC) has a higher energy efficiency[16–18]. These studies use ultrasonic cavitation processes at ultrasound frequencies around 20 kHz, whereas the optimum radical production frequency is found around 300 kHz[19,20].

Decreasing the constriction diameter in hydrodynamic cavitation is desirable because this decreases pressure recovery time and increases the intensity of the cavitation bubble collapse. This results in increased temperatures and radical formation rates[21–23]. Micro fabrication technology offers high precision manufacturing of channels with dimensions in the micrometer range. These channels are easily studied and have small constrictions compared to previous and recent work in hydrodynamic cavitation[16,22]. It has been shown that by a miniaturization strategy in sonochemical reactors it is possible to study complex phenomena such as microbubble nucleation and improve operation efficiency[24]. The relatively smooth silicon surfaces used there allowed the control of certain cavitation conditions.

In this work, cavitation in constrictions with an area of 20 × 100 μm^2 in channels of 100 × 100 μm^2 and constrictions of 100 – 300 μm diameter in tubes with a diameter of 750 μm has been investigated. Cavitation behaviour at various flow rates has been studied in channels at both size scales. Pressure gradients and void fractions in the fluid have been obtained by Computational Fluid Dynamics (CFD) modelling. These pressure gradients have been used to calculate the temperature of a bubble collapse using the Rayleigh-Plesset equation. Apparent frequencies for bubbles travelling through constrictions with a 200 μm diameter are of the same order of magnitude as frequencies in ultrasonic cavitation for the milli channel (160 kHz). Estimations of the collapse temperature are compared with results on an oxidation reaction carried out by cavitation in the milli channel. This is the first time that radical production rate measurements of hydrodynamic cavitation at these length scales are carried out according to our knowledge.

6.1 Experimental

6.1.1 Micro channel experiments

The micro channel design was similar to that of Mishra and Peles[25], see Fig. 6.1. The channel and pressure ports geometry were etched on the top side of the double side polished silicon wafers n-type {100} using a deep reactive ion etching process. The pressure port openings, and the inlet and outlet ports were machined on the back side. The top wafer was made of borofloat glass to allow visual inspection. The channel width and depth was 100 μm, and its total length was was 1 cm. The constriction width and length was 20 μm, and 10 μm, respectively. A liquid flow rate of 0.5 – 6.5 mL min^{-1} was created with a JASCO PU 2086 Plus pump with a filter with 1 μm pores between the pump and the micro channel. The pressure was measured relative to the atmospheric pressure at 460 μm downstream of the constriction using a calibrated Sensortechnics sensor, 24PC series 0 – 16 bar. An Olympus IX-71 microscope with an Olympus UplanFLN 10× lens and a Redlake X4 high speed camera was used for visualisation, using a Nikon SB900 flash light at full flash length as an illumination source. The exposure time was 1 μs for one frame. MilliQ water was used in visualisation studies. MilliQ water (20 mL) containing 0.1 M KI (p.a., Merck) and saturated with CH_2Cl_2 (p.a., Sigma-Aldrich) was used in radical production experiments. The chloroalkane was added to increase the radical production[26]. Saturation with argon was done during 30 minutes prior to the experiment. The solution was kept under argon atmosphere during the experiment. The production of I_3^- was measured at the experiment start, and after 60 minutes using a Shimadzu 2501-PC UV spectrometer operated at 350 nm. The I_3^- concentration was calculated using a spectroscopic extinction coefficient of 26.4×10^3 L mol^{-1} cm^{-1}[27].

a) b)

Figure 6.1: Schematic top view representation of the channel layout, a) entire channel, b) magnification of the constriction. The main channel with the constriction is in the center (dark colour). The diagonal channels (light colour) are connected to pressure sensors or dead ends.

6.1.2 Milli channel experiments

A poly(ether ether ketone) (PEEK) capillary with an internal diameter of 750 μm was inserted in a poly(methyl methacrylate) (PMMA) holder with a constriction of either 110 or 180 μm diameter in visualisation studies (see Fig. 6.2). The transparent PMMA holders with a constriction allow visual inspection inside the constriction. The PMMA constrictions were slightly skewed due to the machining process, the diameters mentioned were measured at the constriction exit. Visualisation was done using a Redlake X4 high speed camera, a Nikon AF micro Nikkor 60 mm lens, and a Dedocool CoolT3 250 W lamp as an illumination source. The exposure time was 1 μs for one frame. The exit stream enters a $8 \times 4 \times 5.2$ mm^3 chamber machined in PEEK with two transparent quartz plates on the top and bottom. A 7 – 80 mL min^{-1} (v_c 5 – 59 m s^{-1}) liquid flow was created by a Gilson 305 HPLC pump with a 0 – 100 mL min^{-1} capacity. The pressure was measured relative to atmospheric pressure at 2.8 cm downstream of the constriction using a calibrated Sensortechnics 24PC series 0 – 16 bar sensor. MilliQ water was used in visualisation studies. PEEK holders with straight 100, 200, and 300 μm diameter constrictions were used in radical production experiments. The solution was kept at 20 ±1°C using a Lauda E300 thermostat. KI solution (20 mL 0.1 M, p.a.,

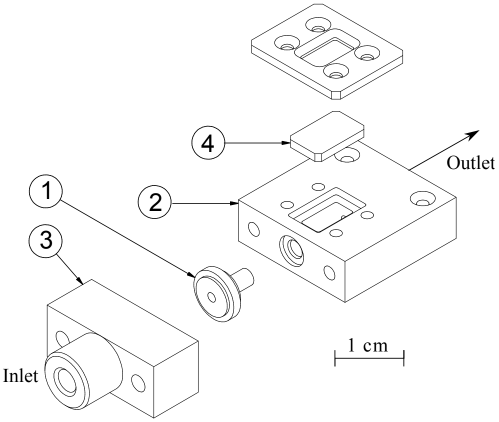

Figure 6.2: Schematic drawing of the milli channel assembly. A holder with the constriction is machined in PMMA or PEEK (1). The rest of the assembly is manufactured in PEEK. The holder is inserted into the chamber (2), and fixed using a second block (3) which contains the inlet port. The top and bottom of the chamber are made of transparent quartz plates (4) for illumination.

Merck) saturated with $CHCl_3$ (p.a., Aldrich) was saturated with argon for 30 minutes prior to the experiment, and was kept under argon atmosphere during the experiment. The production of I_3^- was measured every 5 minutes. The power input into the liquid was between 2 and 14 W depending on the flow rate, measured by calorimetry.

6.2 Modelling

6.2.1 CFD modelling with simplified Rayleigh-Plesset model

All channel geometries have been modelled and meshed with ICEM Hexa release 11.0.1 software. They have been spatially discretised using a structured hexa mesh (see Table 6.1). Only a quarter of the channel has been modelled due to the presence of two symmetry planes. Several refinements have been modelled in order to evaluate the grid dependency. The channels have a refined mesh in the constriction (see Fig. 6.3) because most vapour is formed in the constriction.

The steady state flow field has been obtained using the CFD software ANSYS CFX release 11.0. This software solves the time averaged Reynolds Averaged Navier Stokes equations (RANS) for a Newtonian fluid. The closure of the equation system has been realised with a Shear Stress Transport (SST) turbulence model with an automatic near-wall treatment[28]. The cavitation model is a homogeneous interphase mass transfer model derived from a first order simplification of the Rayleigh-Plesset equation (Also see Eq. 6.7). It describes the radial dynamics of vapour bubbles of uniform size. The bubble nuclei are assumed

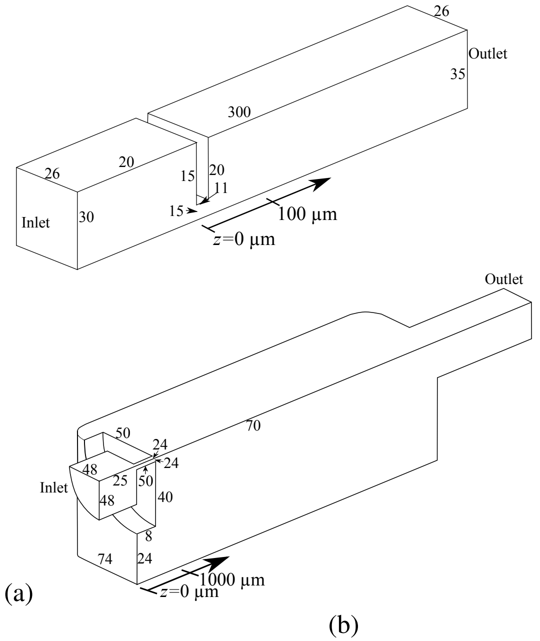

Figure 6.3: Quarter mesh geometries of a) the micro channel (symmetry plane at the bottom and right of the image) and b) the milli channel (symmetry planes at the top and right of the image). The number of nodes for each boundary are indicated in the image.

Table 6.1: Relevant geometry and mesh details used in CFD modelling of the hydrodynamic cavitation devices.

Geometry	Nodes (× 1000)	Max. aspect ratio
Micro channel	284	11.5
Milli channel	534	29

to be homogeneously distributed in the liquid. A threshold pressure for cavitation is added to match the pressure drop found in experiments and literature[11].

$$\dot{R} = \sqrt{\frac{2}{3}\frac{p_v - p[t]}{\rho_l}}\operatorname{sgn}\left(p_{\text{thresh}} - p[t]\right) \tag{6.3}$$

$$\operatorname{sgn}(x) = \begin{cases} 0, x < 0 \\ 1, x \geq 0 \end{cases} \tag{6.4}$$

where p_v is the vapour pressure, $p[t]$ is the pressure as a function of time, ρ_l is the liquid density, p_{thresh} is the threshold pressure for growth of the cavitation bubbles. Average vapour fractions are calculated from the total bubble volume. Vaporisation and condensation rates at the bubble interface were described using:

$$\dot{m}_{\text{vap}} = 3F_{\text{vap}}\epsilon_0(1-\epsilon)\rho_g\frac{\dot{R}}{R} \tag{6.5}$$

$$\dot{m}_{\text{cond}} = 3F_{\text{cond}}\epsilon\rho_g\frac{\dot{R}}{R} \tag{6.6}$$

where $\dot{m}$ is the mass accumulation in time, and where the empirical factors F_{cond} and F_{vap} and the initial void fraction ϵ_0 shown in Table 6.2 were used. The value of p_{thresh} was chosen to match the Blake threshold criterion[1] for bubbles with an initial radius R_0 of 1 µm. The mass, momentum, and void fraction equations were solved in a coupled manner in order to improve convergence. RMS values for mass and momentum were well below $1{\times}10^{-4}$ and imbalances below 1%.

These equations omitted second order terms in the Rayleigh-Plesset equation. Therefore, a full Rayleigh-Plesset description was solved separately using the pressure gradients obtained from the CFD calculations as an input[29].

Table 6.2: Empirical factors used in the CFD modelling.

Parameter	Value	Dimension
F_{cond}	0.01	–
F_{vap}	50	–
ϵ_0	5×10^{-4}	–
R_0	1×10^{-6}	m
p_{thresh}	-0.75	bar

6.2.2 Full Rayleigh-Plesset model

The radius R, pressure p, and temperature T of an oscillating bubble under influence of a pressure field in a Newtonian fluid has been modeled with a Rayleigh-Plesset equation[5].

$$\rho_l\left(R\ddot{R}+\frac{3}{2}\dot{R}^2\right) = p_g - p[t] - p_0 + \frac{R}{c_l}\dot{p}_g - 4\eta_l\frac{\dot{R}}{R} - \frac{2\sigma}{R} \quad (6.7)$$

$$\dot{p}_g = -\gamma(\mathrm{Pe})\frac{3R^2\dot{R}}{R^3-h^3}p_g \quad (6.8)$$

$$\dot{T} = -\left(\gamma(\mathrm{Pe})-1\right)\frac{3R^2\dot{R}}{R^3-h^3}T - \alpha_g\frac{T-T_0}{R^2} \quad (6.9)$$

The Péclet number, Pe, is defined as $\frac{R|\dot{R}|}{\alpha_g}$, c_l is the speed of sound in the liquid, η_l is the liquid viscosity, σ is the liquid surface tension, and h is the minimum bubble radius, $R_0/8.84$ for argon[30], all parameters at 298 K. The adiabatic factor γ is dependent upon the Péclet number:

$$\gamma(\mathrm{Pe}) = 1 + (\gamma_0 - 1)\exp\left(\frac{-5.8}{\mathrm{Pe}^{0.6}}\right) \quad (6.10)$$

Where γ_0 is the initial adiabatic factor. For the relevant physical quantities see Table 6.3 This model assumes spherical symmetry of the bubbles during their lifetime. This assumption does not hold for most bubbles in a vapour cloud created by hydrodynamic cavitation. Furthermore, there are no equations for vapour mass transport near the bubble wall. An increased amount of vapour decreases the hot spot temperature, and the hot spot temperatures obtained in experiments are therefore lower. The model is therefore only useful for qualitative comparisons.

Table 6.3: Physical quantities of argon and water used in the Rayleigh-Plesset model.

Parameter	Value	Dimension
γ_0(Ar)	1.67	–
c_l	1500	m s^{-1}
η_l	8.9×10^{-4}	Pa s
σ	0.072	N m^{-1}
R_0	5×10^{-6}	m
α_g	2.2×10^{-5}	m^2 s^{-1}

6.3 Results and discussion

6.3.1 Micro channel

A pressure drop of 13 bar over the micro channel constriction is obtained in CFD calculations at a flow rate of 4 mL min^{-1}. The formation of a vapour phase in the constriction and downstream is shown in Fig. 6.4 (b). The model shows a quick transition between a vapour volume fraction below 0.2 downstream at flow rates below 3 mL min^{-1} and cavities with a vapour fraction above 0.8 at flow rates above 3 mL min^{-1} (v_c 25 m s^{-1}). This behaviour is linked with the low pressure region extending from the constriction to the channel downstream of the constriction at these flow rates.

The experimental results obtained by Mishra and Peles in micro channels[11,25,31] have been reproduced in a set-up without downstream pressure control. The measurements described in this paper are all performed in the developed cavitation regime. A typical image of hydrodynamic cavitation is shown in Fig. 6.4 (c). A gas phase is formed near the constriction, and the liquid leaves the constriction as a jet which is accompanied by a recirculation loop. The regions with the gas-liquid mixture, visible as dark areas in the images, becomes longer as flow rate increases. The gas phase disappears after a length of several channel diameters at a position depending on the flow rate. Just after the constriction a stable gas pocket is observed. Spherical oscillation and collapse of gas bubbles is not apparent in the images.

The calculated downstream pressure at the pressure port is 0.15 bar, which is in reasonable agreement with the experimental value of 0.5 bar. There is a long pressure recovery region of 625 µm behind the constriction, and this induces an excessive growth of the bubbles. The calculated void fraction profile qualitatively agrees with the experimental one. CFD calculations describe non-local phenomena such as the jet and average void fraction fairly well. The local phenomena such as the turbulent collapse of the vapour are not modelled in this approach with symmetry planes and steady state.

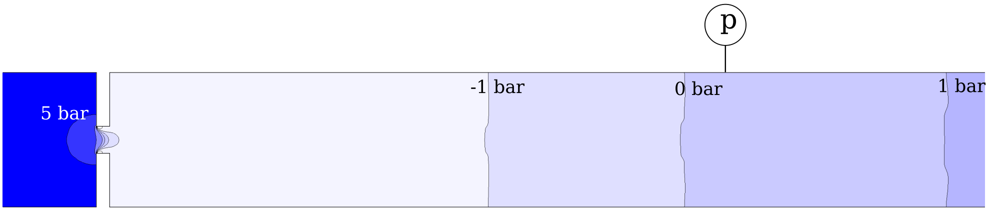

(a) CFD solver pressure profile calculation, micro channel

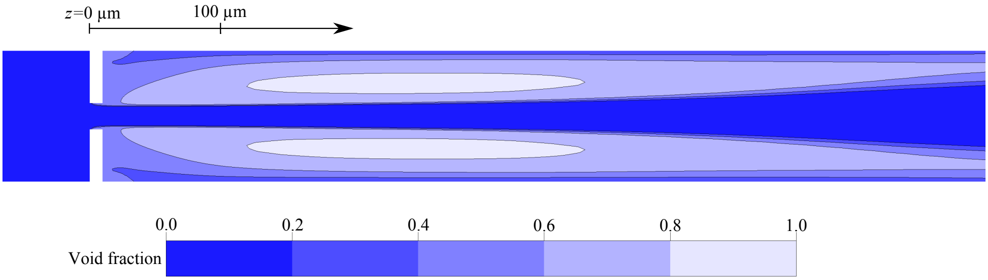

(b) CFD void fraction calculation, micro channel

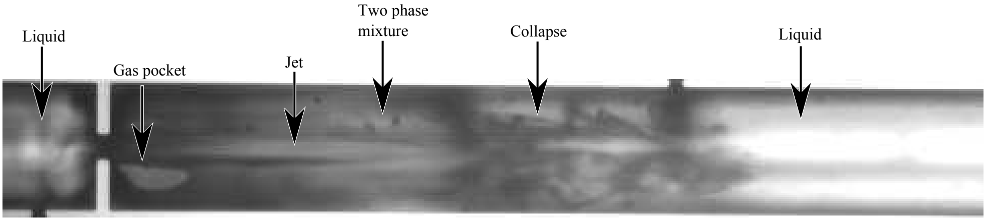

(c) Experimental image, micro channel top view

Figure 6.4: Top view of the CFD simulation results solver pressure (a) and void fraction (b) and top view of an experimental image of cavitation (c) in a micro channel with a 20×10 µm width and length constriction. A symmetry plane is present in the channel centre, the entire channel is reconstructed using this symmetry plane. Temperature = 25 °C, Flow = 4 mL min^{-1} (from left to right, v_c = 33 m s^{-1}). The solver pressure drops from 10.8 bar upstream to -2 bar downstream, and increases to the ambient pressure of 1 bar close to the channel exit. A liquid jet in the channel centre, accompanied by a large region with a void fraction of over 0.6 is found downstream of the constriction. The minimum solver pressure of -4.4 bar is found near the beginning of the constriction and near the wall.
The experimental image shows a liquid jet originating from the constriction. The pressure upstream is 8.9 bar, the pressure at the pressure port is 0.5 bar. A semi-cylindrical vapour pocket which fills the channel from top to bottom is visible just after the constriction. A dark region probably formed by vapour nuclei of sufficient size for discoloration is visible. After about 300 µm the cavities break up and disappear. There is no flow through the pressure port.

Excessive vapour formation occurs at the channel walls with liquid pressures close to the vapour pressure in case a surface nucleation term is included in the model. This does not match experimental observations and therefore the surface nucleation term has not been used in further calculations. The residence time and pressures obtained inside the constriction are sufficient to obtain growth of the nuclei. The surface tension delays the cavitation of a filtered liquid because growth of smaller bubbles needs a larger force than that of larger bubbles. Surface tension is not included in the cavitation model but its effect on the vapour formation can be approximated by lowering the pressure threshold for cavitation in Equation 6.3.

No measurable conversion has been observed in potassium iodide oxidation in the micro channel. Either there is no collapse with a hot spot, or the reaction is not sensitive enough to quantify the radical production. The bubble growth is excessive, filling the entire channel at some places. This prevents spherical collapse and high hot spot temperatures. Calculations with the full Rayleigh-Plesset model yield maximum bubble sizes which exceed the channel dimensions and are not suitable to estimate hot spot temperatures. Further experiments have therefore been carried out in a milli channel.

6.3.2 Milli channel

A ring of vapour is formed near the wall of the constriction as predicted by CFD calculations in the milli channel. Afterwards the vapour is released into the chamber. The vapour volume fraction downstream of the constriction remains below 0.2 so no excessive bubble growth is expected in the chamber at any flow rate studied. The pressure recovery takes place inside the constriction which differs from microscale where the pressure recovery is observed downstream of the constriction (see Fig. 6.6(a) for examples).

The creation of bubbles has been observed in the milli channel at relatively low flow rates of 7 mL min^{-1} (v_c 12 m s^{-1}) in the 110 µm PMMA constriction with p_{DS} = 1.1 bar, and a flow rate of 14 mL min^{-1} (v_c 9 m s^{-1}) in the 180 µm PMMA constriction with p_{DS}=1.3 bar. The shape of the vapour pockets is similar at all flow rates measured. Fig. 6.5 (b) shows a typical image of cavitation at a flow rate of 60 mL min^{-1} (v_c 39 m s^{-1}). Long gas pockets that extend over the entire length of the constriction are formed in the beginning of the constriction. These gas pockets are transparent and stable over time. The two-phase flow in the chamber forms a dark mist flow at flow rates around 30 mL min^{-1} (v_c 20 m s^{-1}, not shown. A mist flow is visible in Fig. 6.5 (b) on the right side of the image). The mist flow likely comes from the many small nuclei that have grown to visible size in and just after the constriction. The many bubbles are observed as a mist because either the bubbles are too small for the resolution of the optics, because not all bubbles are in camera focus, because the light is shielded by the entire cloud of bubbles, due to motion blur, or a combination of these factors. The onset of cavitation can be seen in Fig. 6.5 (b), where the stable transparent gas pockets collapse in a turbulent region. Bubbles are ejected from the constriction at low flow rates in Fig. 6.5 (c) The features of the two-phase flow are not sharp, either due to motion blur or due to the size of the gas pockets, which may be too small to be resolved with the used set-up. A sharp crackling sound which is connected with the cavitation collapse has been detected at all flow rates mentioned. Visual confirmation of bubble oscillation has not been obtained due to the high flow velocities in the experiments.

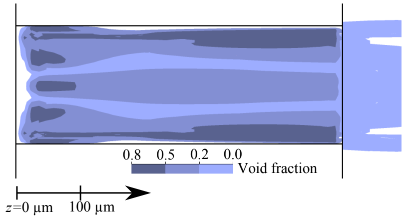

(a) CFD milli channel neck with a flow rate of 90 mL min^{-1} (v_c 59 m s^{-1})

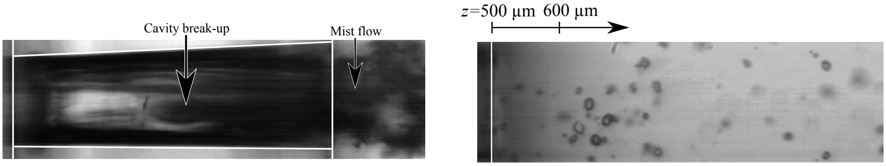

(b) Milli channel neck with a flow rate of 60 mL min^{-1} (v_c 39 m s^{-1})

(c) Milli channel chamber with a flow rate of 20 mL min^{-1} (v_c 13 m s^{-1})

Figure 6.5: Comparison of CFD simulation results of void fraction (a) and experimental image (b) of cavitation in a milli channel with a 180 µm diameter constriction at a flow rate of 60 mL min^{-1}, and an image of the chamber (c) at a flow rate of 20 mL min^{-1} . Vapour formation takes place near the walls in the CFD calculation and reaches vapour fractions of 0.8. A liquid jet with lower vapour fractions is present in the centre of the constriction. The experimental pressure downstream is 3.1 bar (b), and 1.5 bar (c). The constriction walls are outlined by white lines. Long straight vapour pockets are formed in the beginning of the constriction (b). Turbulent break-up of the vapour pockets takes places inside the constriction in this image (indicated with an arrow). Bubbly flow is created at a flow rate of 20 mL min^{-1} (c).

The predicted ring of vapour inside the constriction is observed experimentally in Fig. 6.5 (b). The distinction between the experimental hydrodynamics of two-phase flow - whether a bubbly flow, or a mist flow is formed - can not be made from the CFD calculations. This is because the model does not consider single bubble interfaces, break-up and coalescence, but volume fractions as continuous variables. The characteristics of the collapse such as the hot spot temperature can not be directly calculated from the CFD calculations as a result. Therefore the full Rayleigh-Plesset equations 6.7 – 6.9 have been solved for a bubble

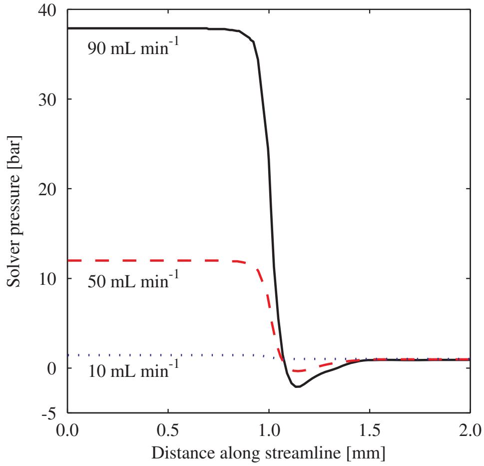

(a)

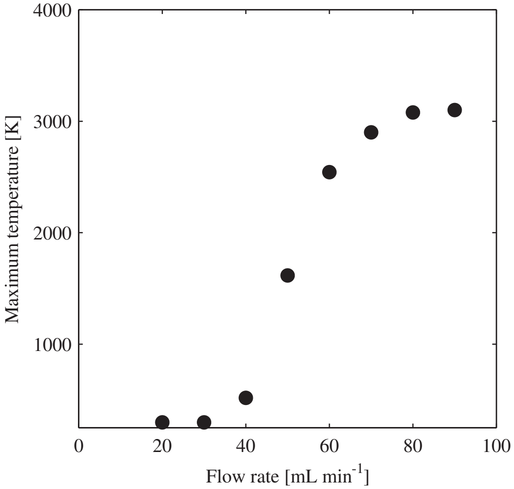

(b)

Figure 6.6: Pressure gradients (a) and the temperature obtained by a Rayleigh-Plesset calculation (b) in the milli channel with the 180 µm constriction. A gas bubble with initial radius of 5 µm traveling near the pressure minimum at flow rates of 10 – 90 mL min^{-1} (v_c 7 – 59 m s^{-1}). The pressure drop from the beginning to the end of the channel is higher at higher flow rates, and ranges from 0.5 – 37 bar (a). The constriction is marked by the sharp decrease in solver pressure, it reaches values as low as -2.1 bar, where the higher flow rates reach the lowest pressures. There is a quick recovery of the solver pressure to atmospheric values behind the pressure minimum. Progressively higher collapse temperatures are obtained at increasing flow rates (b) with a maximum of 3100 K at a flow rate of 90 mL min^{-1}. The collapse is linear and almost isothermal at a flow rate of 30 mL min^{-1}.

travelling along a streamline to estimate the maximum temperature from the corresponding pressure gradients. The higher the temperature, the more radicals can be formed. An accurate description of the vapour formation is needed to obtain accurate pressure profiles.

In Fig. 6.6 the maximum temperature obtained by a bubble traveling along a pressure profile in a 180 µm constriction is reported. The highest temperatures are obtained at the highest flow rate of 90 mL min^{-1} (v_c 59 m s^{-1}). This corresponds to the largest pressure drop of 40 bar (from 38 to -2 bar). The first nonlinear collapse yields a temperature of 3530 K. This temperature is high enough for dissociation of chemical bonds in $CHCl_3$ [32]. Calculations using equations 6.7 – 6.10, a sinusoidal sound field with an amplitude of 1.3 bar at a frequency of 20 kHz, and an initial bubble radius of 5 µm yield a maximum temperature of 5000 K. The pressure drop at a flow rate of 30 mL min^{-1} (v_c 20 m s^{-1}) is 4.2 bar (from 4.8 to 0.6 bar), which is not sufficient to induce a nonlinear growth and collapse in a nucleus at any size investigated here. The hot spot temperatures obtained in the experiments are lower than those calculated for the single bubble travelling along the channel. This is because the presence of other bubbles distorts the sphericity of the bubble during collapse, thereby decreasing the hot spot temperature.

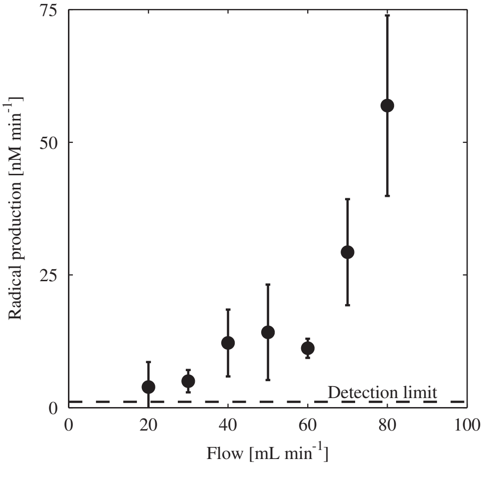

Figure 6.7: Potassium iodide oxidation measurements in the milli channel using the 200 µm diameter PEEK constriction at varying flow rates. A radical production of 4 – 60 nM min^{-1} is observed for flow rates of 20 – 80 mL min^{-1} (v_c 13 – 52 m s^{-1}) and a volume of 50 mL. Error bars indicate one standard deviation. The detection limit is defined as three times the standard deviation of the noise of a blank measurement and is 1.1 nM min^{-1}.

Radical production rates of up to 60 nM min^{-1} have been measured in the milli channel with a 200 µm diameter constriction. Radical production increased with increasing flow rates. The 100 µm diameter constriction yields a potassium iodide oxidation rate of 4 – 10

± 6 nM min^{-1} at flow rates between 25 and 35 mL min^{-1} (v_c 44 – 61 m s^{-1}). No radical formation has been measured in the 300 µm constriction at flow rates up to 100 mL min^{-1} (v_c 23 m s^{-1}). The maximum yield per unit energy of 5 × 10^{-11} mol J^{-1} at a flow rate of 80 mL min^{-1} (v_c 52 m s^{-1}) in the 200 µm constriction is in the same range as oxidation rates measured in other hydrodynamic cavitation experiments for this reaction, 3 × 10^{-13} – 8 × 10^{-11} mol J^{-1} [16], with energy measurements by calorimetry. The calculated values in Fig. 6.6 match the experimental results in Fig. 6.7 only qualitatively. At increasing flow rate an increasing temperature is calculated and an increasing radical formation is measured. On the other hand, there is only a 22 K (0.7 %) difference in temperature between the flow rates of 70 and 80 mL min^{-1} in the calculations, but a 94 % difference in the potassium iodide oxidation measurements, which is not accounted for by an increase of only 12.5 % in number of passes through the constriction at 90 mL min^{-1} as compared to 80 mL min^{-1}.

The residence time inside the 200 µm constriction is 6.3 µs. This corresponds to an apparent frequency of the pressure field of 160 kHz, a value comparable to ultrasonic cavitation frequencies. It is therefore likely that discrepancies between hydrodynamic cavitation and ultrasonic cavitation are not created by a difference in frequency[21] but by the difference in the pressure profiles perceived by the cavitation bubble. The pressure profiles are mainly governed by channel geometry and cloud formation. Also other factors in hydrodynamic cavitation, such as for example the turbulent break up of the vapour phase, may also affect the total oxidation yield[33]. A higher radical production is expected in less constrained environments than the milli chamber, such as orifice plates with micro constrictions.

The cavitation numbers are presented in Table 6.4. They depend on the somewhat arbitrary choice of the reference pressure p_{ref}. The downstream pressure is often used as reference pressure. Cavitation inception is visually detected and is therefore arbitrarily determined. Very small or fast gas pockets may not be detected. The definition of cavitation inception is also inconsistent with the current understanding on how cavitation is initiated. Nuclei are present in the liquid and stabilised by either *e.g.* wall roughness, dust particles, or other impurities[34]. Cavitation is therefore a continuous rather than an instantaneous process. The liquid is filtered to prevent channel blocking in case of experiments with the micro channel. This has an impact on the distribution of nuclei in the liquid. The large distance of the pressure measurement from the constriction in the milli channel (z = 2.8 cm) and the surface roughness of the PMMA constrictions may cause an artificially high CN in these experiments. The reason that size scale effects emerge is caused by lumping the influence of velocity and reference pressure into the CN. The use of the CN as a defining parameter for cavitation is inconvenient when different geometries are compared.

Hybrid geometries with precisely manufactured micro constrictions with an unconfined exit offer opportunities to create high apparent frequencies and high radical production rates.

Table 6.4: Overview of experimental conditions in the cavitation visualisation experiments in the micro and milli channels, with minimum and maximum values obtained.

$d_h^\dagger$ µm		Flow rate mL min^{-1}	v_c m s^{-1}	p_{DS} bar	CN -	Re_c -
33	min	3.0	25	0.5 ‡	0.15	725
	max	6.5	54	0.5 ‡	0.033	1566
110	min	7	12	1.1 *	1.5	1320
	max	35	61	2.0 *	0.11	6710
180	min	14	9	1.1 *	7.6	2520
	max	90	59	3.1 *	0.18	10980

† Hydraulic diameter
‡ measured at z = 460 µm
* measured at z = 2.8 cm

Also the study of plates with multiple constrictions is of interest since these can also give a higher radical production rate.

6.4 Conclusions

Void fraction distributions and pressure gradients in a hydrodynamically cavitating flow in a micro channel and milli channels have been modelled using CFD. Visualisation experiments yield a qualitative agreement with the void fractions obtained in CFD simulations in both size scales. A liquid jet and gas-liquid mixtures are visible in the micro channel, and formation of a bubbly flow or a mist flow in milli channels. The pressure profiles obtained from the CFD calculations have been used to give an estimation of the maximum gas temperature during the collapse using a full Rayleigh-Plesset cavitation model. A maximum temperature estimate of 3100 K at the maximum flow rate of 90 mL min^{-1} (v_c 59 m s^{-1}) has been obtained. The real temperature obtained in the experiments is probably lower due to unsymmetrical collapse of the gas bubbles. An oxidation rate of potassium iodide in the presence of chloroform of up to 60 nM min^{-1} has been measured in the 180 µm diameter milli channel.

Bibliography

[1] T. G. Leighton, The acoustic bubble, Academic Press, London, 1994.

[2] Y. T. Didenko, K. S. Suslick, The energy efficiency of formation of photons, radicals and ions during single-bubble cavitation, Nature 418(6896) (**2002**) 394–397. `doi:10.1038/nature00895`.

[3] J. Rae, M. Ashokkumar, O. Eulaerts, C. von Sonntag, J. Reisse, F. Grieser, Estimation of ultrasound induced cavitation bubble temperatures in aqueous solutions, Ultrasonics Sonochemistry 12(5) (**2005**) 325–329. `doi:10.1016/j.ultsonch.2004.06.007`.

[4] W. B. McNamara III, Y. T. Didenko, K. S. Suslick, Sonoluminescence temperatures during multi-bubble cavitation, Nature 401(6755) (**1999**) 772–775. `doi:10.1038/44536`.

[5] S. Hilgenfeldt, S. Grossmann, D. Lohse, Sonoluminescence light emission, Physics of Fluids 11(6) (**1999**) 1318–1330. `doi:10.1063/1.869997`.

[6] V. Kamath, A. Prosperetti, F. N. Egolfopoulos, A theoretical study of sonoluminescence, The Journal of the Acoustical Society of America 94(1) (**1993**) 248–260. `doi:10.1121/1.407083`.

[7] K. S. Suslick, G. J. Price, Applications of ultrasound to materials chemistry, Annual Review of Materials Science 29(1) (**1999**) 295–326. `doi:10.1146/annurev.matsci.29.1.295`.

[8] T. J. Mason, Sonochemistry: the uses of ultrasound in chemistry, Royal Society of Chemistry Cambridge, 1990.

[9] P. Marmottant, M. Versluis, N. de Jong, S. Hilgenfeldt, D. Lohse, High-speed imaging of an ultrasound-driven bubble in contact with a wall: "Narcissus" effect and resolved acoustic streaming, Experiments in Fluids 41 (**2006**) 147–153. `doi:10.1007/s00348-005-0080-y`.

[10] Y. Yan, R. B. Thorpe, Flow regime transitions due to cavitation in the flow through an orifice, International Journal of Multiphase Flow 16(6) (**1990**) 1023–1045. `doi:10.1016/0301-9322(90)90105-R`.

[11] C. Mishra, Y. Peles, Size scale effects on cavitating flows through microorifices entrenched in rectangular microchannels, Journal of Microelectromechanical Systems 14(5) (**2005**) 987–999. `doi:10.1109/JMEMS.2005.851800`.

[12] R. Singh, Y. Peles, The effects of fluid properties on cavitation in a micro domain, Journal of Micromechanics and Microengineering 19(2) (**2009**) 025009. `doi:10.1088/0960-1317/19/2/025009`.

[13] K. S. Suslick, M. M. Mdleleni, J. T. Ries, Chemistry induced by hydrodynamic cavitation, Journal of the American Chemical Society 119(39) (**1997**) 9303–9304. `doi:10.1021/ja972171i`.

[14] P. Braeutigam, Z.-L. Wu, A. Stark, B. Ondruschka, Degradation of BTEX in aqueous solution by hydrodynamic cavitation, Chemical Engineering & Technology 32(5) (**2009**) 745–753.

[15] M. Franke, P. Braeutigam, Z.-L. Wu, Y. Ren, B. Ondruschka, Enhancement of chloroform degradation by the combination of hydrodynamic and acoustic cavitation, Ultrasonics Sonochemistry 18(4) (**2010**) 888–894. `doi:10.1016/j.ultsonch.2010.11.011`.

[16] P. R. Gogate, I. Z. Shirgaonkar, M. Sivakumar, P. Senthilkumar, N. P. Vichare, A. B. Pandit, Cavitation reactors: Efficiency assessment using a model reaction, AIChE Journal 47(11) (**2001**) 2526–2538. `doi:10.1002/aic.690471115`.

[17] P. R. Gogate, Hydrodynamic cavitation for food and water processing, Food and Bioprocess Technology 3 (**2010**) 1–16. `doi:10.1007/s11947-010-0418-1`.

[18] K. M. Kalamuck, G. L. Chahine, The use of cavitating jets to oxidize organic compounds in water, Journal of Fluids Engineering 122 (**2000**) 465–470. `doi:10.1115/1.1286993`.

[19] D. G. Wayment, D. J. Casadonte Jr., Design and calibration of a single-transducer variable-frequency sonication system, Ultrasonics Sonochemistry 9(4) (**2002**) 189–195. `doi:10.1016/S1350-4177(01)00127-4`.

[20] M. A. Beckett, I. Hua, Impact of ultrasonic frequency on aqueous sonoluminescence and sonochemistry, The Journal of Physical Chemistry 105 (**2001**) 3796–3802. `doi:10.1021/jp003226x`.

[21] S. Arrojo, Y. Benito, A theoretical study of hydrodynamic cavitation, Ultrasonics Sonochemistry 15(3) (**2008**) 203–211. `doi:10.1016/j.ultsonch.2007.03.007`.

[22] P. Braeutigam, M. Franke, Z.-L. Wu, B. Ondruschka, Role of different parameters in the optimization of hydrodynamic cavitation, Chemical Engineering & Technology 33(6) (**2010**) 932–940.

[23] L. P. Amin, P. R. Gogate, A. E. Burgess, D. H. Bremner, Optimization of a hydrodynamic cavita-

tion reactor using salicylic acid dosimetry, Chemical Engineering Journal 156(1) (**2010**) 165–169. `doi:10.1016/j.cej.2009.09.043`.

[24] D. Fernandez Rivas, A. Prosperetti, A. G. Zijlstra, D. Lohse, J. G. E. Gardeniers, Efficient sonochemistry through microbubbles generated with micromachined surfaces, Angewandte Chemie International Edition 49 (**2010**) 9699–9701. `doi:10.1002/anie.201005533`.

[25] C. Mishra, Y. Peles, Cavitation in flow through a micro-orifice inside a silicon microchannel, Physics of Fluids 17(1) (**2005**) 013601. `doi:10.1063/1.1827602`.

[26] A. G. Chakinala, P. R. Gogate, R. Chand, D. H. Bremner, R. Molina, A. E. Burgess, Intensification of oxidation capacity using chloroalkanes as additives in hydrodynamic and acoustic cavitation reactors, Ultrasonics Sonochemistry 15(3) (**2008**) 164–170. `doi:10.1016/j.ultsonch.2007.02.008`.

[27] D. A. Palmer, R. W. Ramette, R. E. Mesmer, Triiodide ion formation equilibrium and activity coefficients in aqueous solution, Journal of Solution Chemistry 13(9) (**1984**) 673–683. `doi:10.1007/BF00650374`.

[28] T. Esch, F. R. Menter, Heat transfer prediction based on two-equation turbulence models with advanced wall treatment, in: K. Hanjalic, Y. Nagano, M. Tummers (Eds.), Proceedings of Turbulence, Heat and Mass Transfer IV, Begell House Inc., 2003.

[29] H. Alehossein, Z. Qin, Numerical analysis of Rayleigh-Plesset equation for cavitating water jets, International Journal for Numerical Methods in Engineering 72(7) (**2007**) 780–807. `doi:10.1002/nme.2032`.

[30] R. Löfstedt, K. Weninger, S. Putterman, B. P. Barber, Sonoluminescing bubbles and mass diffusion, Physical Review E: Statistical, Nonlinear, and Soft Matter Physics 51(5) (**1995**) 4400–4410. `doi:10.1103/PhysRevE.51.4400`.

[31] C. Mishra, Y. Peles, Flow visualization of cavitating flows through a rectangular slot micro-orifice ingrained in a microchannel, Physics of Fluids 17(11) (**2005**) 113602. `doi:10.1063/1.2132289`.

[32] Y.-S. Won, J. W. Bozzelli, Chloroform pyrolysis: experiment and detailed reaction model, Combustion Science and Technology 85(1) (**1992**) 345–373.

[33] V. S. Moholkar, A. B. Pandit, Bubble behavior in hydrodynamic cavitation: effect of turbulence, AIChE Journal 43(6) (**1997**) 1641–1648. `doi:10.1002/aic.690430628`.

[34] L. A. Crum, Nucleation and stabilization of microbubbles in liquids, Applied Scientific Research 38(1) (**1982**) 101–115. `doi:10.1007/BF00385941`.

Pressure wave propagation in air-water slug flow in micro fluidic capillaries with rigid and flexible walls

7

The velocity of pressure wave propagation in gas-liquid slug flow in a micro capillary with an internal diameter of 250 µm with rigid or flexible walls is described with an accuracy within 10% by equations from literature describing pressure wave propagation in slug flow and in bubbly flow. The equations for slug flow reduce to those for bubbly flow at a large number of slugs, as is the case in this work. The model can be used to determine the gas bubble length and gas fraction in gas-liquid slug flow in a capillary when both the pressure drop and the pressure wave propagation velocity are known, and can be used to calculate the length of a safety capillary needed for operation of a gas-liquid separator.

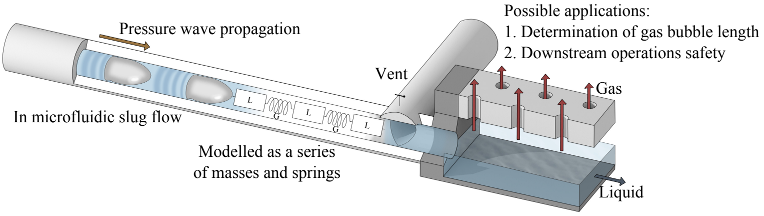

This Chapter is in preparation to be submitted as: J. Rooze, J. C. Schouten, J. T. F. Keurentjes, and E. V. Rebrov, Pressure wave propagation in air-water slug flow in micro fluidic capillaries with rigid and flexible walls.

7.1 Introduction

A full understanding of how compression and rarefaction waves propagate in two-phase flow is desired *e.g.* to use measurements of propagation speed and pressure drop to obtain indirect measurements of the slug length and void fraction. Currently optical or conductivity cells are used to measure these variables. The optical measurements have to be quantified off-line. Having a real-time measurement as is described in this paper would greatly improve the speed of measurement. Furthermore, it can be used for *e.g.* the safe operation of micro fluidic applications. An example is the design and operation of a passive gas-liquid micro structured device for separating the reaction products from a micro reactor, which is incapable of handling over pressures, which is described in the appendix to this paper. Next to these applications a full description of sound propagation in confined bubbly flows would be useful in case of acoustic cavitation is miniaturised, as has been done for hydrodynamic cavitation in the previous Chapter.

The pressure wave propagation velocity has been investigated experimentally in this study for the air-water slug flow in horizontal micro channels with different diameters and moduli of elasticity. The results can be used to measure the gas bubble length indirectly.

Pressure pulse propagation in two-phase flow

The mechanism of pressure wave propagation in two-phase flow is more complex than that in a single phase flow due to the compression of the gas phase and the momentum and energy exchange at the interface, and to the walls[1]. The pressure wave propagation velocity is 330 and 1400 m s^{-1} in air and water at 0 °C, respectively. Various models have been proposed for the propagation velocity in two-phase flow. Usually these models are derived from the momentum balance and continuity balances for the gas and liquid phases. Henry *et al.*[2] have derived a relation for the velocity of sound in homogeneous bubbly flow:

$$c_b = \sqrt{\frac{kp}{\alpha\left(1-\alpha\right)\rho_l}} \tag{7.1}$$

Where c is the speed of sound, k is the adiabatic parameter of the gas, p is the pressure, α is the gas volume fraction in the mixture, also called the void fraction, and ρ is the density. The gas volume fraction can change due to decompression by pressure drop over the length of the capillary. The assumptions made in the derivation are that there is homogeneous flow, no liquid compression, no interphase mass transfer, the superficial liquid and gas velocities are approximately the same $(u_g/u_l \approx 1)$, and a much larger liquid density than the gas density $(\rho_l/\rho_g >> 1)$. The minimum velocity of sound in a two-phase mixture can be an order of magnitude lower than either the velocity of sound in the liquid or the gas[2]. Experimental studies on pressure wave propagation in slug flow[3–5] are less numerous than those in bubbly flow. Several models to describe pressure wave propagation in slug flow have been derived from various physical representations[1,2,5–7]. These models yield results that closely match each other. One of the simplest models is that derived by Korolev by assuming that wave propagation in slug flow is similar to wave propagation in a series of masses and springs[7].

$$c_s = \sqrt{\frac{kp}{\alpha(1-\alpha)\rho_l}}\left(\frac{1}{1+n^{-1}}\right) \tag{7.2}$$

where n is the number of slugs. This equation reduces to the equation for homogeneous flow (Eq. 7.1) in case of a large number of slugs (there is less than 5 % deviation when $n > 19$), as is the case in this work. Also more elaborate models such as the one by Martin and Padmanabhan reduce to the equation for bubbly flow with a large number of slugs[5]. The homogeneous model for pressure wave propagation is subsequently used here since the number of slugs in the experiments in this work is larger than 250.

Wave propagation is slower in capillaries with flexible walls than in capillaries with rigid walls[8]. The tube elasticity is usually taken into account to describe this effect[2,8,9]. The slug flow pressure propagation velocity in inelastic tubes c_s can be adjusted by dividing by a factor to account for elasticity:

$$c_{s,E} = \frac{c_s}{\sqrt{1+\frac{E}{K}\frac{d}{w}}} \tag{7.3}$$

where $c_{s,E}$ is the pressure propagation velocity in slug flow in an elastic tube, K is Young's modulus of elasticity for the capillary, E is the bulk modulus of elasticity for the fluid, d is the capillary diameter, and w is the capillary wall thickness.

7.2 Experimental

A schematic view of the experimental set-up is shown in Fig. 7.1. A valve was closed and opened to create a small pressure disturbance. The valve opening or closing was done with a pneumatic actuator with an opening or closing time of 5 ms. This technique was applied for its simplicity and high accuracy. The gas hold-up was changed from 0.3 to 0.7 by changing the air and water flow rates. The water flow was controlled by a HPLC pump (Shimadzu LC-20AD), and the air was controlled using a Bronkhorst mass flow controller. The water velocity was in the range of 0.05 – 0.5 m s^{-1}, and the air flow rate was in the range of 0.05 – 1.0 m s^{-1}, calibrated at room temperature and pressure. The liquid and gas were mixed in a stainless steel T-mixer (VICI AG International) with a 90° angle between the mixer inlets.

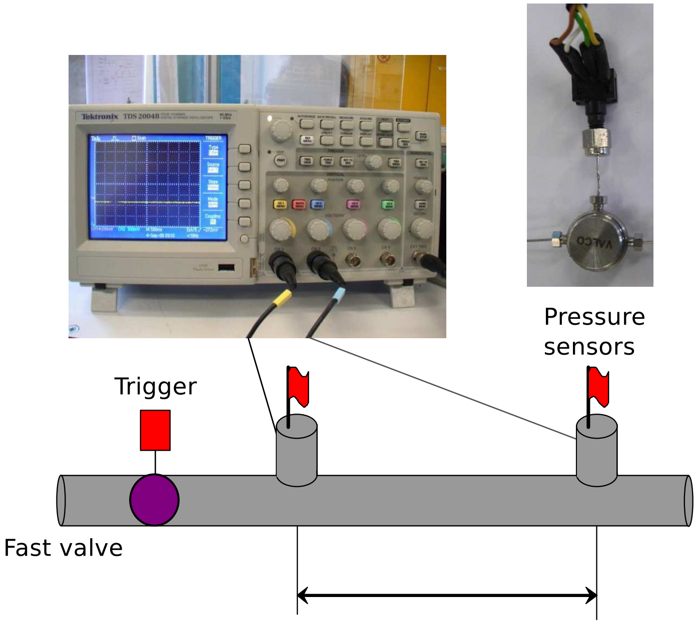

Figure 7.1: A schematic view of the set-up in experiments with short capillaries. The setup consisted of two pressure sensors mounted downstream on the capillary. Data acquisition was done using a triggered oscilloscope and high speed camera.

Several T-mixers with internal diameters in the range of 250 – 500 µm were used to change the slug length at the same gas hold-up.

A trigger was used to synchronise the valve closing, the start of data collection by an oscilloscope, and recording by a high-speed video camera (Redlake MotionPro CCD). An additional short transparent capillary was mounted after the pressure sensors for flow image analysis. The slug velocity, average slug size, and void fraction, were obtained via image analysis under each operational condition from a sequence of 25 to 100 slugs.

the amplitude of the pressure wave decreases exponentially with distance traveled, wave frequency and gas void fraction[10], and can be calculated using:

$$a(z) = a(z_0)e^{-\eta(z-z_0)} \tag{7.4}$$

where $a(z_0)$ is the initial amplitude at the position z_0, $a(z)$ the amplitude at position z, and η is the attenuation coefficient of the pressure wave.

A pressure sensor (26C Series, Sensortechnics) with a 5 % relative error of measurement was mounted at a distance of 2 m downstream from the disturbance valve. Rigid and flexible tubes made of stainless steel, poly(propylene) (PP) or fluorinated ethylene propylene (FEP), with an internal diameter of 120 and 250 µm and a wall thickness of 50 – 270 µm were mounted between the pressure sensor and the valve. The FEP capillary had a length of 39 cm. The average propagation velocity of a pressure wave, c_s is calculated as

$$c_s = \frac{L}{\tau} \tag{7.5}$$

where τ is the time shift between the start of the pressure pulse at the different pressure sensors, and L is the distance between two pressure sensors. The value of the void fraction at the channel exit was obtained by image analysis.

Warnier *et al.* describe an equation for two-phase pressure drop, valid at small capillary numbers $(\mathrm{Ca}_{gl} = \mu u_{gl}/\sigma < 0.01)$[11]:

$$-\frac{dp}{dz} = \frac{2\mu_l u_l}{d^2} f_{gl} \mathrm{Re}_{gl} \tag{7.6}$$

$$\mathrm{FF}_{gl} = \frac{16}{\mathrm{Re}_{gl}} \left(1 + \frac{14.9}{32} d \frac{f_g}{u_{gl}}\right) \left(\mathrm{Ca}_{gl}^{-\frac{1}{3}} + 3.3\mathrm{Ca}_{gl}\right)^{-1} \tag{7.7}$$

where μ is the liquid viscosity, σ is the surface tension, u is the superficial velocity, Re_{gl} is the Reynolds number based on the sum of the superficial velocities of the gas and liquid, u_{gl}, F_g is the gas bubble formation frequency and f is the friction factor. Gas expansion is calculated using the ideal gas equation.

A gas-liquid separator chip and a safety system were operated according to Fig. 1. The gas-liquid slug flow came from a micro reactor system. The pressure after the micro reactor was measured using a pressure sensor (26C Series, Sensortechnics, 0 – 2 bar with respect to atmospheric pressure). A second pressure sensor (26C Series, Sensortechnics, differential pressure 0 – 100 mbar) was used to measure the pressure difference over the gas-liquid separator. When either value crossed its respective threshold value the release valve was opened.

The gas-liquid micro separator chip was fabricated in a glass and silicon wafer (see Fig. 7.6). The pressure difference between the gas-liquid side and the gas disposal side was kept below the capillary pressure of 25 mbar by controlling the flow rate via an additional discharge valve (see Fig. 7.7). Water could flow through the hydrophilic openings made in the bottom of the glass plate. Because the system was slightly pressurised, the gas bubbles were pushed through the hydrophobic membrane pores. The hydrophilic liquid cannot flow into the holes.

7.3 Results and discussion

A pressure wave attenuation coefficient of η of 0.06 m^{-1} is observed in steel and 0.76 m^{-1} in FEP capillaries. The attenuation coefficient does not depend on the superficial fluid velocity. It is 12 % in the steel capillary over the length of 2 meter, and 26 % in the FEP capillary over the length of 0.39 m.

7.3.1 Calculation of void fraction and slug length

Pressure drop, void fraction, and several other parameters are calculated for each position along the capillary. These parameters change due to gas compressibility, since there is a higher pressure near the valve than near the capillary exit. Gas compression is calculated using the ideal gas law. The gas void fraction and bubble length are fixed and have been determined using Eq. 7.2 and the correlations for pressure drop in slug flow from Warnier *et al.*[11]. Two equations with two unknowns can be solved when the pressure drop and pressure wave propagation velocity are known from measurements (see Figs. 7.2 and 7.3).

7.3.2 Propagation velocity in a rigid capillary

The pressure wave propagation velocity has a constant value in the range of void fractions above 0.3 in a stainless steel capillary and does not depend on the superficial liquid velocity under present experimental conditions. The propagation velocity remains constant as the gas hold-up increases from 0.30 to 0.50. The pressure wave propagation velocity increases gradually as the gas hold-up increases beyond 0.50.

The model for propagation velocity and in bubbly flow and in slug flow (Eqs. 7.1 and 7.2) predict the experimental data reasonably well (see Fig. 7.4). A slight rise in propagation velocity is seen experimentally at high void fractions, which is under predicted in the calculations.

7.3.3 Propagation velocity in an elastic capillary

The propagation velocity is lower when the rigid stainless steel capillary was replaced by a flexible plastic capillary with the same internal diameter and wall thickness. A PP capillary reduces propagation velocity by 1.5 times as compared with an AISI-316 stainless steel capillary according to Eq. 7.3. This has been confirmed experimentally. The pressure wave propagation velocity decreases from 32 to 21 m s^{-1} when a stainless steel capillary is replaced with a PP capillary of the same dimensions (see Fig. 7.5). Again the model gives a good approximation of the measured propagation velocity. Low propagation velocities of 9

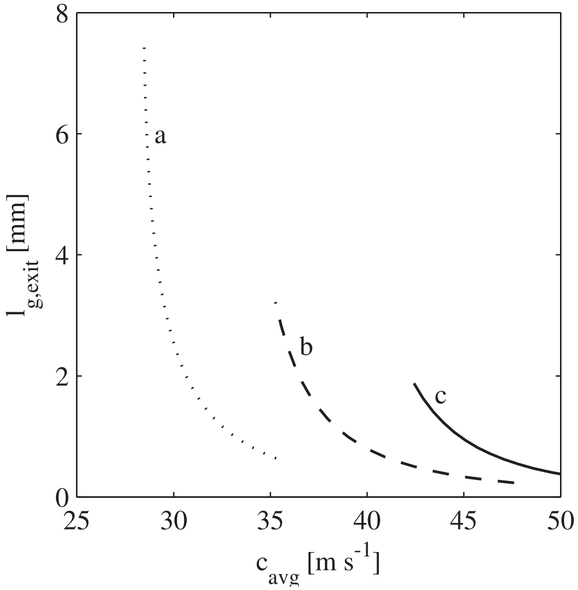

Figure 7.2: Gas bubble length as a function of pressure wave propagation velocity and a total pressure drop of a: 2 bar, b: 4 bar, and c: 6 bar in an air-water slug flow in a 2 m inelastic capillary with an internal diameter of 250 µm. Calculations were done with correlations for pressure drop in slug flow (Eqs. 7.6 and 7.7) and propagation velocity (Eq. 7.2). The two equations with two position dependent unknowns (L_g, and α) can be solved when the system constants capillary length and flow rate, and the variables to measure, the total pressure drop $\frac{dp}{dz}$ and the average propagation speed c, are known. The void fraction was limited between 0.2 and 0.7 to ensure that only the slug flow regime is shown. The gas bubble length is graphically presented as a function of pressure drop and pressure propagation velocity and can be read in the graph when the latter quantities are known. The void fraction can be determined in a similar manner (not shown)

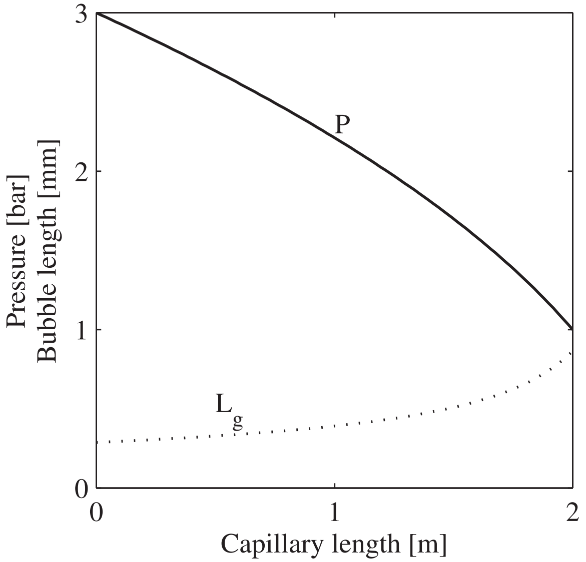

Figure 7.3: The pressure drop and bubble length as a function of the position in the capillary, at a chosen total pressure drop of 2 bar, a pressure propagation speed of 40 m s^{-1}, and a flow rate of 1 mL min^{-1}. The pressure decreases over the length of the capillary, whereas the bubble length increases.

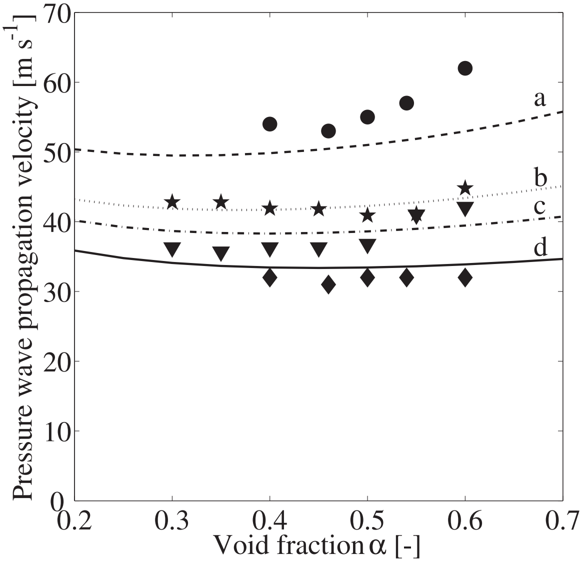

Figure 7.4: Pressure wave velocity as a function of void fraction in a 250 µm internal diameter, 2 m length AISI-316 stainless steel capillary at different bubble lengths, with u_l = 0.5 m s^{-1}. The symbols and lines present the experimental data and modelled data, respectively, at various average bubble lengths $l_g(\alpha = 0.5)$. Circle, a: 1.75 mm, star, b: 1.05 mm, triangle, c: 0.79 mm, diamond, d: 0.46 mm. Deviations from the predictions are due to deviations in the measured bubble length.

and 4 m s^{-1} have been measured in a FEP capillary at void fraction of 0.55 and 0.65. The validity of the model becomes questionable in FEP capillaries because the assumption that the superficial gas and velocities are both much lower than the pressure wave velocity is no longer valid as the pressure wave propagation velocity approaches the superficial liquid flow velocity.

Safe operation of the gas-liquid separator can be achieved using a 15 cm fluorinated ethylene propylene (FEP) capillary. This allows a pressure propagation speed of 30 m s^{-1} when the safety valve switches in 5 ms. This design can handle pressure peaks up to 9.3 bar at the micro reactor outlet.

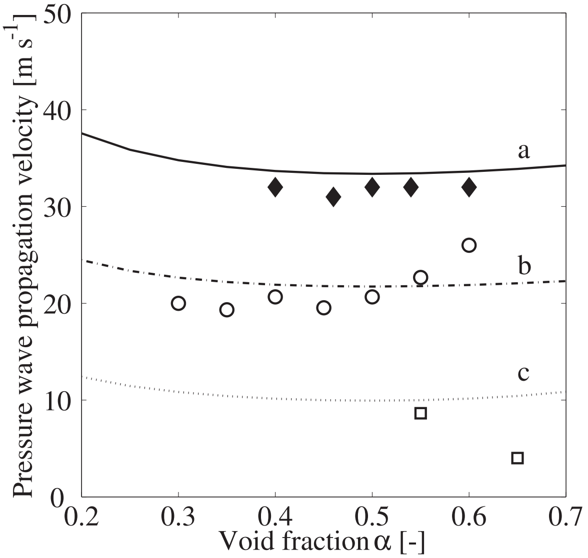

Figure 7.5: Pressure wave velocity as a function of void fraction and tube material for capillaries with internal diameter of 250 µm, a wall thickness of 270 µm, and a length of 2 m. The measured average bubble lengths at the exit are given for gas and liquid velocities equal to 0.5 m s^{-1} to give an indication of the bubble length. The gas bubble length varies with the void fraction, as well as with T-mixer type. The highest velocities (31 m s^{-1}) are obtained using a steel tube (diamond, a: AISI-316, K = 200 GPa), the velocities for more elastic materials are lower: 20 m s^{-1} (circle, b: PP, K = 1.5 GPa), and 4 m s^{-1} (square, c: FEP, K = 0.5 GPa). A correction for capillary wall elasticity is made using Eq. 7.3.

7.4 Conclusions

The pressure wave propagation velocity has been studied in a micro fluidic air-water slug flow regime in capillaries with an internal diameter of 250 µm. The model for pressure propagation in slug flow describes the propagation velocity if the latter considerably exceeds the superficial gas and liquid velocities. The model reduces to an expression for homogeneous bubbly flow for the Taylor flow regime.

An approach to calculate the slug length and void fraction from the pressure drop and propagation speed between two pressure sensors and measurements on propagation velocity and pressure drop are presented. The propagation velocity increases with increasing static pressure.

An elastic capillary wall reduces the pressure wave propagation velocity up to 66 % depending on the capillary material. The propagation velocity reduces from 32 m s^{-1} in a steel capillary to 4 – 9 m s^{-1} in a FEP elastic capillary. A 15 cm FEP capillary allows enough time for release of a pressure wave with an initial amplitude of 9.3 bar.

Bibliography

[1] X.-X. Xu, J. Gong, A united model for predicting pressure wave speeds in oil and gas two-phase pipeflows, Journal of Petroleum Science and Engineering 60(3-4) (**2008**) 150–160. `doi:10.1016/j.petrol.2007.05.012`.

[2] R. E. Henry, M. A. Grolmes, H. K. Fauske, Pressure-pulse propagation in two-phase one- and two-component mixtures, Report ANL-7792, 86, Argonne National Laboratory (1971).

[3] H. J. W. M. Legius, H. E. A. van den Akker, T. Narumo, Measurements on wave propagation and bubble and slug velocities in cocurrent upward two-phase flow, Experimental Thermal and Fluid Science 15(3) (**1997**) 267–278. `doi:10.1016/S0894-1777(97)00012-5`.

[4] F. Huang, M. Takahashi, L. Guo, Pressure wave propagation in air-water bubbly and slug flow, Progress in Nuclear Energy 47(1-4) (**2005**) 648–655. `doi:10.1016/j.pnucene.2005.05.068`.

[5] C. S. Martin, M. Padmanabhan, Pressure pulse propagation in two-component slug flow, Journal Fluids Engineering 101(1) (**1979**) 44–52.

[6] D. L. Nguyen, E. R. F. Winter, M. Greiner, Sonic velocity in two-phase systems, International Journal of Multiphase Flow 7(3) (**1981**) 311–320. `doi:10.1016/0301-9322(81)90024-0`.

[7] A. V. Korolev, Dynamics of low-velocity two-phase flows, Power Engineering 27(5) (**1989**) 101–106.

[8] H. J. Rath, Unsteady pressure waves and shock waves in elastic tubes containing bubbly air-water mixtures, Acta Mechanica 38(1) (**1981**) 1–17. `doi:10.1007/BF01351459`.

[9] S. Vedel, L. H. Olesen, H. Bruus, Pulsatile microfluidics as an analytical tool for determining the dynamic characteristics of microfluidic systems, Journal of Micromechanics and Microengineering 20 (**2010**) 035026(1–11).

[10] H. Wang, G. H. Priestman, S. B. M. Beck, R. F. Boucher, Measurement and simulation of pressure wave attenuation in upward air-water bubbly flow, International Journal of Heat and Fluid Flow 21(1) (**2000**) 104–111. `doi:10.1016/S0142-727X(99)00052-1`.

[11] M. J. F. Warnier, M. H. J. M. de Croon, E. V. Rebrov, J. C. Schouten, Pressure drop of gas-liquid Taylor flow in round micro-capillaries for low to intermediate Reynolds numbers, Microfluidics and Nanofluidics 8(1) (**2010**) 33–45. `doi:10.1007/s10404-009-0448-z`.

[12] D. D. Meng, J. Kim, C.-J. Kim, A degassing plate with hydrophobic bubble capture and distributed venting for microfluidic devices, Journal of Micromechanics and Microengineering 16(2) (**2006**) 419–424. `doi:10.1088/0960-1317/16/2/028`.

[13] T. Y. Chan, G. H. Priestman, J. M. MacInnes, R. W. K. Allen, Development of a micro-channel contactor-separator for immiscible liquids, Chemical Engineering Research and Design 86(1) (**2008**) 65–74. `doi:10.1016/j.cherd.2007.10.010`.

[14] H. Hisamoto, Y. Shimizu, K. Uchiyama, M. Tokeshi, Y. Kikutani, A. Hibara, T. Kitamori, Chemicofunctional membrane for integrated chemical processes on a microchip, Analytical Chemistry 75(2) (**2003**) 350–354. `doi:10.1021/ac025794+`.

[15] C. C. Hsieh, S. C. Yao, Y. Alyousef, Development of a silicon-based passive gas-liquid separation system for microscale direct methanol fuel cells, International Journal of Nanomanufacturing 4(1) (**2009**) 13–25. `doi:10.1504/IJNM.2009.028106`.

[16] J. De Jong, R. G. Lammertink, M. Wessling, Membranes and microfluidics: a review, Lab on a Chip 6(9) (**2006**) 1125–1139. `doi:10.1039/b603275c`.

[17] E. V. Rebrov, M. J. F. Warnier, O. Muraza, M. H. J. M. de Croon, V. Hessel, J. C. Schouten, Advanced catalytic microstructured reactor for continuous chemical synthesis integrated with a separation step, in: AIChE Spring National Meeting, Houston, Texas, USA, 2007, CD-ROM nr. 95b.

[18] E. V. Rebrov, M. H. J. M. de Croon, J. C. Schouten, Propagation of pressure waves in microchannels containing gas-liquid slug flow, in: H. Komayima (Ed.), Book of Abstacts of the 20^{th} International Symposium on Chemical Reaction Engineering (ISCRE-20), Green chemical reaction engineering, Society of chemical engineers, Japan, Kyoto, Japan, 2008.

Appendix

gas–liquid separator safety capillary design

Micro fluidic separator chips can be fabricated by combining hydrophobic and hydrophilic materials and by making use of the capillary pressure in a pore[12–16]. Separator chips are used to remove gas from a gas-liquid mixture. The liquid or gas can subsequently be sent to analysis apparatuses. A gas-liquid micro separator chip has been fabricated from glass and silicon wafers[17,18] (see Fig. 7.6). It can withstand a pressure up to 2 bars, above which liquid leaks into the gas phase. The upstream pressure often exceeds 10 bar to provide the required flow rate of the two-phase mixture. The bubble length, which determines the pressure drop in Taylor flow, depends on the pressure in the gas-liquid mixer, which in turn depends on the pressure drop. Therefore the pressure drop can fluctuate substantially in time, even at the same gas hold-up. A high pressure area can be created at the position of the micro separator in this manner, resulting in membrane leakage. A pressure sensor connected to a fast safety valve is required to monitor pressure changes and release excess pressure. This requires to insert an additional capillary between the pressure sensor and the valve, which would provide enough time to open the valve (see Fig. 7.7) to release the excess pressure before a pressure wave reaches the separator.

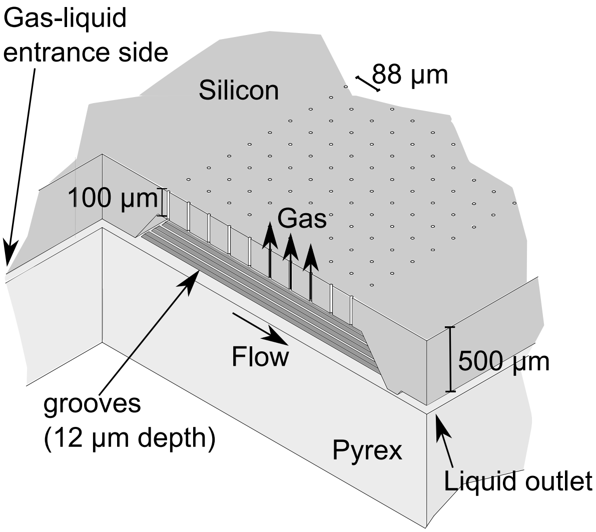

Figure 7.6: Schematic view of the gas-liquid micro separator chip fabricated from two wafers. The bottom side was fabricated in glass and a 100 µm thick membrane with 12 µm wide holes for the gas release was fabricated in silicon. The silicon wafer was anodically bonded to the glass wafer after teflonising with a hydrophobic polymer and subsequent Piraña cleaning. Gas-liquid enters the system over the entire width of the chip (top-left in the image). The liquid flows through the hydrophilic grooves and leaves the system over the entire width of the chip (bottom-right in the image). Gas bubbles flow upwards and leave the system through the hydrophobic silicon membrane.

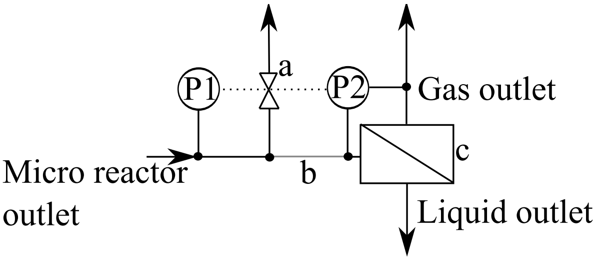

Figure 7.7: Schematic view of the experimental set-up containing a capillary micro reactor and a gas-liquid separation section. P1 is a pressure sensor, P2 is a differential pressure sensor. a: fast valve, b: FEP safety capillary, c: micro separator. The fast valve opens to release an excess of pressure if either the pressure drop exceeds the capillary pressure or if the pressure at sensor P1 exceeds the set-point as a result of a malfunction of the equipment in the upstream section.

8

Conclusions

This thesis describes the effects of dissolved gases on cavitation processes. Dissolved gases play an influential role in several cavitation processes such as bubble nucleation, hot spot temperature determination, and ultimately on the observed effects such as radical production and polymer scission. In this work several of these resulting physical effects are addressed in separate chapters. Besides this topic also hydrodynamic cavitation and pressure wave propagation in micro channels is investigated.

Dissolved gases influence the hot spot temperature by heat conduction and heat capacity. This is observed in experiments in single-bubble and multi-bubble sonoluminescence, where a light-emitting plasma of over 2000 K is formed. The dissolved gas and vapour also participate in chemical reactions. This is best illustrated when the breakdown of a molecule by radicals formed by cavitation is increased when dissolving air instead of the inert argon. The oxygen in the air is easily broken down into two radicals, which subsequently react with the target molecules. Furthermore, the amount of gas present in the liquid alters the radial dynamics of the cavitation bubbles and therefore strain rates around the bubble during collapse, which is encountered in polymer scission experiments.

The sound frequency used to induce cavitation has a tight connection with radical production and optimum dissolved gas composition. By changing it, the sound field in the reactor changes and therewith the location, surroundings, and amplitude of the cavitation cycles that take place. The reactor configuration that is used has a large influence on the formed sound field and therefore it is often not straightforward to compare experiments with those described in literature. A change in the amplitude of the cycle changes the bubble collapse conditions and therefore also the collapse maximum temperature and the radical production.

The potassium iodide radical production increases with a factor of three from 0.6 to 1.7×10^{-10} mol J^{-1} when comparing a 20 kHz sound field to a 62 kHz sound field in argon saturated water at a power of 5 W in a fixed geometry. It is in this case therefore likely that the maximum temperature attained upon collapse is the highest when using 60 kHz ultrasound. The radical production increases at 60 kHz when using air as a saturation gas. Due to the lower adiabatic index of air than that of argon the collapse temperature is lowered, and a lower radical production can be expected. However, a higher radical production is measured due to the combined chemical properties of oxygen and carbon dioxide. Oxygen can form extra radicals at temperatures above 2000 K, and acidification of the solution leads to an increased iodine production. At 20 kHz and 5 W, no radicals are measured when using air as a saturation gas. This is likely because the thermal properties of air reduce the hot spot temperature of the collapse to such an extent that water or oxygen breakdown into radicals is reduced significantly.

Polymer scission of a non-covalently bound silver(I)-NHC complex is found to be due to strain forces rather than due to radical breakdown or pyrolysis. This is further supported by radical production experiments, and by numerical modeling of a collapsing cavitation bubble with different saturation gases. The radical production of argon, nitrogen, methane, and isobutane-saturated toluene 20 kHz ultrasound varies between 1 and 23 $\times 10^{-10}$ mol L J^{-1}, whereas the scission percentage of the 20 kDa polymer is more or less constant under argon, nitrogen, and methane (11–14 %) and slightly lower under isobutane (6 %). Modeling shows that strain rates of over 1×10^{7} s^{-1} are feasible.

Hydrodynamic cavitation in microenvironments yield lower temperatures than ultrasound cavitation. No radicals have formed in a micro channel with a typical orifice dimension of 20 µm in argon saturated water. Molecules that are more easily degraded than water, such as small hydrochlorocarbons need to be added to measure radical production in a milli channel with a typical orifice dimension of 200 µm. A large liquid jet with gas pockets on the sides is formed in the micro channel, which probably does not yield symmetrical collapse of the gas phase. There is a large low pressure volume after the orifice. The milli channel is not constrained after the orifice, and therefore a larger cloud of bubbles is formed. A CFD model of pressure driven flow in a tube including a full Rayleigh-Plesset model for bubble collapse predicts lower temperatures in this case of hydrodynamic cavitation than those during ultrasound collapses. However, this approach assumes a symmetrical collapse of the bubbles in hydrodynamic cavitation, which is not the case most of the time.

Pressure wave propagation speed in slug flow is found to be a function of pressure, void fraction, and wall elasticity. An approach is proposed to estimate the slug length in the Taylor flow regime when the void fraction (gas hold-up), wave propagation speed and pressure drop are known between two measuring sensors in the channel. The model is applied to design a safety capillary for a micro separator unit which cannot withstand pressures over 2 bar. A safety valve is released when a pressure wave approaches. The time the safety valve needs to open and the pressure wave propagation speed determine the length of the safety capillary.

Outlook

The challenges in studies on cavitation in the future mainly lie in the study of the differences between a bubble field and a single bubble, since there are many parameters that influence this behaviour, such as sound frequency, reactor geometry, and dissolved gas. An interesting subset of the single-bubble experiment that is maybe close to multi-bubble behaviour is the instable single bubble. Bubble pinch-off takes place during the cavitation cycle, which disturbs the sphericity and location of the original bubble, and also creates new bubbles which collapse and induce the cavitation effects. More insight into this phenomenon would help progression of multi-bubble fields understanding. The study of cavitation in non-standard solvents such as gas-expanded liquids and sulfuric acid offer a welcome fresh look on the existing theories of cavitation. Not only because extra testing of the theories and models is possible, but also because the new solvents can be tailored to provide the maximum in the desired effects. Also related to the differences between single and multi-bubble fields is knowledge on the full effect of frequency on the cavitation effects. Several studies describe an “optimum” frequency at around 300 kHz, but the resolution of the curve to describe this optimum is low, and furthermore the reaction conditions are often different.

The relation between gas solubility and the cavitation process needs further attention. This is less pronounced in single-bubble experiments since the liquids used there are significantly degassed, but it is likely that this relation influences multi-bubble experiments. A special case is formed by carbon dioxide dissolved in water, since it also slightly acidifies the liquid. This induces an extra apparent radical formation in potassium iodide dosimetry experiments.

Cavitation can be a useful tool for novel processes, as well as intensification of existing processes. Several physical and chemical effects, *i.e.* mixing, radical production, mechanical degradation and pyrolysis, operate simultaneously. A combination of these effects results in the best cost efficiency. Radical production by sonochemistry is an inherently inefficient process. Molecules are dissociated by high temperatures and form radicals. These radicals subsequently either recombine, or react further. No net effect is achieved in case of recombination. A better control strategy of the efficiency of cavitation is desired. The best way of achieving this would be in a multiple single-bubble configuration, with separated oscillating single bubbles with no or low cross-influences between each other. A standing wave sound field with bubbles separated by the Bjerknes forces is one option, and physically separated cavitation bubbles such as cavitation bubbles in a micro channel is another. The inherent limitations of such a configuration are bubble-wall interactions, and the increased difficulty of homogeneous sound transfer into the channels, which can form an additional impedance mismatch between the sound source and the cavitation bubble.

In non-covalent polymer scission the most interesting continuation lies in the validation that subsequent reactions of the cavitation-activated polymer-supported catalyst are really mechanically driven, rather than influenced by radical formation by the cavitation bubble. This requires either tailoring of the saturation gas, *e.g.* using a methane-saturated in toluene liquid phase, or use of a totally different technique to mechanically cut the polymer. Using a single-bubble setup for cavitation studies is preferred over a multi-bubble setup, since the single-bubble experiment allows more accurate probing of the bubble collapse. Strain rates can be estimated in single-bubble experiments by monitoring the bubble radius over time.

Hydrodynamic cavitation offers options for further research despite the lower collapse temperatures and radical formation rates. The bubble cloud can potentially be removed by degassing the water to attain the theoretical temperature of symmetrical single-bubble collapse. In the latter case, scale-up of a single orifice by numbering up opens a way to large scale operation.

Nomenclature

Roman symbols

a	Pressure wave amplitude	Pa
A	Area	m^2
c	Propagation velocity of a pressure wave	$m\ s^{-1}$
C	Concentration	$mol\ m^{-3}$
c_S	Speed of sound	$m\ s^{-1}$
d	Capillary diameter	m
Ca	Capillary number	-
CN	Cavitation number	–
C_p	Heat capacity, constant pressure	$J\ mol^{-1}\ K^{-1}$
C_v	Heat capacity, constant volume	$J\ mol^{-1}\ K^{-1}$
d	Capillary diameter	m
D	Diffusion constant	$m^2\ s^{-1}$
E	Bulk modulus of elasticity for the fluid	Pa
f	Frequency	s^{-1}
F	Empirical factor	–
FF	Friction factor	-
Fo	Fourier number	–
h	Enthalpy per molecule	$J\ molecule^{-1}$
k	Adiabatic parameter	-
K	Young's modulus of elasticity	Pa
k_B	Boltzmann constant	$J\ K^{-1}$

l	Liquid slug or gas bubble length	m
L	Distance between two pressure sensors	m
M	Molecular weight	kg mol^{-1}
n	Number of slugs	-
N	Number of moles	mol
N_A	Avogadro constant	molecules mol^{-1}
p	Pressure	Pa
Pe	Péclet number	–
Q	Flow rate	$\mathrm{m}^3\ \mathrm{s}^{-1}$
Q	Amount of heat	J
r	Polar coordinate	m
R	Bubble radius	m
Re	Reynolds number	–
R_g	Gas constant, 8.3145	J $\mathrm{mol}^{-1}\ \mathrm{s}^{-1}$
T	Temperature	K
t	Time	s
u	Superficial velocity	m s^{-1}
V	Speed of sound in the liquid	m s^{-1}
v	Fluid velocity	m s^{-1}
w	Capillary wall thickness	m
W	Work	J
x	Gas fraction	-
z	Length coordinate, axial direction	m
Greek symbols		
α	Gas fraction	-
α	Thermal diffusivity	$\mathrm{m}^2\ \mathrm{s}^{-1}$
δ	Boundary layer thickness	m
ΔH	Enthalpy	J $\mathrm{mol}^{-1}\ \mathrm{K}^{-1}$
ϵ	Strain	–
η	Attenuation coefficient pressure wave	m^{-1}

γ	Adiabatic index of the gas	–
$\gamma(\mathrm{Pe})$	Modified adiabatic index, changing during ultrasound cycle	–
κ	Heat conduction coefficient	$\mathrm{J\ m^{-1}\ K^{-1}\ s^{-1}}$
λ	Longest characteristic relaxation time of a polymer	s
μ	Viscosity	$\mathrm{N\ s\ m^{-2}}$
ρ	Density	$\mathrm{kg\ m^{-3}}$
σ	Surface tension	$\mathrm{N\ m^{-1}}$
τ	Time difference between arrival of pressure pulses at two positions	s

Superscripts

$\dot{}$	Time derivative	$\mathrm{s^{-1}}$
$\ddot{}$	Second time derivative	$\mathrm{s^{-2}}$
sat	Saturation value	

Subscripts

0	Initial conditions
1	Position 1
2	Position 2
a	Of the acoustic field
avg	Average value
b	Bubbly flow
c	Of the constriction
collapse	During the collapse
cond	Condensation
DS	Downstream
E	Elastic capillary
exit	At the capillary exit
g	Gas
gl	Based on the sum of the superficial gas and liquid velocities
i	At the interface
∞	At large distance
l	Liquid

max	Maximum value
m	For mass transport
ref	Reference value
s	Slug flow
thresh	Threshold value
th	For heat transport
v	Vapour
vap	Vaporisation

About the author

Joost Rooze was born August 24, 1981 in Eindhoven. He went to the St. Willibrord Gymnasium in Deurne for secondary education. After obtaining his diploma in 1999 he started as a student in Chemical Engineering at the Chemical Engineering and Chemistry department at the Eindhoven University of Technology. He obtained his Master of Science degree in 2006 with a thesis on “Maxwell-Stefan modelling of non-aqueous nanofiltration”. After doing contract research for a period of 9 months with ETD&C, Ede he started a PhD on the topic of cavitation in the group of prof.dr.ir. Jos Keurentjes under supervision of dr. Nieck Benes. In 2008 the research was continued in the Laboratory of Chemical Reaction Engineering under the daily supervision of prof.dr. Evgeny Rebrov and supervision of prof.dr.ir. Schouten and prof.dr.ir. Keurentjes. In March 2011 he joined ASML where he is currently employed as an overlay engineer.

List of publications

J. Rooze, E. V. Rebrov, J. C. Schouten, and J. T. F. Keurentjes, Effect of resonance frequency, power input, and saturation gas type on the oxidation efficiency of an ultrasound horn, *Ultrasonics Sonochemistry*, 18(1) (**2011**) 209–216.

J. Rooze, R. Groote, R. T. M. Jakobs, R. P. Sijbesma, M. M. van Iersel, E. V. Rebrov and J. C. Schouten and J. T. F. Keurentjes, Mechanism of ultrasound scission of a silver-carbene coordination polymer, *The Journal of Physical Chemistry B* 115(38) (**2011**) 11038–11043

J. Rooze, M. André, G.-J. S. van der Gulik, D. Fernández-Rivas, J. G. E. Gardeniers, E. V. Rebrov and J. C. Schouten and J. T. F. Keurentjes, Hydrodynamic cavitation in micro channels with channel sizes of 100 and 750 micrometers, *Microfluidics Nanofluidics* 12(1–4) (**2011**) 499–508

J. Rooze, E. V. Rebrov, J. C. Schouten, and J. T. F. Keurentjes, Cavitation and dissolved gas: a review.*Ultrasonics Sonochemistry*, accepted

Publications in preparation

J. Rooze, E. V. Rebrov, J. C. Schouten, and J. T. F. Keurentjes, Enhanced ultrasonic radical production in water saturated with argon-oxygen-carbon dioxide gas mixtures.

J. Rooze, J. C. Schouten, J. T. F. Keurentjes, and E. V. Rebrov, Pressure wave propagation in an air-water slug flow in capillaries with rigid and flexible walls.

Oral presentations

J. Rooze, M. M. van Iersel, M. A. van Schilt, N. E. Benes, and J. T. F. Keurentjes, High yield gas-phase sonochlorination of methane, Conference of the European Society for Sonochemistry (ESS11), Montpellier, France, **2008**.

J. Rooze, D. Fernández Rivas, J. G. E. Gardeniers, E. V. Rebrov, J. T. F. Keurentjes, and J. C. Schouten, Hydrodynamic cavitation in a microchannel, 11th International Conference on Microreaction Technology, Kyoto, Japan, **2010**.

J. Rooze, E. V. Rebrov, J. C. Schouten, and J. T. F. Keurentjes, Frequency and gas-dependent efficiency of a 20-kHz horn at 20, 41, and 62 kHz, The 12th European Society of Sonochemistry conference, Chania, Greece, **2010**.

J. Rooze, R. Groote, R. T. Jakobs, R. P. Sijbesma, M. M. van Iersel, E. V. Rebrov, J. C. Schouten, and J. T. F. Keurentjes, Non-covalent bond scission by ultrasound under radical-suppressing conditions, The 12th European Society of Sonochemistry conference, Chania, Greece, **2010**.

Dankwoord

Een proefschrift schrijven mag dan wel een solitaire aangelegenheid schijnen aangezien er maar één naam op de voorkant prijkt, maar er zijn natuurlijk een groot aantal mensen zonder wie dit werk niet tot stand zou kunnen zijn gekomen.

Jos, jij hebt me in staat gesteld om me uit te leven op deze wetenschappelijke studie, met de randvoorwaarden die daar bij horen, zoals bijvoorbeeld een tot in de puntjes uitgerust lab en de juiste mensen daaromheen. Toen je terugging naar Akzo Nobel was het even zoeken naar de juiste invulling van jouw en mijn tijd, maar dat is allemaal op zijn pootjes terecht gekomen. In die drukke periode zorgde je toch nog steeds voor support op de juiste momenten, bedankt daarvoor.

Jaap, jij hebt me heel goed opgevangen in jouw groep ná het vertrek van Jos terug naar Akzo Nobel. Stiekem was het toch wel een spannende tijd op dat moment, maar dankzij jouw faciliterende rol is de overgang redelijk soepeltjes verlopen. Bedankt ook voor je bijdrage in de wetenschappelijke discussies, waaruit ook bleek dat je je ook betrokken voelde bij het project.

Evgeny, thanks for continuing the coaching of the project after I moved to the SCR group, it was a very pleasant time together; in my opinion at least! You also moved after accepting a professorship in Belfast. I wish you all the best in your new position! Also thanks for the extensive discussions on all kinds of topics.

Nieck, bedankt voor het op de rails zetten van het project, veel succes met je inmiddels niet meer zo nieuwe positie aan de Universiteit Twente. Als ik je enthousiaste verhalen als uitgangspunt neem gaat dat helemaal goedkomen.

De subsidie voor mijn project kwam van technologiestichting STW, waarvoor dank uiteraard. In projecten van STW is er ook input en ondersteuning van een gebruikerscommissie vanuit de industrie. Dr.ir. Gert-Jan van der Gulik van Bunova, dr.ir. Jan Hofman van het KWR watercycle research institute, en prof.dr. Stephan Kallweit van ILA bedankt voor het zitting nemen in deze commissie en voor jullie input en hulp. Ook was het fijn dat er discussie en hulp was van prof.dr. Han Gardeniers en prof.dr. Detlef Lohse en hun studenten David

Fernández Rivas en Laura Stricker. Met Gert-Jan en onze student Matthieu André, Han en David is er ook nog een tastbaar bewijs van prettige samenwerking gekomen in de vorm van het artikel over hydrodynamische cavitatie. Matthieu, it was a pleasure being your coach, good luck with your PhD in Washington D.C., and David good luck with the remainder of your PhD and anything that follows!

Rint, behalve dat jij hebt plaatsgenomen in mijn leescommissie, heb ik ook een prettige samenwerking met jou en je studenten Bob en Ramon achter de rug, wat geresulteerd heeft in plaatsing van een artikel in the Journal of Physical Chemistry B. Bob en Ramon, veel succes nog met jullie verdere activiteiten, ik zie de verdere interessante stukken van jullie hand graag verschijnen in de bladen!

De vaste medewerkers van SCR en SPD bedankt voor jullie hulp. Jullie zorgen niet alleen voor een vruchtbare omgeving waarin de aio's kunnen excelleren in het onderzoek, maar ook voor de cohesie in de groep. De mannen van de werkplaats, Anton, Chris, Dolf, Erik, en Madan bedankt voor alle tijd en expertise, in het bijzonder de meestal kleine klusjes die noodzakelijk waren om mij (en vast ook vele anderen) verder te helpen. Mijn fiets zal nooit meer dezelfde zijn dankzij de apparaten in de werkplaats! Madan in het bijzonder bedankt voor het ontwerpen van de milli-cavitatiemodule uit hoofdstuk 6, ik vind het nog steeds een mooi apparaatje in al zijn flexibiliteit en eenvoud. Peter, Carlo, en Marlies stonden altijd klaar voor hulp op en rond het lab, dank daarvoor. Denise bedankt voor het helpen bij allerhande zaken, zoals het herinneren aan formulieren om in te vullen, stukjes om te schrijven, en met name voor het achter mijn broek aanzitten om mij de laatste meters te laten afleggen. Martin, Mart, Johan, en Jan bedankt voor hulp tijdens mijn project en voor discussies eromheen!

De aio's van SPD en SCR bedankt voor de samenwerking op het lab, voor de gezelligheid en nuttige discussies in de koffiekamer, en tijdens andere activiteiten op de faculteit, en daarnaast, vooral mede-koffielurkers en quiz/F.O.R.T./kart-maatjes Marco, Stijn, Michiel, Jack, Patrick, Maurice, Niek, Tom, en Frans, met aanhang allemaal, en vele anderen. Ook Maikel bijzonder bedankt voor alle hulp, suggesties, en discussies over ons onderwerp. Met name zal mij het ESS-congres in La Grande Motte, Frankrijk bijblijven met de redelijk familiaire sfeer voor een congres, en ook de enigzins surrealistische aankomst aldaar. With Jovan and Stijn I went to the microreactor technology conference IMRET, it was a pleasure hanging out with you guys while discussing the pros and cons of analytical solutions versus numerical solutions, and therefore sort of forgetting to have a good look at the picturesque surroundings! Also a big thanks to my roomies over the years Eric, Niek, Stijn, Shrikrant, Dulce, and Kevin for putting up with my feet on the desk and for providing the sometimes much needed comical relief!

In de lunchpauzes kon ik mooi stoom afblazen in de diverse zaalvoetbalcompetities in het studentensportcentrum met de Vlakkers en de Cup-a-soup Tigers en ook de overige faculteitsvoetbalteams die altijd mooie derby's afwerkten in een fanatieke doch sportieve sfeer. Sjoerd, Michiel, Tom, Carlos, Joris, Mark, Maria, Marcos, Vladimir, Stijn, and all the others: it's a pity we can't play anymore but we'll remember the glorious past! En op zondag waren er natuurlijk alle mannen van NWC 5 om een balletje mee te trappen, alhoewel de "harde kern", Bas, Jozef, Lars, Paul, Ronald, Lucien, Gerrit, Joost, Babbel, Rob, Ricky en Christian (en Bob, die is ook wel harde kern ondanks zijn Horizonmentaliteit) de laatste jaren in toenemende mate aan de kant (of elders) stond in plaats van op het veld.

Over stoom afblazen gesproken, dank aan alle schermvriendjes die zichzelf als gewillig doelwit aandienden op de loper of die de moeite namen om mij eens even flink in de luren te leggen. Ouwe lollies Alke, Bente, Harm, Jitte, Jos, Jeroen, Marloes, Martijn, Maurice, Peter, het was erg leuk om met jullie de (studenten)toernooitjes en andere activiteiten af te struinen, met name de GNSK's waren onvergetelijk: als laatste aanwezig 's avonds, en als laatste van de loper af de volgende dag! Ik hoop op de dag van de verdediging toe te treden tot een illuster gezelschap van leden van de badjassencommissie, dat bovendien zelf een badjas heeft! Alke bedankt ook voor hulp met een aantal van de graphical abstracts.

Mijn familie, vooral ook opa en oma, erg bedankt voor de steun, hulp, interesse ("cavitatie" stond er bij een enkeling in de agenda, om het even op te frissen vóór familieactiviteiten), en gezelligheid de afgelopen jaren (en daarvoor). Ook kan ik altijd bij mijn schoonfamilie terecht, Henk, Fieke, Debby en Marjolijn en aanhang, bedankt daarvoor.

Mam, pap, en Marjol, ik heb me nooit ergens zorgen om hoeven te maken; het is fijn om te weten dat jullie altijd voor me klaarstaan, bedankt voor alles.

Anke, je inspireert me, ik prijs mezelf gelukkig dat ik zoveel tijd met je mag doorbrengen.